Extending resolution of structured illumination microscopy with sparse deconvolution

Weisong Zhao
Harbin Institute of Technology https://orcid.org/0000-0002-5969-1956

Shiqun Zhao
Peking University

Liuju Li
State Key Laboratory of Membrane Biology, Beijing Key Laboratory of Cardiometabolic Molecular Medicine, Institute of Molecular Medicine, Peking University, Beijing 100871

Xiaoshuai Huang
State Key Laboratory of Membrane Biology, Beijing Key Laboratory of Cardiometabolic Molecular Medicine, Institute of Molecular Medicine, Peking University, Beijing 100871

Shijia Xing
Peking University

Yulin Zhang
Peking University https://orcid.org/0000-0001-9107-0634

Guohua Qiu
Harbin Institute of Technology

Zhenqian Han
Harbin Institute of Technology

Yingxu Shang
CAS Key Laboratory of Nanosystem and Hierarchical Fabrication, CAS Center for Excellence in Nanoscience, National Center for Nanoscience and Technology

De-en Sun
College of Chemistry and Molecular Engineering, Peking University

Chunyan Shan
Peking University https://orcid.org/0000-0002-5532-2811

Runlong Wu
Peking University

Shuwen Zhang
National Laboratory of Biomacromolecules, CAS Center for Excellence in Biomacromolecules, Institute of Biophysics, Chinese Academy of Sciences

Riwang Chen
Peking University

Jian Xiao

Wuhan University

Yanquan Mo

State Key Laboratory of Membrane Biology, Beijing Key Laboratory of Cardiometabolic Molecular Medicine, Institute of Molecular Medicine, Peking University, Beijing 100871

Jianyong Wang

State Key Laboratory of Membrane Biology, Beijing Key Laboratory of Cardiometabolic Molecular Medicine, Institute of Molecular Medicine, School of Future Technology, Peking University

Wi Ji

National Laboratory of Biomacromolecules, CAS Center for Excellence in Biomacromolecules, Institute of Biophysics, Chinese Academy of Sciences

Xing Chen

College of Chemistry and Molecular Engineering, Peking University https://orcid.org/0000-0002-3058-7370

Baoquan Ding

National Center for Nanoscience and Technology https://orcid.org/0000-0003-1095-8872

Yanmei Liu

Institute for Brain Research and Rehabilitation (IBRR), Guangdong Key Laboratory of Mental Health and Cognitive Science, South China Normal University, Guangzhou, China

Heng Mao

Peking University

Baoliang Song

Wuhan University

Jiubin Tan

Harbin Institute of Technology

Jian Liu

Harbin Institute of Technology

Haoyu Li

Harbin Institute of Technology

Liangyi Chen (lychen@pku.edu.cn)

State Key Laboratory of Membrane Biology, Beijing Key Laboratory of Cardiometabolic Molecular Medicine, Institute of Molecular Medicine, Peking University https://orcid.org/0000-0003-1270-7321

Article

Keywords: Photon Flux, Intricate Structural Intermediates, Signal-to-noise Ratio, Spatiotemporal Resolution, Live-cell Fluorescence Microscopy

Posted Date: March 2nd, 2021

DOI: https://doi.org/10.21203/rs.3.rs-279271/v1

Extending resolution of structured illumination microscopy with sparse deconvolution

Weisong Zhao[1,14], Shiqun Zhao[2,14], Liuju Li[2,14], Xiaoshuai Huang[5], Shijia Xing[2], Yulin Zhang[2], Guohua Qiu[1], Zhenqian Han[1], Yingxu Shang[9], De-en Sun[10], Chunyan Shan[13], Runlong Wu[2], Shuwen Zhang[11], Riwang Chen[7], Jian Xiao[12], Yanquan Mo[2], Jianyong Wang[6], Wei Ji[11], Xing Chen[10], Baoquan Ding[9], Yanmei Liu[2,8], Heng Mao[4], Baoliang Song[12], Jiubin Tan[1], Jian Liu[1], Haoyu Li[1]✉, Liangyi Chen[2,3,6]✉

[1]School of Instrumentation Science and Engineering, Harbin Institute of Technology, Harbin 150080, China.

[2]State Key Laboratory of Membrane Biology, Beijing Key Laboratory of Cardiometabolic Molecular Medicine, Institute of Molecular Medicine, School of Future Technology, Peking University, Beijing 100871, China.

[3]PKU-IDG/McGovern Institute for Brain Research, Beijing 100871, China.

[4]School of Mathematical Sciences, Peking University, Beijing 100871, China.

[5]Biomedical Engineering Department, Peking University, Beijing 100191, China.

[6]Shenzhen Bay Laboratory, Shenzhen 518055, China.

[7]School of Software and Microelectronics, Peking University, Beijing 100871, China.

[8]Institute for Brain Research and Rehabilitation (IBRR), Guangdong Key Laboratory of Mental Health and Cognitive Science, South China Normal University, Guangzhou, China.

[9]CAS Key Laboratory of Nanosystem and Hierarchical Fabrication, CAS Center for Excellence in Nanoscience, National Center for Nanoscience and Technology, Beijing, China.

[10]College of Chemistry and Molecular Engineering, Peking University, Beijing, China.

[11]National Laboratory of Biomacromolecules, CAS Center for Excellence in Biomacromolecules, Institute of Biophysics, Chinese Academy of Sciences, Beijing, China.

[12]Hubei Key Laboratory of Cell Homeostasis, College of Life Sciences, Wuhan University, Wuhan, China.

[13]College of Life Sciences, Peking University, 100871, Beijing, China.

[14]These authors contributed equally: Weisong Zhao, Shiqun Zhao, Liuju Li.

✉e-mail: lychen@pku.edu.cn; lihaoyu@hit.edu.cn

The spatial resolutions of live-cell super-resolution microscopes are limited by the maximum collected photon flux. Taking advantage of a priori knowledge of the sparsity and continuity of biological structures, we develop a deconvolution algorithm that further extends the resolution of super-resolution microscopes under the same photon budgets by nearly twofold. As a result, sparse structured illumination microscopy (Sparse-SIM) achieves ~60 nm resolution at a 564 Hz frame rate, allowing it to resolve intricate structural intermediates, including small vesicular fusion pores, ring-shaped nuclear pores formed by different nucleoporins, and relative movements between the inner and outer membranes of mitochondria in live cells. Likewise, sparse deconvolution can be used to increase the three-dimensional resolution and contrast of spinning-disc confocal-based SIM (SD-SIM), and operates under conditions with the insufficient signal-to-noise-ratio, all of which allows routine four-color, three-dimensional, ~90 nm resolution live-cell super-resolution imaging. Overall, sparse deconvolution may be a general tool to push the spatiotemporal resolution limits of live-cell fluorescence microscopy.

Despite the theoretically unlimited resolution, the spatial resolution of super-resolution (SR) microscopy in live-cell imaging is still limited. Because multiple raw images are usually taken to reconstruct one super-resolved image, any increase in the spatial resolution must be matched with an increase in temporal resolution to avoid resolution degradation due to motion artifacts of fast moving subcellular structures in live cells, such as tubular endoplasmic reticulum (ER)[1], lipid droplets, mitochondria and lysosomes[2]. Therefore, the highest resolution of current live-SR microscopy is limited to ~60 nm, irrespective of the modalities used[3-7]. To achieve that resolution, excessive illumination power (kW~MW/mm^2) and long exposures (> 2 s) are usually required[8], which may compromise the integrity of the holistic fluorescent structure and degrade the achievable resolution.

Previously we developed a Hessian deconvolution algorithm for structured illumination microscopy

(SIM), which enables ultrafast and hour-long SR imaging in live cells[9]. However, its resolution is limited at 90~110 nm posed by linear spatial frequency mixing. Nonlinear SIM with ~60 nm resolution comes at a cost of reduced temporal resolution and requires photoactivatable/photoswitchable fluorescent proteins that are susceptible to photobleaching[10]. Because the resolution and contrast inside deep layers of the cell are still compromised by the fluorescence emissions and the scattering from out-of-focus planes, high-contrast SR-SIM imaging is largely limited to imaging depths of 0.1 to 1 μm[9-11]. To date, no SR method has achieved millisecond exposures with ~60 nm spatiotemporal resolution in live cells, or is capable of multi-color, three-dimensional, long-term SR imaging.

Alternatively, mathematical bandwidth extrapolation that may boost spatial resolution without hardware modifications was first proposed in the 1960s[12, 13]. It follows that when the object being imaged has a finite size, there exists a unique analytic function that coincides inside the bandwidth-limited frequency spectrum band of the optical transfer function (OTF), thus enabling the reconstruction of the complete object by extrapolating the observed spectrum[14-16]. For example, the iterative Richardson-Lucy (RL) deconvolution[17, 18] could surpass the Rayleigh criterion in separating double stars in astronomical imaging[19]. However, such astronomical SR imaging was shown to be infeasible for solar systems later[20]. Recently, a compressive sensing paradigm also enables SR in proof-of-principle experiments[21]. However, these bandwidth extrapolation methods failed in actual applications because the stable reconstruction depends critically on the accuracy and availability of the assumed a priori knowledge[14-16], and logarithmically on the image signal-to-noise ratio (SNR)[21-23]. Thus, despite the theoretical feasibility, it is generally agreed that the Rayleigh diffraction limit represents a practical frontier that cannot be overcome by applying bandwidth extrapolating methods on images obtained from conventional imaging systems[14].

Here we have shown that RL deconvolution improves resolution in synthetic, bandwidth-limited, noise-free fluorescence images, but fails in real microscopic images containing noise. With a novel algorithm that

incorporates both the sparsity and the continuity as the a priori knowledge to constrain the iterative deconvolution followed, we have overcome resolution limits of current SIM[9, 10], spinning-disc confocal SIM (SD-SIM)[24], stimulated emission depletion (STED)[5], wide-field, confocal, two-photon[25], and expansion microscopes[26]. Therefore, our sparse deconvolution algorithm may help current fluorescence microscopes to push their spatiotemporal resolution limits and better resolve intricate, three-dimensional, and fast dynamics in live cells.

RESULTS

Method execution

Unlike the Wiener deconvolution that operates in the Fourier domain (**Supplementary Note 1**), iterative RL deconvolution approximates in the space domain and has been proposed to improve resolution under specific conditions[19, 20]. However, in practice, it is usually used to reduce out-of-focus blur and noise[27, 28]. To understand how RL deconvolution works, we have synthesized ground-truth images containing various-shaped structures that were filtered with a band-limited OTF (**Supplementary Note 2**). Interestingly, sufficient iterations of RL deconvolution correctly recovered the high-frequency information in these synthetic images without noise (**Supplementary Fig. 1**, **2**), thus demonstrating the possible potential of pure computational SR. On the other hand, in images corrupted with the noise similar to that captured by real-world microscopes, RL deconvolution failed to improve resolution (**Supplementary Fig. 2**).

In the presence of noise, RL deconvolution quickly converges to a solution dominated by the noise after a small number of iterations[28], which constitutes the major problem. For any fluorescence microscopes, to ensure sufficient Nyquist sampling criteria for maximal spatial resolution dictated by the optics, their point spread function (PSF) must occupy more than 3 × 3 pixels in space (**Supplementary Fig. 3**), which constitutes the basis for the continuity along x and y axes of any fluorescence microscopes[9]. Therefore, we used the continuity in xy and also t to suppress noise and subsequent reconstruction artifacts, as we have done before[9].

However, the application of continuity a priori also obscures the images and reduces the resolution. Therefore, we propose introducing the sparsity as another prior knowledge to antagonize resolution degradation and extract the high-frequency information. This is because an increase in spatial resolution always leads to smaller PSF for any given fluorescence microscopes. As compared with a conventional microscope, the convolution of the object with the smaller PSF in SR imaging always confers a relative increase in sparsity (**Supplementary Fig. 3**). Therefore, we believe that continuity and sparsity are general features of the fluorescence microscope, which could be used as the prior knowledge to suppress noise and facilitate high-frequency information extraction (detailed in **Supplementary Note 3**).

Overall, we have proposed the following loss function containing these two priors, in which the Hessian matrix continuity to reduce artifacts and increase robustness at the price of reduced resolution, and the sparsity to balance the extraction of high-frequency information, which gives:

$$\arg\min_{\mathbf{x}}\left\{\frac{\lambda}{2}\left\|\mathbf{f}-\mathbf{b}-\mathbf{A}\mathbf{x}\right\|_2^2+\mathrm{R}_{\mathrm{Hessian}}(\mathbf{x})+\lambda_{\mathrm{L1}}\left\|\mathbf{x}\right\|_1\right\},$$

where the first term on the left side of the equation is the fidelity term, representing the distance between recovered image **x** and the input SIM image **f**. Here, **b** is the background estimated using the method described in **Supplementary Notes 4.3**, and **A** is the PSF of the optical system. The second and third terms are the continuity prior and sparsity prior, respectively. $\|\cdot\|_1$ and $\|\cdot\|_2$ are the ℓ_1 and ℓ_2 norms, respectively. λ and λ_{L1} denote the weight factors, balancing the image's fidelity and the sparsity. Instead of ℓ_0 norm (absolute sparsity) used as the start point in compressive sensing theory[29], we directly used the ℓ_1 norm (sparsity score in **Supplementary Fig. 3a**), i.e., the sum of the absolute values of each element, which can handle both absolutely and relatively sparse structures and constrain the extraction of high spatial frequency information (examples listed in **Supplementary Fig.4**). The details for minimizing such convex problems could be found in **Supplementary Notes 3** and **4**, and the full pipeline was shown in **Extended Data Fig. 1**.

Sparse deconvolution improves resolution and contrast in synthetic images corrupted with noise

First, we tested the functionality of different steps in our deconvolution pipeline on synthetic filament structures. While filaments closer than ~100 nm could hardly be resolved by Wiener inverse filtering, reconstruction with the sparsity a priori created only a small difference in fluorescence of the middle part between the two filaments, while the final deconvolution resulted in the clear separation of two filaments down to ~81 nm apart (**Extended Data Fig. 2a**, **2b**). However, the contrast for two filaments ~65 nm apart was low, which could be further improved after the pixel upsampling (labeled as ×2) procedure (**Extended Data Fig. 2c**, **2d**). Regarding synthetic filament structures corrupted with different levels of noise, deconvolution without the addition of the sparsity a prior was unable to retrieve the high-frequency information reliably, while deconvolution without the addition of the continuity a priori led to reconstruction artifacts that manifested particularly in raw images with low SNR (**Extended Data Fig. 3**). Only the combination of the continuity and sparsity enabled robust and high-fidelity extrapolation of the high-frequency information inaccessible to SIM, even under situations with considerable noise (**Extended Data Fig. 3**, **Supplementary Table 1**, **2**).

In addition, on deconvolution of synthesized punctated- or ring-shaped structures with diameters of 60 ~ 120 nm, previous RL deconvolution was only able to resolve rings with diameters larger than 110 nm, while more iterations led to over-shrink artifacts; in contrast, sparse deconvolution was able to resolve rings with diameter down to 60 nm and produced smaller puncta closely resembling the ground truth (**Extended Data Fig. 4**). Unlike content-dependent SR via deep learning algorithms[30, 31], the sparse deconvolution could resolve erratic synthetic structures in the same field-of-view (FOV, **Supplementary Fig. 6**).

Finally, the poor SNR condition may limit the sparse deconvolution in improving resolution. Under extreme noisy conditions, parallel lines after the sparse deconvolution sometimes manifested as twisted and fluctuated fluorescence profiles, indicative of artifacts (**Supplementary Fig. 7**). According to a line restoration quality criterion we proposed (detailed in **Supplementary Note 5**), the sparse deconvolution could not

faithfully extract information beyond the OTF in images under 150% Gaussian noise condition (**Supplementary Fig. 8**). However, compared to the RL deconvolution, it significantly increased the contrast of high-frequency information within the OTF, enabled lines 100 nm apart to be separated (**Supplementary Fig. 7**), or better visualization of weakly-labeled microtubules under the SD-SIM (**Supplementary Fig. 9**).

Benchmarking of sparse deconvolution against samples with known structures

We benchmarked the performance of sparse deconvolution on imaging structures with known ground-truth. By low-pass filtering the image obtained by the 1.4 NA objective with a synthetic PSF from a 0.8 NA objective in the Fourier domain, we created a blurred version of actin filaments (**Extended Data Fig. 5a**, **5b**). Interestingly, two blurry opposing actin filaments under the low NA objective became separable after sparse deconvolution, along with an extended Fourier frequency domain (**Extended Data Fig. 5c**, **5d**). Likewise, two neighboring filaments ~120 nm apart (confirmed by 2D-SIM) were resolved by the sparse deconvolution of wide-field images (**Extended Data Fig. 5e**, **Supplementary Video 15**). In addition, a CCP of ~135 nm in diameter under the TIRF-SIM manifested as a blurred punctum in wide-field images that had undergone conventional deconvolution or been deconvolved with the Hessian continuity a priori. Only after sparse deconvolution did the ring-shaped structure emerge (**Extended Data Fig. 5f**). Similarly, sparse deconvolution but not the RL deconvolution resolved pairs of horizontal lines 150 nm apart (**Extended Data Fig. 6**), and extended OTF of the wide-field microscope (**Extended Data Fig. 7**).

Next, we have designed and synthesized rod-like origami with two sites fluorescently labeled, each labeled with 4~5 Cy5 molecules (**Extended Data Fig. 8**). When these molecules were 60, 80, and 100 nm apart, they were barely distinguishable under the TIRF-SIM but well-separated after the up-sampling followed by the sparse deconvolution (Sparse-SIM ×2, **Fig. 1**). Similarly, one obscure line in the commercial Argo-SIM slide under the 2D-SIM could be resolved as two parallel lines 60 nm apart after the sparse deconvolution only (**Fig. 2a**, **2b**). This resolution enhancement was maintained in processing variable SNR images captured

under different conditions but failed at extremely low SNR (1/16 SNR, **Extended Data Fig. 9**), recapitulating previous experiments with the synthetic image (**Supplementary Fig. 7**, **8**).

Sparse-SIM also resolved ring-shaped nuclear pores labeled with different nucleoporins (Nup35, Nup93, Nup98, or Nup107), while they were similar in sizes to 100-nm fluorescent beads in the same FOV under the 2D-SIM (**Fig. 2c**, **2d**, **Extended Data Fig. 10**, **Supplementary Video 1**). After corrected for narrower fitted diameters of nuclear pores due to camera pixel sizes and pore diameters comparable to the resolution of Sparse-SIM (**Supplementary Fig. 23**, **Supplementary Note 9.1**), Nup35 and Nup107 pores were ~66 ± 3 nm and ~97 ± 5 nm in diameters, while Nup98 and Nup93 pores were of intermediate sizes (**Fig. 2e**, **2f**). These estimations nicely agreed with previous results obtained with different SR methods in fixed cells[32-34]. Interestingly, 12-min SR imaging enables visualization of the vigorous reshaping of nuclear pores in live cells, possibly reflecting reoriented individual nuclear pore complex on the nuclear membrane to or away from the imaging plane (**Fig. 2g**, **Extended Data Fig. 11**), which would be difficult for other SR methods.

Finally, we tested the reliability of sparse deconvolution in resolving immunofluorescent-labeled complicated structures after expansion microscopy[26] (**Fig. 3**). Compared to those obtained by the 2D-SIM, tubulin filaments from the 4.5× expanded cell after the sparse deconvolution were comparable in resolution but better contrasted (**Fig. 3a-3c**). Similarly, while sparse deconvolution of the same expanded complex ER tubules yielded similar overall shapes to that obtained by SIM reconstruction, it was much less affected by artifacts (**Fig. 3d-3f**). Taken together, these data demonstrate a *bona fide* increase in spatial resolution by our sparse deconvolution.

Sparse-SIM achieves 60 nm resolution within millisecond exposures in live cells

Concentrated actin forms a gel-like, dynamic network under the cell cortex with pore diameters of 50~200 nm[35], which are challenging tasks for any live-cell SR methods for the requirement on the combined spatiotemporal resolution. In the COS-7 cell, two actin filaments ~66 nm apart, indistinguishable with either

2D-SIM or Hessian-SIM, were resolved by Sparse-SIM (**Fig. 4a-c**, **Supplementary Video 2**). In contrast, applying previous claimed sparsity-based deconvolution algorithms[21, 36] (**Supplementary Note 10**) produced thinner actin filaments at the price of much-amplified artifacts and removed some filaments (**Supplementary Fig. 25a-25c**). In our sparse deconvolution, better separation of dense actin meshes resulted from both the enhanced contrast (**Fig. 4d**) and the increased spatial resolution, as shown both by the full-width-at-half-maximum (FWHM) analysis of actin filaments and Fourier ring correlation (FRC) mapping analysis[37, 38] (**Fig. 4e**, **4f**). This increase in resolution was stable during time-lapse SR imaging of actin dynamics (**Fig. 4g**), which led to more frequent observations of small pores within the actin mesh. The mean diameter of pores within the cortical actin mesh was ~160 nm from the Sparse-SIM data (**Fig. 4i**), similar to those measured by the STORM method in fixed cells[35].

An increase in the spatial resolution also helped resolve the ring-shaped caveolae (fitted diameter ~60 nm) (**Fig. 4j-4l**, **Supplementary Video 3**), which required nonlinear SIM at the expense of limited imaging durations and additional reconstruction artifacts[10]. The fidelity of the reconstruction was confirmed since we did not observe significant artifacts in the error map obtained with the resolution-scaled error analysis[38] (**Extended Data Fig. 12**). For vesicles such as lysosomes and lipid droplets within the cytosol under wide-field illumination, the sparse deconvolution reduced the background fluorescence and produced high quality images (**Fig. 4m**, **4n**, **Supplementary Video 4**).

By rolling reconstruction with a temporal resolvability of 564 Hz[9], Sparse-SIM could also distinguish fusion pores labeled by VAMP2-pHluorin in INS-1 cells smaller than those detectable by the conventional TIRF-SIM (such as the pore with a fitted diameter of ~61 nm, **Fig. 4o**, **4p**, **Supplementary Video 5**, **6**). In fact, small pores (mean diameter ~87 nm, size corrected following the calibration protocol of nuclear pores) appeared at the early stage of vesicle fusion and lasted only for ~9.5 ms; instead, larger pores (~116 nm in diameter) manifested at the later stage of the exocytosis and sustained for ~47 ms (**Fig. 4q**). For the TIRF-

SIM, the opening time of the initial pores and the stationary pores were indistinguishable (~37 ms, **Fig. 4q**), indicating that the early small pore stage was invisible. Nevertheless, although this exocytosis intermediate was not observed by other SR methods, our data agreed with the much lower probability of observing small fusion pores than the larger ones by the rapid-freezing electron microscope reported more than three decades ago[39].

Relative movements between sub-organellar structures observed by dual-color Sparse-SIM

Sparse-SIM could be readily used in a dual-color imaging mode to improve the resolution at both wavelengths. For example, in COS-7 cells with both outer and the inner mitochondrial membranes (OMM and IMM) labeled with Tom20-mCherry and Mito-Tracker Green, Sparse-SIM showed sharper cristae structures than did the conventional 2D-SIM, and readily detected two types of OMM:IMM configurations: a long crista extended from one side to ~142 nm away from the other side of the OMM, and a short crista extended only ~44 nm towards the other side of the OMM (**Extended Data Fig. 13a-13d**, **Supplementary Video 7**). Time-lapse SR imaging also revealed rare events, such as the IMM extension not being enclosed within the Tom20-labeled structures in a few frames (**Extended Data Fig. 13e**). This result might be explained by the non-homogenous distribution of Tom20 protein on the OMM[40].

Dual-color Sparse-SIM imaging also resolved more details regarding organelle contacts, including those formed between the mitochondria and ER. We found that ER tubules (Sec61β-mCherry) randomly contacted the mitochondria with equal probability at both the cristae regions and the regions between cristae (**Extended Data Fig. 13f**, **Supplementary Video 8**). In addition, the contact between one ER tubule and the top of a mitochondrion not only correlated with the directional movement of the latter but also the synergistically rearranged orientations of cristae thereafter (**Extended Data Fig. 13g**, **Supplementary Video 8**).

Sparse deconvolution increases the three-dimensional resolution of SD-SIM

Because the continuity and sparsity a priori are general features of SR microscopy, we tested our algorithm on

images obtained by the pinhole-based SD-SIM[24, 41-43]. By imaging large fluorescent beads (100 nm) and correcting for the alias effects (**Supplementary Note 9.2**)[44] or imaging small beads without corrections, we showed a lateral resolution of ~90 nm and an axial resolution of ~266 nm of Sparse SD-SIM (**Extended Data Fig. 14**), a nearly twofold increase of spatial resolution in all three axes compared to the SD-SIM.

In live COS7-cells labeled with clathrin-EGFP, Sparse SD-SIM enables a previously blurred fluorescent punctum to be resolved as a ring-shaped structure with a fitted diameter of ~97 nm (**Fig. 5a**, **5b**, **Supplementary Video 9**), which agrees with the resolution given by the beads analysis and the FRC method (**Fig. 5c**) and could not be achieved by other sparsity-based deconvolution methods (**Supplementary Fig. 25d**, **25e**). The median estimated diameter of all the ring-shaped CCPs was ~158 nm (**Fig. 5d**), the same as previously measured with high-NA TIRF-SIM[10]. Events such as the disappearance of a ring-shaped CCP (**Fig. 5e**) and the disintegration of another CCP into two smaller rings nearby could be seen (**Fig. 5f**). Because photon budget allowed by the Sparse SD-SIM could be as small as was ~0.9 W/cm^2 (**Supplementary Table 3**), both actin filaments and CCPs within a large FOV of 44 μm × 44 μm could be monitored for more than 15 min at a time interval of 5 s (**Fig. 5g**, **Extended Data Fig. 15**, **Supplementary Video 16**). Under these conditions, many relative movements between CCPs and filaments could be seen. For example, we observed the *de novo* appearance and the stable docking of a CCP at the intersection of two actin filaments, followed by its disappearance from the focal plane as the neighboring filaments closed up and joined together (**Extended Data Fig. 15d**), which is consistent with the role of actin in the endocytosis of CCPs[45]. Similarly, dual-color Sparse SD-SIM also revealed dynamic interplays between ER tubules and lysosomes, such as the hitchhiking behavior described previously[11] (**Extended Data Fig. 16**, **Supplementary Video 17**).

Sparse SD-SIM could easily be adapted to four-color SR imaging, allowing the dynamics of lysosomes, mitochondria, microtubules, and nuclei to be simultaneously monitored in live cells (**Fig. 5h**, **5i**, **Supplementary Video 10**) at FRC resolutions as small as 79~90 nm (**Fig. 5j**). Benefiting from the absence

of out-of-focus fluorescence and the improved axial resolution, Sparse SD-SIM allowed similar structures to be seen at similar contrast levels throughout the cells, such as the mitochondrial outer membrane structures with FWHMs at ~280 nm axially (**Fig. 5l**) maintained in the live cell that is ~7 μm thick (**Fig. 5k**, **Supplementary Video 11**), which was in sharp contrast to the failure of the RL deconvolution (**Supplementary Fig. 26**).

Sparse deconvolution on a finer grid helps to recover resolution of images of insufficient Nyquist sampling

Despite their superior quantum efficiency and electron-multiplying capability, the large pixel size of EMCCD cameras may limit the system resolution. For example, EMCCD-based SD-SIM images of ER tubules after sparse deconvolution conferred an FRC resolution of ~195 nm, mostly determined by the undersampling of the pixel size ~94 nm (**Fig. 6a**, **6b**, **Supplementary Video 12**). We artificially upsampled the image on a finer grid (labeled as × 2, ~47 nm pixel size) before subsequent sparse deconvolution. Along with an increase in the FRC resolution to ~102 nm and the expanded system OTF (**Fig. 6b**, **6d**), previously blurred ring-shaped ER tubules became distinguishable (pointed by white arrows in **Fig. 6c**).

In HeLa cells, we used Sparse SD-SIM to follow dynamic interactions among lysosomes, peroxisomes, and microtubules in time (**Fig. 6e**, **Supplementary Video 13**), which could not be resolved by PURE denoise[46] or RL deconvolution (**Supplementary Fig. 27**). Many peroxisomes encounter lysosomes on microtubules, demonstrated by a lysosome moving along the microtubules and colliding with two peroxisomes stably docked closely to the intersection of two tubulin filaments (**Fig. 6f**), or the co-migration of a lysosome and a peroxisome along a microtubule for some time before separation and departure (**Fig. 6g**). These contacts may mediate lipid and cholesterol transport, as reported previously[47].

Finally, we observed nuclei, mitochondria, and microtubules in a three-dimensional volume spanning ~6 μm in the axial axis of a live COS-7 cell (**Fig. 6h**, **Supplementary Video 14**). Again, the axial FWHM of a

microtubule filament decreased from ~465 nm in the raw dataset to ~228 nm after Sparsity ×2 processing (**Fig. 6i**). In contrast, TV deconvolution[48] (**Supplementary Fig. 28**) failed to improve the *xy*-*z* axes contrast. From the volumetric reconstruction, it was apparent that the continuous, convex nuclear structure bent inward and became concave at regions in some axial planes that were intruded by extensive microtubule filaments and mitochondria (**Fig. 6j**). Such reciprocal changes suggest that the tubulin network may affect nucleus assembly and morphology[49].

DISCUSSION

It is long believed that microscopic optics determines its bandwidth limit. Therefore, it is difficult to imagine how sparse deconvolution extracts the high-frequency information beyond the microscope OTF. By synthesizing the ground-truth image containing various-shaped structures convolved with band-limited PSF, we have shown that RL deconvolution recovers information beyond the spatial frequency limit under the noise-free condition (**Supplementary Fig. 1**, **Supplementary Note 2**). This data instead demonstrates an alternative possibility, in which the total information carried by the microscope is invariant[15, 50], and adding a priori knowledge (nonnegative) may help reveal more details of the object. In this sense, by introducing the sparsity and continuity a priori knowledge to constrain the iterative deconvolution, we have significantly alleviated its problem of converging to artifacts in the presence of noise[27, 28] (**Supplementary Fig. 2**, **7**).

As we have elaborated in **Supplementary Note 3**, the sparsity and continuity priors are general features of high-resolution fluorescence microscopes. Correspondingly, using the sparse deconvolution on images obtained with the point-scanning confocal microscope, we observed features of nuclear pores and microtubules comparable to those obtained with STED[5] (**Extended Data Fig. 18**). Moreover, as compared to the normal STED, Sparse-STED also provided increased resolution and showed images of actin, ER, and microtubules in live cells at ~40 nm FRC resolution (**Extended Data Fig. 19**). Finally, sparse deconvolution also extended the observable spatial frequency spectrum of a miniaturized two-photon microscope[25], nearly

doubled its resolution quantified by the decorrelation method at different axial positions[51], and enabled numerous dendritic Thy1-GFP-labeled spines to be visualized in the live mouse brain (**Extended Data Fig. 20**, **Supplementary Video 18**).

Unlike the content-dependent SR imaging achieved by the deep-learning algorithms[30, 31], our sparse deconvolution is content-agnostic, such as revealing both rings and punctuated beads in the same FOV (**Extended Data Fig. 10**), distinguishing both the bisected ring mixed with irregular lines (**Supplementary Fig. 6**), and appreciating tubulin filaments and ER tubules after expansion microscopy (**Fig. 3**). Even for cells labeled with cytosolic Ca^{2+} indicators[52] that were far from absolute sparsity, sparse deconvolution could increase the resolution of SD-SIM without nonlinearly perturbed amplitudes of different Ca^{2+} transients (**Extended Data Fig. 17**). All these data endorse our sparse deconvolution algorithm's general applicability in handling different samples captured under various fluorescence microscopes (**Supplementary Table 4**, **Supplementary Fig. 3**).

As a computational SR method, sparse deconvolution faces challenges and caveats often associated with its forerunners, i.e., iterative deconvolution algorithms. For example, in addition to the resolution enhancement limited by the image SNR (**Supplementary Note 5**), whether sparse deconvolution provides high fidelity SR images also depends on the optimal choice of parameters. Having listed all parameters used in the software (**Supplementary Note 6**, **7**), we concluded that we only needed to adjust the fidelity and sparsity values carefully, while their optimal values follow an approximately linear relationship (**Supplementary Fig. 11**). It is also worth noticing that high SNR images afford large fidelity values, while low SNR ones require small fidelity numbers (**Supplementary Note 7**). Inappropriate choice of the fidelity and sparsity values may lead to either no increase in resolution, the emergence of artifacts (**Supplementary Fig. 12**), or the removal of weak signals (**Supplementary Fig. 16, Supplementary Fig. 21d**). Therefore, we have provided step-by-step examples in **Supplementary Note 8** to guide others to use the software better, and emphasized that any novel

structures identified by the sparse deconvolution need to be cross-validated by other fluorescence SR methods or electron microscopy.

For two-dimensional live-cell SR imaging, Sparse-SIM confers the best spatiotemporal resolution combination and achieves ~60 nm resolution at a temporal resolvability of ~2 ms, two orders of magnitude faster than other live-cell SR methods with similar spatial resolution. However, we have recently shown that organelles of different refractive indices within the cell cause illumination scattering and distorted grids that lead to reconstruction artifacts[53]. To avoid artifacts caused by illumination scattering within the live cells, Sparse SD-SIM represents a better choice for multi-color three-dimensional SR imaging, as it maintains the resolution and contrast enhancement throughout different planes. For tissues with even more scattering that require confocal, STED, or even two-photon microscopes, our sparse deconvolution algorithm may improve their resolution as well. Therefore, by providing the detailed source code, ready-to-use software, and example datasets for others to use and explore, we expect our sparse deconvolution method to be broadly tested to push the spatiotemporal resolution limits of current fluorescence microscopes at no additional hardware cost.

METHODS

Cell maintenance and preparation. INS-1 cells were cultured in RPMI 1640 medium (GIBCO, 11835-030) supplemented with 10% FBS (GIBCO), 1% 100 mM sodium pyruvate solution, and 0.1% 55 mM 2-mercaptoethanol (GIBCO, 21985023) in an incubator at 37°C with 5% CO_2 until ~75% confluency was reached. COS-7 cells and HeLa cells were cultured in high-glucose DMEM (GIBCO, 21063029) supplemented with 10% fetal bovine serum (FBS) (GIBCO) and 1% 100 mM sodium pyruvate solution (Sigma-Aldrich, S8636) in an incubator at 37°C with 5% CO_2 until ~75% confluency was reached. For the 2D-SIM imaging experiments, cells were seeded onto coverslips (H-LAF 10L glass, reflection index: 1.788, diameter: 26 mm, thickness: 0.15 mm, customized). For the SD-SIM imaging experiments, 25-mm coverslips (Fisherbrand, 12-545-102) were coated with 0.01% Poly-L-lysine solution (SIGMA) for ~24 hours before seeding transfected cells.

Samples for SIM imaging.

DNA origami Materials. M13mp18 phage DNA was purchased from New England Biolabs incorporation and was used without any further purification. All staple strands, including Cy5 modified and biotin modified staple strands, were purchased from Sangong Biotech (Shanghai, China). The Cy5 labeled and biotin-modified staple strands were purified by denaturing polyacrylamide gel electrophoresis (PAGE) with the rest staples used as received without further purification. The DNA origami staple strands were premixed and stored in 1.5 mL EP tubes under -20 °C.

DNA origami design and assembly. The 14-helix bundle DNA origami nanostructure (14HB) was designed with a length of 178 nm using the open-source software caDNAno[54]. The structural integrity and rigidity were examined using the online modeling server Cando[55, 56]. We mixed scaffold strands, staple strands, and Cy5 modified staple strands at a molar ratio of 1: 10: 10 in 1 * TAE buffer (with 18 mM Mg^{2+}). Then the mixed solution was annealed in a BioRad PCR thermocycler using a program: from 95 °C to 65 °C (5 min/°C); from

65 ℃ to 45 ℃ (90 min/℃); from 45 ℃ to 25 ℃ (10 min/℃). After the annealing process, the DNA origami nanostructures were purified using 2% agarose gel electrophoresis. Finally, the DNA origami nanostructures were extracted from the gel and stocked in 1 * TAE/ Mg^{2+} buffer for further use.

Preparing DNA origami samples for SIM imaging. To immobilized DNA origami on the surface, the DNA origami was modified with eighteen biotinylated staple strands that can bind to a BSA–biotin–streptavidin-coated SIM cover glass surface. The cover glass was processed as described in ROSE[57]. The DNA origami structures were mixed with 2 μl of the 80/100/120 nm structure and 4 μl of the 60 nm, and then diluted with 200 μl PBS with 10 mM $MgCl_2$. Then, 200 μl mixture was pipetted into the cover glass, incubated for 5 min. After three times washing with PBS, the sample was ready for imaging.

Argo-SIM slide. To validate the increase in resolution, we used a commercial fluorescent sample (the Argo-SIM slide, Argolight, France) with ground-truth patterns consisting of fluorescing double line pairs (spacing from 0 nm to 390 nm, λ_{ex}= 300–550 nm, http://argolight.com/products/argo-sim/).

Live-cell samples. For the 2D-SIM experiments, to label LEs/LYs, COS-7 cells were incubated with 1× LysoView™ 488 (Biotium, 70067-T) in complete cell culture medium at 37°C for 15–30 min and protected from light, without being washed and imaged. To label LEs/Lys in the SD-SIM experiments, we incubated COS-7 cells in 50 nM LysoTracker Deep Red (Thermo Fisher Scientific, L12492) for 45 min and washed them 3 times in PBS before imaging. To label LDs, COS-7 cells were incubated with 1 × LipidSpot™ 488 (Biotium, 70065-T) in complete cell culture medium at 37°C for 30 min and protected from light before being washed and imaged. To label mitochondria, COS-7 cells were incubated with 250 nM MitoTracker™ Green FM (Thermo Fisher Scientific, M7514) and 250 nM MitoTracker® Deep Red FM (Thermo Fisher Scientific, M22426) in HBSS containing Ca^{2+} and Mg^{2+} or no phenol red medium (Thermo Fisher Scientific, 14025076) at 37°C for 15 min before being washed three times before imaging. To perform nuclear staining, COS-7 cells

were incubated with 10 μg/ml Hoechst (Thermo Fisher Scientific, H1399) in PBS for ~5 mins and washed 3 times in PBS.

To label cells with genetic indicators, COS-7 cells were transfected with caveolin-EGFP/LifeAct-EGFP/LAMP1-EGFP/LAMP1-mChery/Tom20-mScarlet/Tom20-mCherry/Sec61β-Cherry/Sec61β-EGFP/clathrin-EGFP/clathrin-DsRed. For calcium imaging experiments, COS-7 cells were transfected with GCaMP6s. To label nuclear pores, COS-7 cells were transfected with GFP-Nup35/ GFP-Nup93/ GFP-Nup98/GFP-Nup107. HeLa cells were transfected with Tubulin-EGFP/Pex11a-BFP/LAMP1-mChery. INS-1 cells were transfected with Vamp2-pHluorin. The transfections were executed using Lipofectamine^{TM} 2000 (Thermo Fisher Scientific, 11668019) according to the manufacturer's instructions. After transfection, cells were plated in pre-coated coverslips. Live cells were imaged in a complete cell culture medium containing no phenol red in a 37°C live cell imaging system. For the calcium lantern imaging in SD-SIM, calcium signal was stimulated with a micropipette containing 10 μmol/L 5'-ATP-Na_2 solutions (Sigma-Aldrich, A1852)[52]. For the experiments conducted with INS-1 cells, the cells were stimulated with a solution containing 70 mM KCl and 20 mM glucose, and vesicle fusion events were observed under a TIRF-SIM microscope[9]. For beads imaging, the 100-nm-diameter fluorescent beads (Thermo Fisher Scientific, T7279) were diluted to 1:100 in PBS.

Samples preparation for expansion microscopy.

α-tubulin immunostaining. COS-7 cells were seeded in a Lab-Tek II chamber slide (Nunc, 154534). Cells were firstly extracted in the cytoskeleton extraction buffer (0.2% (v/v) Triton X-100, 0.1 M PIPES, 1 mM EGTA and 1 mM $MgCl_2$, pH 7.0) for 1 min at room temperature (r.t.). Next, the extracted cells were fixed with 3% (w/v) formaldehyde and 0.1% (v/v) glutaraldehyde for 15 min, reduced with 0.1% (w/v) $NaBH_4$ in PBS for 7 min, and washed three times with 100 mM glycine. Then the cells were permeabilized with 0.1% (v/v) Triton X-100 for 15 min, and blocked with 5% (w/v) BSA in 0.1% (v/v) Tween 20 for 30 min. for

antibody staining, the cells were incubated with monoclonal rabbit anti-α-tubulin antibody (Abcam, ab52866, 1:250 dilution) in antibody dilution buffer (2.5% (w/v) BSA in 0.1% (v/v) Tween 20) overnight at 4 °C, washed three times with 0.1% (v/v) Tween 20, incubated with Alexa Fluor 488-conjugated F(ab')2-goat anti-rabbit secondary antibody (Thermo, A11070, 1:1,000 dilution) in antibody dilution buffer for 2 h at r.t. and washed three times with 0.1% (v/v) Tween 20.

Sec61β-GFP transfection. COS-7 cells were seeded in a Lab-Tek II chamber slide (Nunc, 154534) and cultured to reach around 50% confluence. For transient transfection of Sec61β-GFP in a single well, 500 ng plasmid and 1 μL of X-tremeGENE HP (Roche) were diluted in 20 μL Opti-MEM sequentially. The mixture was vortexed, incubated for 15 min at r.t., and applied to cells. 24 h after transfection, the cells were washed three times with PBS and fixed as described in the α-tubulin immunostaining experiment.

Sample expansion. The sample expansion was performed as previously described[26, 58]. The labeled cells were incubated with 0.1 mg mL^{-1} of Acryloyl-X (AcX, Thermo, A20770) diluted in PBS overnight at r.t. and washed three times with PBS. To prepare the gelation solution, freshly prepared 10% (w/w) N,N,N′,N′-tetramethylethylenediamine (TEMED, Sigma, T7024) and 10% (w/w) ammonium persulfate (APS, Sigma, A3678) were added to the monomer solution (1×PBS, 2 M NaCl, 2.5% (w/v) acrylamide (Sigma, A9099), 0.15% (w/v) N,N′-methylenebisacrylamide (Sigma, M7279) and 8.625% (w/v) sodium acrylate (Sigma, 408220)) to a final concentration of 0.2% (w/w) each. Next, the cells were embedded with the gelation solution first for 5 min at 4 °C, and then for 1 h at 37 °C in a humidified incubator. The gels were immersed into the digestion buffer (50 mM Tris, 1 mM EDTA, 0.1% (v/v) Triton X-100, and 0.8 M guanidine HCl, pH 8.0) containing 8 units mL^{-1} proteinase K (NEB, P8107S) at 37 °C for 4 h, and then placed into ddH_2O to expand. Water was changed 4-5 times until the expansion process reached a plateau. By determining the gel sizes of before and after the expansion, we quantified the expansion factor to be 4.5 times. The gels were immobilized on poly-D-lysine-coated glass No. 1.5 cover-glass for further imaging.

Samples for the STED imaging. To label the ER tubules/actin/microtubule in live cells, COS-7 cells were either transfected with Sec61β-EGFP/LifeAct-EGFP, or incubated with SiR-Tubulin (Cytoskeleton, CY-SC002) for ~20 mins without wash before imaging. For immunofluorescence experiments, HeLa cells were quickly rinsed with PBS and immediately fixed with prewarmed 4% PFA (Santa Cruz Biotechnology, sc-281692). After rinsing three times with PBS, cells were permeabilized with 0.1% Triton® X-100 (Sigma-Aldrich, X-100) in PBS for 15 mins. Cells were blocked in 5% BSA/PBS for 1h in room temperature. Primary antibodies (monoclonal mouse anti Mab414 1:1000, Abcam, ab24609; monoclonal mouse anti-Tom20 1:1000, BD Biosciences, 612278; monoclonal rat anti-Tubulin 1:1000, Abcam, ab6160) were incubated in 2.5% BSA/PBS blocking solution in 4°C cold room overnight, followed by the final washing in PBS. Secondary antibodies (goat anti-mouse conjugated to AlexaFluor594, Abcam, ab150120; goat anti-rat conjugated to AlexaFluor647, Abcam, ab150167) were used at concentrations of 1:500 and incubated in 2.5% BSA/PBS blocking solution at room temperature, followed by washing.

The interference-based SIM setup. The schematic illustration of the system is based on a commercial inverted fluorescence microscope (IX83, Olympus) equipped with a TIRF objective (100×/1.7 HI oil, APON, Olympus), a TIRF objective (100×/1.49 oil, UAPON, Olympus), a wide-field objective (100×/1.45 oil, APON, Olympus) and a multiband dichroic mirror (DM, ZT405/488/561/640-phase R; Chroma) as described previously[9]. In short, laser light with wavelengths of 488 nm (Sapphire 488LP-200) and 561 nm (Sapphire 561LP-200, Coherent) and acoustic, optical tunable filters (AOTF, AA Opto-Electronic, France) were used to combine, switch, and adjust the illumination power of the lasers. A collimating lens (focal length: 10 mm, Lightpath) was used to couple the lasers to a polarization-maintaining single-mode fiber (QPMJ-3AF3S, Oz Optics). The output lasers were then collimated by an objective lens (CFI Plan Apochromat Lambda 2× NA 0.10, Nikon) and diffracted by the pure phase grating that consisted of a polarizing beam splitter (PBS), a half-wave plate, and the SLM (3DM-SXGA, ForthDD). The diffraction beams were then focused by another

achromatic lens (AC508-250, Thorlabs) onto the intermediate pupil plane. A carefully designed stop mask was placed to block the zero-order beam and other stray light and to permit passage of ±1 ordered beam pairs only. To maximally modulate the illumination pattern while eliminating the switching time between different excitation polarizations, we placed a home-made polarization rotator after the stop mask[9]. Next, the light passed through another lens (AC254-125, Thorlabs) and a tube lens (ITL200, Thorlabs) to focus on the objective lens's back focal plane, which interfered with the image plane after passing through the objective lens. Emitted fluorescence collected by the same objective passed through a dichroic mirror (DM), an emission filter, and another tube lens. Finally, we used an image splitter (W-VIEW GEMINI, Hamamatsu, Japan) before the sCMOS camera (Flash 4.0 V3, Hamamatsu, Japan) to split the emitted fluorescence into two channels.

The SD-SIM setup. The SD-SIM is a commercial system based on an inverted fluorescence microscope (IX81, Olympus) equipped with a wide-field objective (100×/1.3 oil, Olympus) and a scanning confocal system (CSU-X1, Yokogawa). Four laser beams of 405 nm, 488 nm, 561 nm, and 647 nm were combined with the SD-SIM. The Live-SR module (GATACA systems, France) was equipped with the SD-SIM. The images were captured either by an sCMOS camera (C14440-20UP, Hamamatsu, Japan) or an EMCCD camera (iXon3 897, Andor), as mentioned in **Fig. 5** or **Fig. 6**.

The STED setup. Image acquisition of STED was obtained using a gated STED (gSTED) microscope (Leica TCS SP8 STED 3X, Leica Microsystems, Germany) equipped with a wide-field objective (100×/1.40 oil, HCX PL APO, Leica). The excitation and depletion wavelengths were 488 nm and 592 nm for the Sec61β-GFP and LifeAct-GFP, 594 nm and 775 nm for the AlexaFluor594, 635 nm and 775 nm for the AlexaFluor647, 651 nm and 775 nm for SiR-tubulin. The detection wavelength range was set to 495-571 nm for GFP, 605-660 nm for AlexaFluor594, 657-750 nm for SiR, 649-701 nm for AlexaFluor647. For comparison, confocal images were acquired in the same field before the STED imaging. All images were obtained using the LAS AF software (Leica).

The miniaturized two-photon microscope setup. The Thy-1-GFP transgenic mouse was awake and head fixed under the miniature two-photon microscope[25] (FHIRM TPM-V1.5, Transcend Vivoscope Biotech Co., Ltd, China) *in vivo* by using a micro-objective with NA 0.7. The FOV of the microscope is 190 × 190 μm^2, the frame rate is 13 Hz (512 × 512 pixels), and the working distance is 390 μm. The three-dimensional imaging is from 50 μm to 160 μm below the cortex with 1 μm of each slice. The raw stack captured by MTPM is registered by the rigid body transformation[59] before further processing and visualization.

The usage of sparse deconvolution software. In the **Supplementary Software** user interface (UI), we included thirteen parameters to adapt to different hardware environments, experimental conditions, and fluorescence microscopes (**Supplementary Fig. 10**). To simplify the usage of software, we have classified them into three categories: fixed parameters, image property parameters, and content-aware parameters. We have explained these parameters in detail in **Supplementary Note 6**. In short, the ten parameters in the first two categories are primarily determined by the optical system and image property and hardly need tuning. Only the three content-aware parameters need to be adjusted back-and-forth carefully by visual examination of the reconstruction results. In **Supplementary Note 7** followed, we discussed ideal values of the sparsity and the fidelity under different experimental conditions. While the optimal values of fidelity and sparsity follow an approximately linear relationship, high SNR images afford large fidelity values, while low SNR images require small fidelity numbers. In **Supplementary Note 8**, we have introduced a four-step procedure for parameters finetuning, five step-by-step examples of adjusting the sparsity and the fidelity to obtain optimal reconstructions, and more explanations on the background estimation in the end.

FRC resolution map and other metrics. FRC resolution is implemented to describe the effective resolution of the SR microscope. To visualize the FRC resolution more clearly, we applied the blockwise FRC resolution mapping described in[38] to evaluate our (Sparse) SIM and (Sparse) SD-SIM images. More specifically, each image is divided into independent blocks, and the local FRC value is calculated individually using the method

reported in[37]. If the FRC estimations in a block are sufficiently correlated, this region will be color-coded in the FRC resolution map. Otherwise, the region will be color-coded according to its neighbor interpolation. Note that before calculating the FRC resolution map of SD-SIM raw images in **Fig. 5a**, **5h**, and **6a**, the PURE denoise method[46] was applied in advance to images to avoid the ultralow SNR of SD-SIM raw images perturbing the FRC calculation. We also used the structural similarity (SSIM) values[60] and peak signal-to-noise ratio (PSNR) to evaluate the quality of reconstructions in **Extended Data Fig. 3**.

Synthetic filament structures under SIM imaging. We created synthetic filament structures using the *Random Walk* process and adopted the maximal curvatures in the program, generating the filament structures[61] (**Extended Data Fig. 3a**). To simulate time-lapse sequences of filament structures, we used a subpixel shift operation to generate a random shift in these filaments based on the *Markov chain* in the *t*-axis, resulting in an image stack of 128 × 128 × 5 pixels. To mimic SIM acquisition, these ground truth objects were illuminated by pattern excitation and convolved with a microscope PSF of (1.4 NA, 488 nm excitation, 32.5 nm pixel) to generate wide-field raw images. In addition to the filaments, we also included a background signal that combined the effects of cellular autofluorescence, and fluorescence emitted from the out-of-focus plane (simulated by the convolution of synthetic filaments with out-of-focus PSF 1 μm away from the focal plane). Moreover, we incorporated *Gaussian* noise with different variance extents (0%, 11%, 25%, 50%, 80%) to the peak fluorescence intensity of the filaments. The raw images were acquired by a camera with a pixel size of 65 nm and pixel amplitudes of 16 bits (**Extended Data Fig. 3b**).

The corrections of bead FWHMs and pore diameters. To extract FWHMs of fluorescent beads and linear structures and the double-Gaussian-peak in ring structures, we used the multiple-peak fit of the Gaussian function in OriginPro. When the sizes of system PSF and the size of camera pixel were comparable to the size of the structure been imaged, fitted diameters of punctated and ring-shaped structures differently deviated from their real values (**Fig. 2e**, **Extended Data Fig. 14c**, **Supplementary Fig. 23**, **24**, also detailed in

Supplementary Note 9). For narrowed fitted diameters of nuclear pores and fusion pores under the Sparse-SIM (**Fig. 2e**, **4q**), we corrected these values followed the protocol in **Supplementary Note 9.1**. For apparent enlarged sizes of fluorescent beads under the microscope (**Supplementary Fig. 24** and other details in **Supplementary Note 9.2**), we included a bead-size correction factor for the beads with the diameter of 100-nm to estimate the real resolution of Sparse SD-SIM (**Extended Data Fig. 14c**).

Mesh pore diameters of actin networks. We analyzed the mesh pore diameters (**Fig. 4h**) of actin networks based on the pipeline in[35]. Considering the low SNR condition and high background in 2D-SIM and SD-SIM images, we replaced the pre-transform[35, 62] with the pre-filter. Specifically, we used a Gaussian filter and an unsharp mask filter[63] to denoise the raw image and remove its background sequentially. To do so, we extracted the pores by Meyer watershed segmentation[64]. The pore sizes can then be calculated by the number of enclosed pixels from inverted binary images multiplied by the physical pixel size. It is worth noting that the Sparse-SIM and Sparse SD-SIM images can be segmented directly using hard thresholds due to their low backgrounds.

CCP diameters. Following the pipeline in[10], two main procedures are involved before calculating the CCP diameters in **Fig. 5a**. First, the image in **Fig. 5a** is segmented with the locally adaptive threshold[65] to segment the ring structures in the image. Second, the resulting binary images are processed by the Meyer watershed after distance transform to separate touching CCPs, and the goal is to generate a boundary as far as possible from the center of the overlapping CCPs[64]. Subsequently, the CCP diameters can be calculated in the same manner as the mesh pore diameters. Finally, a correction of the CCP dimeters is also included as the same to the protocol in **Supplementary Note 9.1**.

Pre-compensating for the skewed intensity distribution. Fluorescence images are prone to shading and vignetting effects, which may perturb later processing and analysis. Thus we chose BaSiC[66] as a pre-correction option before sparse deconvolution. BaSiC is based on a linear imaging model that relates the measured image, $I^{meas}(x)$ at location x, to its uncorrupted accurate correspondence, $I^{true}(x)$. Such linear model can be expressed

as $I^{meas}(x) = I^{true}(x) \times S(x) + D(x)$, where $S(x)$ represents the change in effective illumination across an image (known as flat-field), and the additive term $D(x)$ (known as the dark-field) is dominated by the camera offset and its thermal noise that are present even in the absence of incident light. BaSiC estimates the $S(x)$ and $D(x)$ by low rank and sparse decomposition to correct the shading in space and background variations in time. We employed BaSiC to correct the uneven illumination to avoid removing weak signals at the edge of the FOV in the following deconvolution process (**Supplementary Fig. 21b-21e**). However, we shall be cautious in using such a correction step, avoiding overcorrected and degraded images.

Image rendering and processing. The color map SQUIRREL-FRC[38] associated with ImageJ was used to present the FRC map in **Fig. 4e**. The color map Morgenstemning[67] was applied to show lysosomes in **Fig. 5h,** and the Fourier transform results in **Fig. 6d**, **Extended Data Fig. 5b**, **5d**, **7a**, **18c**, and **20b-20d**. The 16-color projection was used to show the depth in **Fig. 5k**. The jet projection was used to show the depth in **Fig. 6k** and **Extended Data Fig. 20a-20d**, time series in **Fig. 5g**, **Extended Data Fig. 15a**, and **15b**, and RSE error map[38] in **Extended Data Fig. 12e**, and **12f**. The volumes in **Fig. 6h**, **Supplementary Video 11**, and **13** were rendered by ClearVolume[68]. The volume in **Supplementary Video 18** was rendered by 3Dscript[69]. All data processing was achieved using MATLAB and ImageJ. All the figures were prepared with MATLAB, ImageJ, Microsoft Visio, and OriginPro, and videos were all produced with our light-weight MATLAB framework, which is available at https://github.com/WeisongZhao/img2vid.

The adaptive filter for SD-SIM. Confocal-type images often exhibit isolated pixels (1×1 ~ 5×5) with extremely bright values caused by voltage instability or dead/hot camera pixels. The magnitudes of these pixels are approximately 5 to 100 times higher than the normal intensity amplitudes of the biostructure. These isolated pixels are ill-suited for the sparse reconstruction. Unlike the method in[61], which used percentage image normalization to overcome this problem, we created an adaptive median filter to remove these improper pixels. More specifically, instead of the normal median filter, which replaces each pixel with the median of

the neighboring pixels in the window, we set a threshold for our developed adaptive median filter. If the pixel intensity is larger than ***threshold*** × ***median in the window***, the pixel is replaced by the median; otherwise, the window moves to the next pixel. By using this method, we can filter the isolated pixels without blurring the images. The related method has been written as an ImageJ plug-in and can be found at https://github.com/WeisongZhao/AdaptiveMedian.imagej.

GPU acceleration. We implemented Sparse-SIM in MATLAB using a CPU (Intel i9-7900X, 3.3 GHz, 10 cores, 20 threads, and 128 GB memory), the NVIDIA CUDA fast Fourier transform library (cuFFT), and a Graphics Processing Unit (GPU, TITAN RTX, 4608 CUDA cores and 24 GB memory). The FFT was utilized to accelerate the high-content and multidimensional matrix convolution operation in Sparse-SIM. Under the premise that the GPU memory is sufficient for the input data, acceleration becomes more evident as the data's size increases. In most circumstances, a 60-fold improvement was achieved with GPU acceleration compared to Central Processing Unit (CPU) processing. For example, the image dataset of 1536 × 1536 × 20 in **Fig. 4a** required ~90 s to process with the GPU, far less than 46 mins needed for processing with the CPU. The full list for CPU/GPU computing time of data in **Fig. 2-5** can be found in **Supplementary Table 5**.

Data availability. Raw image datasets from **Fig. 4a**, **4m**, **4j**, **6e**, and **Extended Data Fig. 15** can be found at https://github.com/WeisongZhao/Sparse-SIM/releases/download/v1.0.3/DATA.zip. All other data that support the findings of this study are available from the corresponding author on request.

Code availability. The version of Sparse-SIM software used in this manuscript (accompanied with user manual) is available as **Supplementary Software**. The readily usable executable binary files for Windows (.EXE) and Mac (.APP) operating systems are at https://github.com/WeisongZhao/Sparse-SIM/releases/tag/v1.0.3. The updated version of the source code can be found at https://github.com/WeisongZhao/Sparse-SIM.

REFERENCES

1. Nixon-Abell, J. et al. Increased spatiotemporal resolution reveals highly dynamic dense tubular matrices in the peripheral ER. *Science* **354**, aaf3928 (2016).
2. Valm, A.M. et al. Applying systems-level spectral imaging and analysis to reveal the organelle interactome. *Nature* **546**, 162-167 (2017).
3. Hess, S.T. et al. Dynamic clustered distribution of hemagglutinin resolved at 40 nm in living cell membranes discriminates between raft theories. *Proceedings of the National Academy of Sciences of the United States of America* **104**, 17370-17375 (2007).
4. Shroff, H., Galbraith, C.G., Galbraith, J.A. & Betzig, E. Live-cell photoactivated localization microscopy of nanoscale adhesion dynamics. *Nat Methods* **5**, 417-423 (2008).
5. Westphal, V. et al. Video-rate far-field optical nanoscopy dissects synaptic vesicle movement. *Science* **320**, 246-249 (2008).
6. Zhu, L., Zhang, W., Elnatan, D. & Huang, B. Faster STORM using compressed sensing. *Nature Methods* **9**, 721-723 (2012).
7. Shin, W. et al. Visualization of Membrane Pore in Live Cells Reveals a Dynamic-Pore Theory Governing Fusion and Endocytosis. *Cell* **173**, 934-945 (2018).
8. Godin, A.G., Lounis, B. & Cognet, L. Super-resolution microscopy approaches for live cell imaging. *Biophysical Journal* **107**, 1777-1784 (2014).
9. Huang, X. et al. Fast, long-term, super-resolution imaging with Hessian structured illumination microscopy. *Nature biotechnology* **36**, 451-459 (2018).
10. Li, D. et al. Extended-resolution structured illumination imaging of endocytic and cytoskeletal dynamics. *Science* **349**, aab3500 (2015).
11. Guo, Y. et al. Visualizing Intracellular Organelle and Cytoskeletal Interactions at Nanoscale Resolution on Millisecond Timescales. *Cell* **175**, 1430-1442 (2018).
12. Wolter, H. On basic analogies and principal differences between optical and electronic information, Vol. 1. (Elsevier, 1961).
13. Harris, J.L. Diffraction and resolving power. *Journal of the Optical Society of America* **54**, 931-936 (1964).
14. Goodman & W, J. Introduction to Fourier optics. (Roberts and Company Publishers, 2005).
15. Lindberg, J. Mathematical concepts of optical superresolution. *Journal of Optics* **14**, 083001 (2012).
16. Bertero, M. & De Mol, C. Super-Resolution by Data Inversion, Vol. 36. (Elsevier, 1996).
17. Richardson, W.H. Bayesian-based iterative method of image restoration. *Journal of The Optical Society of America A* **62**, 55-59 (1972).
18. Lucy, L.B. An iterative technique for the rectification of observed distributions. *The Astronomical Journal* **79**, 745 (1974).
19. Lucy, L.B. Resolution limits for deconvolved images. *The Astronomical Journal* **104**, 1260-1265 (1992).
20. Puschmann, K.G. & Kneer, F. On super-resolution in astronomical imaging. *Astronomy & Astrophysics* **436**, 373-378 (2005).
21. Gazit, S., Szameit, A., Eldar, Y.C. & Segev, M. Super-resolution and reconstruction of sparse sub-wavelength images. *Optics Express* **17**, 23920-23946 (2009).
22. Demanet, L. & Nguyen, N. The recoverability limit for superresolution via sparsity. *Preprint at*, https://arxiv.org/abs/1502.01385 (2015).
23. Fannjiang, A.C. Compressive imaging of subwavelength structures. *SIAM Journal on Imaging Sciences* **2**, 1277-1291 (2009).
24. Schulz, O. et al. Resolution doubling in fluorescence microscopy with confocal spinning-disk image scanning microscopy. *Proceedings of the National Academy of Sciences of the United States of America* **110**, 21000-21005 (2013).

25. Zong, W. et al. Fast high-resolution miniature two-photon microscopy for brain imaging in freely behaving mice. *Nature Methods* **14**, 713-719 (2017).
26. Sun, D.-E. et al. Click-ExM enables expansion microscopy for all biomolecules. *Nature Methods* **18**, 107–113 (2021).
27. Dey, N. et al. Richardson–Lucy algorithm with total variation regularization for 3D confocal microscope deconvolution. *Microscopy research and technique* **69**, 260-266 (2006).
28. Laasmaa, M., Vendelin, M. & Peterson, P. Application of regularized Richardson–Lucy algorithm for deconvolution of confocal microscopy images. *Journal of Microscopy* **243**, 124-140 (2011).
29. Candes, E.J. & Tao, T. Near-optimal signal recovery from random projections: Universal encoding strategies? *IEEE Transactions on Information Theory* **52**, 5406-5425 (2006).
30. Hoffman, D.P., Slavitt, I. & Fitzpatrick, C.A. The promise and peril of deep learning in microscopy. *Nature Methods* **18**, 131–132 (2021).
31. Belthangady, C. & Royer, L.A. Applications, promises, and pitfalls of deep learning for fluorescence image reconstruction. *Nature Methods* **16**, 1215-1225 (2019).
32. Szymborska, A. et al. Nuclear pore scaffold structure analyzed by super-resolution microscopy and particle averaging. *Science* **341**, 655-658 (2013).
33. Ma, J., Kelich, J.M., Junod, S.L. & Yang, W. Super-resolution mapping of scaffold nucleoporins in the nuclear pore complex. *Journal of Cell Science* **130**, 1299-1306 (2017).
34. Gottfert, F. et al. Strong signal increase in STED fluorescence microscopy by imaging regions of subdiffraction extent. *Proceedings of the National Academy of Sciences of the United States of America* **114**, 2125-2130 (2017).
35. Xia, S. et al. Nanoscale Architecture of the Cortical Actin Cytoskeleton in Embryonic Stem Cells. *Cell reports* **28**, 1251-1267 (2019).
36. Szameit, A. et al. Sparsity-based single-shot subwavelength coherent diffractive imaging. *Nature materials* **11**, 455-459 (2012).
37. Nieuwenhuizen, R.P. et al. Measuring image resolution in optical nanoscopy. *Nature Methods* **10**, 557 (2013).
38. Culley, S. et al. Quantitative mapping and minimization of super-resolution optical imaging artifacts. *Nature Methods* **15**, 263 (2018).
39. Ornberg, R.L. & Reese, T.S. Beginning of exocytosis captured by rapid-freezing of Limulus amebocytes. *The Journal of Cell Biology* **90**, 40 - 54 (1981).
40. Wurm, C.A. et al. Nanoscale distribution of mitochondrial import receptor Tom20 is adjusted to cellular conditions and exhibits an inner-cellular gradient. *Proceedings of the National Academy of Sciences of the United States of America* **108**, 13546-13551 (2011).
41. York, A.G. et al. Instant super-resolution imaging in live cells and embryos via analog image processing. *Nature Methods* **10**, 1122-1126 (2013).
42. York, A.G. et al. Resolution doubling in live, multicellular organisms via multifocal structured illumination microscopy. *Nature Methods* **9**, 749-754 (2012).
43. Muller, C.B. & Enderlein, J. Image scanning microscopy. *Physical review letters* **104**, 198101 (2010).
44. Theer, P., Mongis, C. & Knop, M. PSFj: know your fluorescence microscope. *Nature Methods* **11**, 981-982 (2014).
45. Saffarian, S., Cocucci, E. & Kirchhausen, T. Distinct dynamics of endocytic clathrin-coated pits and coated plaques. *PLoS biology* **7**, e1000191 (2009).
46. Luisier, F., Vonesch, C., Blu, T. & Unser, M. Fast interscale wavelet denoising of Poisson-corrupted images. *Signal Processing* **90**, 415-427 (2010).
47. Chu, B.B. et al. Cholesterol transport through lysosome-peroxisome membrane contacts. *Cell* **161**, 291-306 (2015).
48. Wang, Y., Yang, J., Yin, W. & Zhang, Y. A new alternating minimization algorithm for total variation image reconstruction. *SIAM Journal on Imaging Sciences* **1**, 248-272 (2008).
49. Xue, J.Z. & Funabiki, H. Nuclear assembly shaped by microtubule dynamics. *Nucleus* **5**, 40-46 (2014).
50. Cox, c.I. & Sheppard, C. Information capacity and resolution in an optical system. *Journal of The Optical Society of America A* **3**, 1152-1158 (1986).

51. Descloux, A., Grußmayer, K.S. & Radenovic, A. Parameter-free image resolution estimation based on decorrelation analysis. *Nature Methods* **16**, 918-924 (2019).
52. Zhang, Y. et al. Mitochondria determine the sequential propagation of the calcium macrodomains revealed by the super-resolution calcium lantern imaging. *Science China Life Sciences*, 1 - 9 (2020).
53. Mo, Y., Feng, F., Mao, H., Fan, J. & Chen, L. Structured illumination microscopy artifacts caused by illumination scattering. *Preprint at bioRxiv*, https://doi.org/10.1101/2021.1101.1101.425033 (2021).
54. Douglas, S.M. et al. Rapid prototyping of 3D DNA-origami shapes with caDNAno. *Nucleic acids research* **37**, 5001-5006 (2009).
55. Kim, D.-N., Kilchherr, F., Dietz, H. & Bathe, M. Quantitative prediction of 3D solution shape and flexibility of nucleic acid nanostructures. *Nucleic acids research* **40**, 2862-2868 (2012).
56. Castro, C.E. et al. A primer to scaffolded DNA origami. *Nature Methods* **8**, 221-229 (2011).
57. Gu, L. et al. Molecular resolution imaging by repetitive optical selective exposure. *Nature Methods* **16**, 1114-1118 (2019).
58. Tillberg, P. et al. Protein-retention expansion microscopy of cells and tissues labeled using standard fluorescent proteins and antibodies. *Nature biotechnology* **34**, 987-992 (2016).
59. Thévenaz, P., Ruttimann, U.E. & Unser, M. A pyramid approach to subpixel registration based on intensity. *IEEE Transactions on Image Processing* **7 1**, 27-41 (1998).
60. Wang, Z., Bovik, A.C., Sheikh, H.R. & Simoncelli, E.P. Image quality assessment: from error visibility to structural similarity. *IEEE Transactions on Image Processing* **13**, 600-612 (2004).
61. Weigert, M. et al. Content-aware image restoration: pushing the limits of fluorescence microscopy. *Nature Methods* **15**, 1090 (2018).
62. Zhang, Z., Nishimura, Y. & Kanchanawong, P. Extracting microtubule networks from superresolution single-molecule localization microscopy data. *Molecular biology of the cell* **28**, 333-345 (2017).
63. De Vries, F.P. Automatic, adaptive, brightness independent contrast enhancement. *Signal Processing* **21**, 169-182 (1990).
64. Meyer, F. & Beucher, S. Morphological segmentation. *Journal of visual communication and image representation* **1**, 21-46 (1990).
65. Yanowitz, S.D. & Bruckstein, A.M. A new method for image segmentation. *Computer Vision, Graphics, and Image Processing* **46**, 82-95 (1989).
66. Peng, T. et al. A BaSiC tool for background and shading correction of optical microscopy images. *Nature Communications* **8**, 14836 (2017).
67. Geissbuehler, M. & Lasser, T. How to display data by color schemes compatible with red-green color perception deficiencies. *Optics Express* **21**, 9862-9874 (2013).
68. Royer, L.A. et al. ClearVolume: open-source live 3D visualization for light-sheet microscopy. *Nature Methods* **12**, 480 (2015).
69. Schmid, B. et al. 3Dscript: animating 3D/4D microscopy data using a natural-language-based syntax. *Nature Methods* **16**, 278-280 (2019).

Acknowledgments: We thank Profs. Bertil Hille and Chris Xu for their reading and critical comments on the manuscript. We thank Profs. Michael Knop and Patrick Theer for their feedback and valuable discussions of the bead-correction factor, Profs. Chuanmao Zhang and Jiong Ma for the sharing of nuclear pore vectors. The work was supported by grants from the National Natural Science Foundation of China (81925022, 91854112,

91750203, 31570839, 31327901, 31521062, 61805057), the National Science and Technology Major Project Program (2016YFA0500400), the Beijing Natural Science Foundation (L172003, 7152079, 5194026), the National Postdoctoral Program for Innovative Talents (BX201800008), China Postdoctoral Science Foundation (2019M650329), Young Elite Scientists Sponsorship Program (2018QNRC001) and the High-performance Computing Platform of Peking University.

Author contributions: L. C. and H. L. conceived and supervised the research; W. Z., S. Z., L. L., X. H., S. X., Y. Z., C. S., and R. W. performed the experiments; W. Z., G. H., Z. H., J. W., R. C, and Y. M. performed the simulations and theoretical analysis; W. Z. wrote the algorithm software with the contribution of J. W; W. Z., S. Z., and L. L. analyzed the data; W. Z., S. Z., and L. L. prepared the figures and videos; B. S., J. X. provided some of the reagents and participated in some of the discussions; Y. S. and S. Z. prepared the DNA origami samples under the supervision of B. D. and W. J. respectively; D. S. prepared the expansion samples under the supervision of X. C.; Y. L., H. M., J. T., J. L., H. L., B. S., and L.C. participated in discussions during the development of the manuscript. L. C., H. L., and W. Z. wrote the manuscript. All of the authors participated in discussions and data interpretation.

Competing interests: The authors declare no competing financial interests.

FIGURES

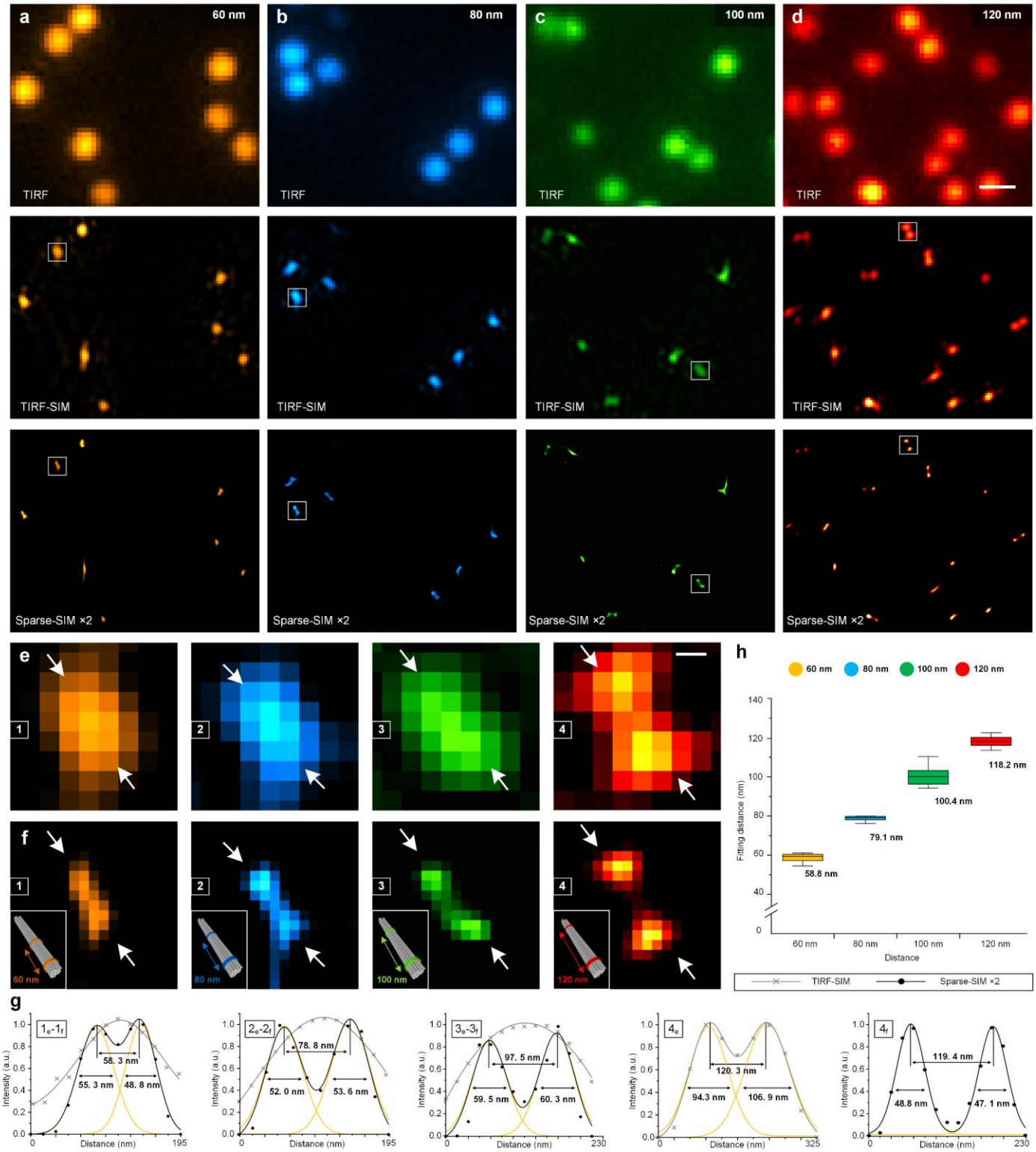

Fig. 1 | Evaluating Sparse-SIM with DNA origami samples. (**a**-**d**) DNA origami samples (**Method**) with 60 nm (**a**), 80 nm (**b**), 100 nm (**c**), and 120 nm (**d**) designed distances imaged by TIRF (top), TIRF-SIM (middle), and Sparse-SIM ×2 (bottom) configurations. (**e**, **f**) Enlarged regions enclosed by the white boxes in (**a**-**d**) under TIRF-SIM (**e**) and Sparse-SIM ×2 (**f**) configurations. (**g**) Corresponding intensity profiles and multiple Gaussian fitting of the DNA origami structures indicated by the white arrows in (**e**), respectively. The numbers represent the FWHM and distance between peaks. (**h**) Average fitted distances of different DNA origami samples. Each measurement was repeated 12 times. Scale bars: (**d**) 500 nm; (**e**) 50 nm.

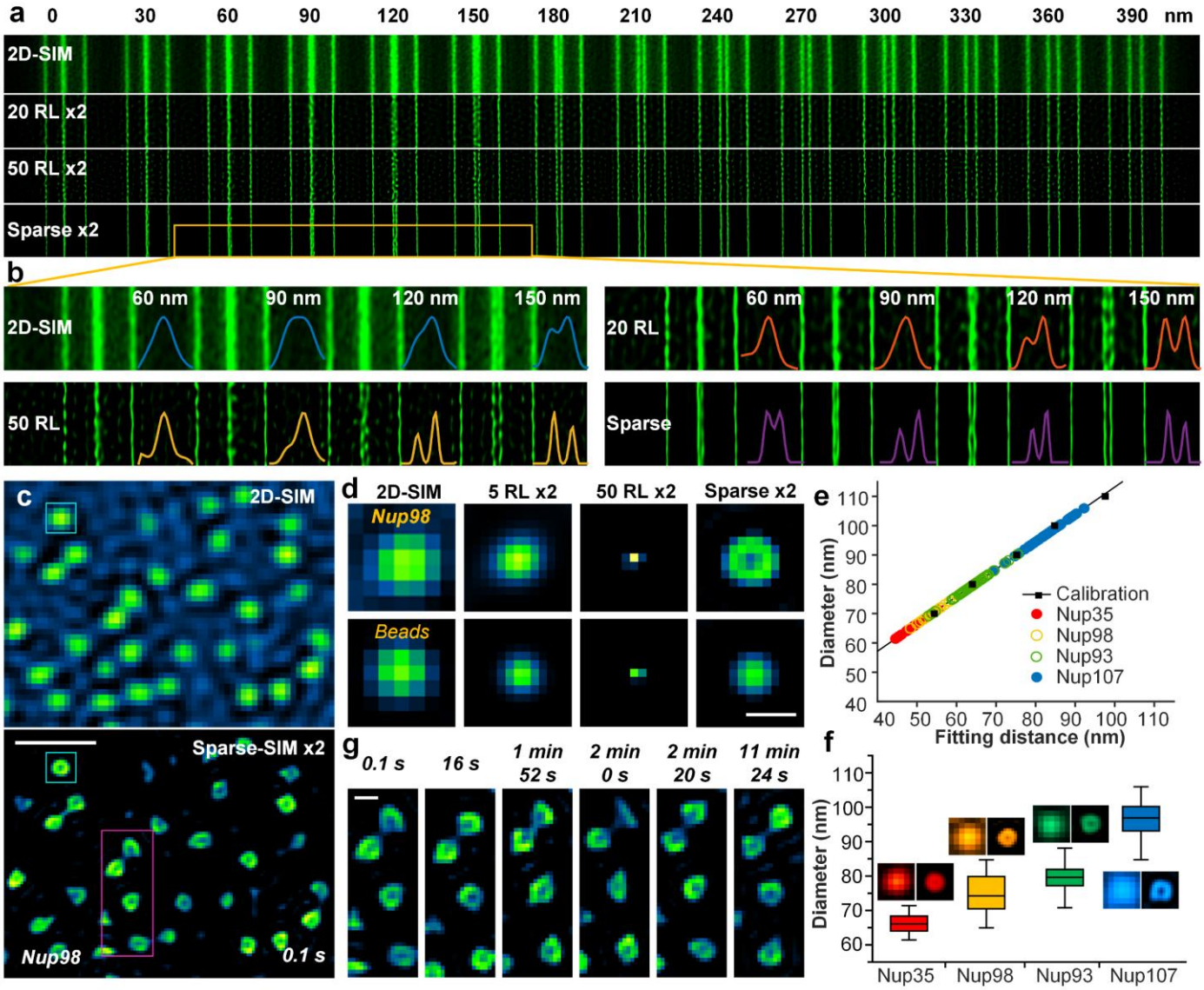

Fig. 2 | Sparse-SIM resolves known structures of ~60 nm in size. (**a-b**) Separation of two fluorescent lines with interline spacing down to 60 nm by the Sparse-SIM. Raw images were either reconstructed with Wiener algorithm (2D-SIM), or Fourier interpolated before reconstructed with Wiener algorithm followed by Fourier interpolated before reconstructed with the RL deconvolution for 20 (20 RL × 2), 50 (50 RL × 2) iterations, or the Sparse deconvolution pipeline (Sparse ×2) (**a**). The region enclosed by the yellow box was magnified and shown in (**b**). (**c**) A representative example of dynamic ring-shaped nuclear pores labeled with Nup98-GFP in a live COS-7 cell was observed with Sparse-SIM for more than ten mins. Images under the 2D-SIM and the Sparse-SIM ×2 configurations were shown in the upper and bottom panels, respectively. (**d**) The snapshot of the nuclear pore structure enclosed by the cyan box in **c** was compared with a 100-nm fluorescent bead under different reconstruction methods (2D-SIM, 20 RL × 2, 50 RL × 2, Sparse ×2). (**e**) Because the sizes of nuclear pores were comparable to the resolution of Sparse-SIM and the size of the pixel, we followed the protocol in **Supplementary Note 9.1** to derive the actual diameters of nuclear pore structures labeled by Nup35-GFP (red), Nup98-GFP (yellow), Nup93-GFP (green), and Nup107-GFP (cyan), respectively. (**f**) Average diameters of rings formed by Nup35 (66 ± 3 nm, n = 30 from 3 cells), Nup98 (75 ± 6 nm, n = 40 from 3 cells), Nup93 (79 ± 4 nm, n = 40 from 3 cells), or Nup107 (97 ± 5 nm, n = 40 from 3 cells). Left and right montages showed the results after Wiener reconstruction or Sparse deconvolution. (**g**) The magenta box in (**c**) is enlarged and shown at six time points. Scale bars: (**c**) 500 nm; (**d**, **g**) 100 nm.

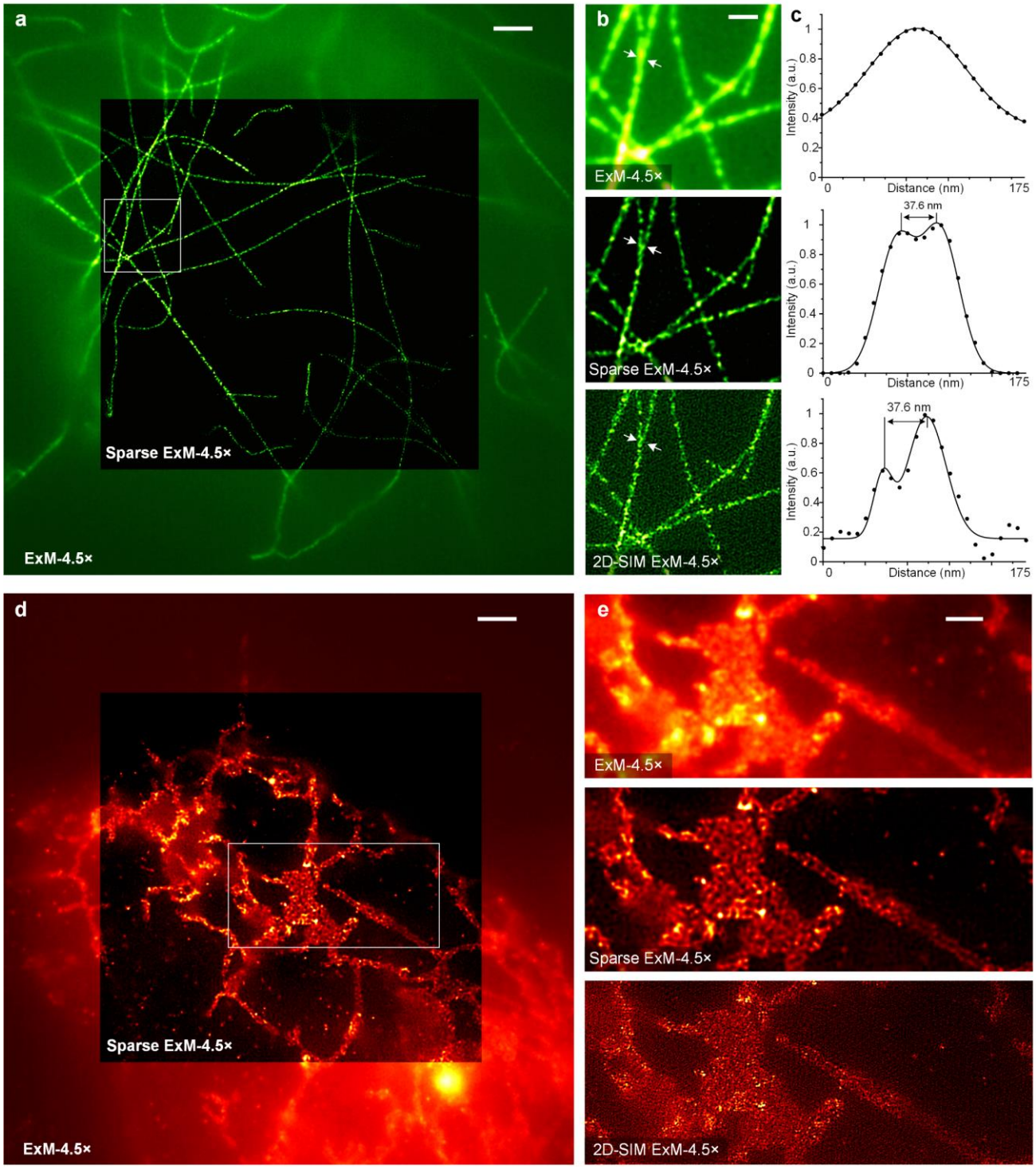

Fig. 3 | Sparse deconvolution assisted expansion microscopy (Sparse-ExM). (**a**) The COS-7 cell was immunostained with a primary antibody against α-tubulin, and a second antibody conjugated with AF488. We showed the 4.5 times expanded cell (ExM-4.5×) in the background and the Sparse ExM-4.5× image in the center. (**b**) Magnified views of the regions in (**a**) under ExM-4.5×, Sparse ExM-4.5×, and ExM-4.5× under the 2D-SIM (2D-SIM ExM-4.5×). (**c**) Intensity profiles and multiple Gaussian fitting of the filaments are indicated by the white arrows in (**c**), respectively. The numbers represent the distances between peaks. (**d**) ExM images of Sec61β-GFP in a COS-7 cell. We showed the 4.5 times expanded cell (ExM-4.5×) in the background and the Sparse ExM-4.5× image in the center. (**e**) Enlarged regions enclosed by the white box in (**a**) seen under ExM-4.5×, Sparse ExM-4.5×, and 2D-SIM ExM-4.5×. (**f**) Highlighted regions from white boxes in (**e**). Scale bars: (**a**, **d**) 1 μm; (**b**) 300 nm; (**e**) 500 nm; (**f**) 200 nm.

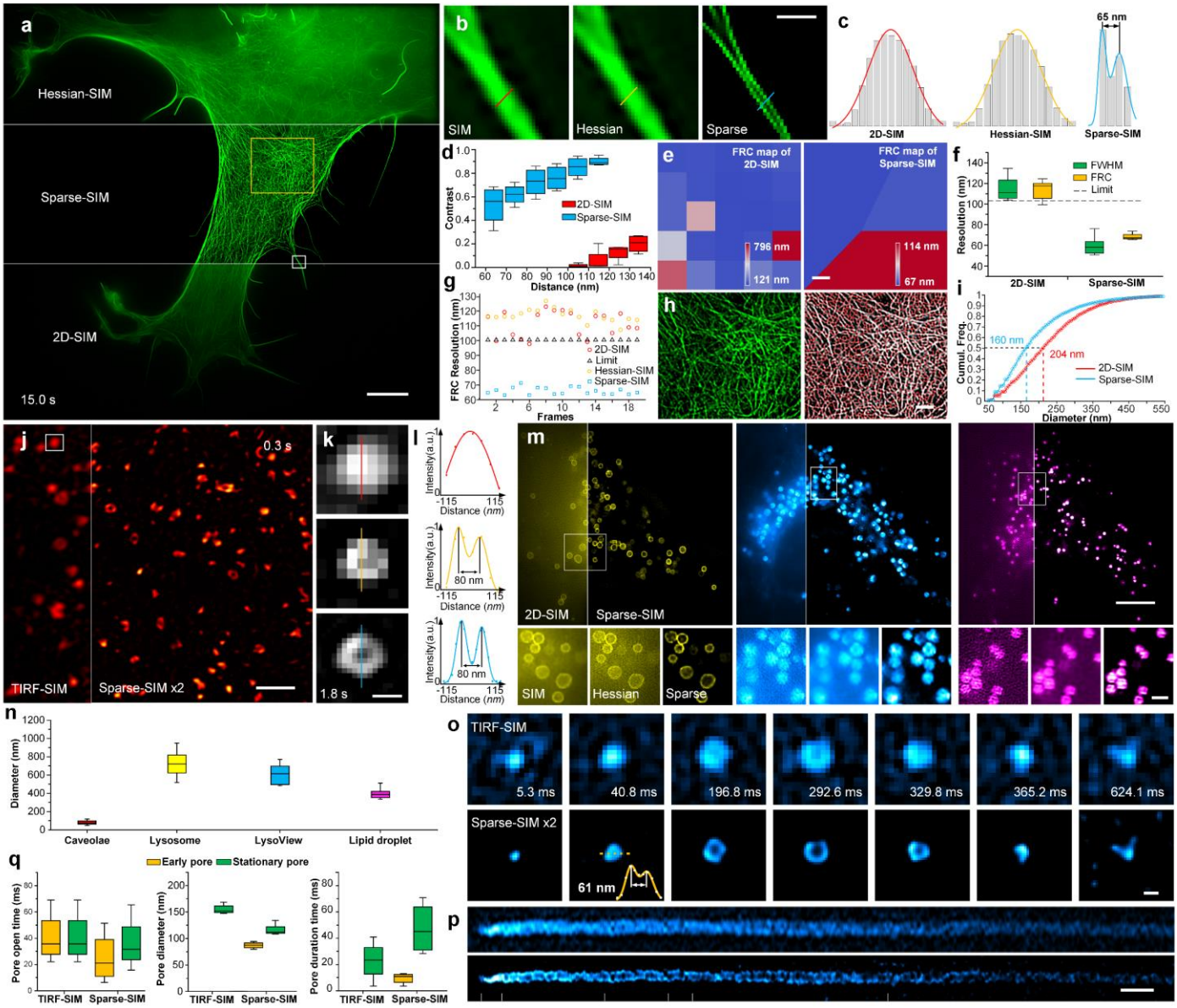

Fig. 4 | Sparse-SIM achieves ~60 nm and millisecond spatiotemporal resolution in live cells. **(a)** A representative COS-7 cell labeled with LifeAct-EGFP. **(b-c)** Enlarged regions enclosed by the white box in **a** (**b**), and the corresponding profiles along lines (**c**). Each box in (**c**) denotes the intensity of one pixel. **(d)** Average contrasts of two peaks with different distances. **(e)** FRC maps of actin filaments. **(f)** Resolutions measured as the FWHMs and by the FRC. **(g)** Time-dependent minimal FRC resolutions. Black triangles represent the theoretical resolution limit of 2D-SIM. **(h)** The magnified view of actin filaments in the yellow box from **(a)** (left) and the segmented version (right, **Method**). **(i)** Cumulative distributions of pore sizes within the actin meshes in **(h)**. **(j)** A representative COS-7 cell labeled with caveolin-EGFP. **(k-l)** From top to bottom are magnified views of the white box in **(j)** reconstructed by TIRF-SIM, Sparse-SIM, and Sparse-SIM ×2 with upsampling (**k**), and their fluorescence profiles are shown in **(l)**. **(m)** Lysosomes were labeled with LAMP1-EGFP (left, yellow) or LysoView (middle, cyan), while lipid droplets were labeled with LipidSpot (right, magenta). **(n)** Average diameters of different vesicles**. (o)** Representative montages of a vesicle fusion event. **(p)** Kymographs from lines in TIRF-SIM (upper) and Sparse-SIM ×2 (lower) images are shown in **(o)**. **(q)** Average opening time (left), diameters (middle), and duration time of early (yellow) and stationary (green) fusion pores (right). Centerline, medians; limits, 75% and 25%; whiskers, maximum and minimum; error bars, s.e.m.; Cumul. Freq., cumulative frequency; scale bars: **(a**, **e**, and **m** top**)** 5 μm; **(b** and **j)** 500 nm; **(h** and **m** bottom**)** 1 μm; **(k, o)** 100 nm; **(p)** 500 ms.

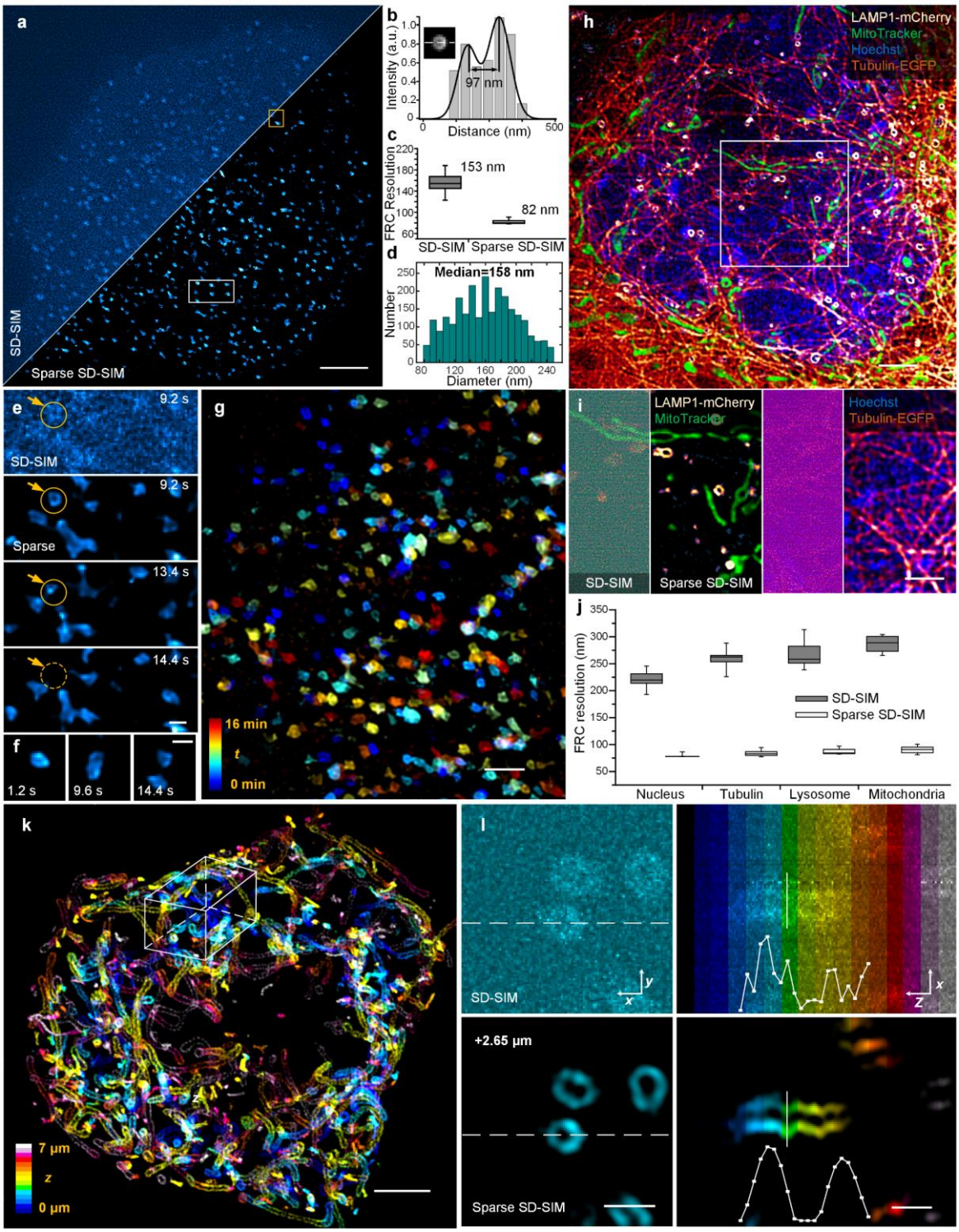

Fig. 5 | Sparse SD-SIM enables three-dimensional, multi-color, and sub-90-nm resolution for live-cell SR imaging. (**a**) A snapshot of CCPs in a COS-7 cell. (**b**) The profile corresponding to the resolved central ring of the CCP. (**c**) Average minimal resolutions by the FRC method. (**d**) Histogram of the diameters of CCPs. (**e-f**) Magnified view of the white boxed region (**e**) and yellow boxed region (**f**) in (**a**). (**g**) Temporal projections of CCPs within 16 mins. (**h**) A representative example of four-color (LAMP1-mCherry, yellow; MitoTracker, green; Hoechst, blue; Tubulin-EGFP, brown), live-cell SR imaging. (**i**) Magnified view of the white boxed region in (**h**). (**j**) Average resolutions by the FRC method. (**k**) Three-dimensional distributions of all mitochondria (labeled with TOM20-mCherry) of a live COS-7 cell. (**l**) Color-coded horizontal (left) and vertical sections (right) from the white boxed region in (**k**). Centerline, medians; limits, 75% and 25%; whiskers, maximum and minimum; error bars, s.e.m; scale bars: (**a**, **i**) 3 μm; (**e**, **f**) 300 nm; (**g**, **l**) 1 μm; (**h**, **k**) 5 μm.

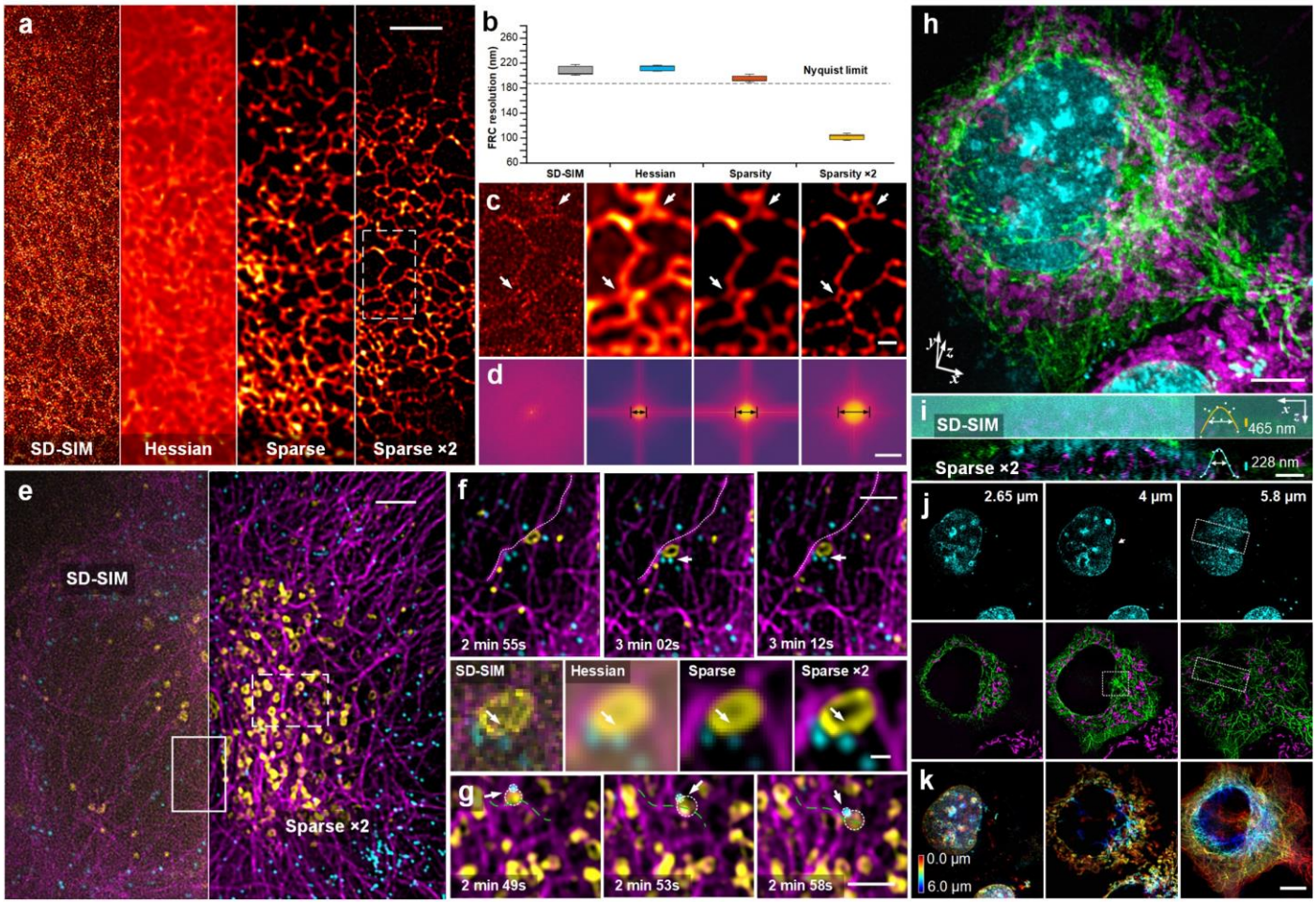

Fig. 6 | Upsampling enables Sparse SD-SIM to overcome the Nyquist sampling limit to achieve multi-color 3D SR imaging in live cells. (**a**) ER tubules in a COS-7 cell seen under different configurations. (**b**) Average resolutions by the FRC method. (**c**) Magnified views of ER tubules from (**a**). (**d**) Fourier transforms of images. Black arrows indicate the OTFs of corresponding images. (**e**) A snapshot of a HeLa cell labeled with tubulin-EGFP (magenta), Pex11a-BFP (cyan), and Lamp1-mCherry (yellow). (**f**) Magnified views in (**e**). As highlighted by white arrows in the bottom panel, only Sparse SD-SIM ×2 can dissect the lysosome's deformation by a neighboring peroxisome. (**g**) Time-lapse images of another example of the co-movement of both a lysosome and a peroxisome along a microtubule. (**h**) Live-cell three-color (Tubulin-EGFP, green; Hoechst, cyan; MitoTracker Deep Red, magenta) 3D imaging by Sparse SD-SIM ×2. (**i**) The *z*-axial view from (**h**). (**j**) Three horizontal sections of the cellular nucleus (top) and mitochondria merged with microtubules (bottom). (**k**) Color-coded volumes of nuclei, mitochondria, and microtubules. Scale bars: (**a**, **d**, **e**, **h**, **i**, **j**, and **k**) 5 μm; (**b** and **f** top, and **g**) 3 μm; (**c**) 1 μm; (**f** middle and bottom) 500 nm.

EXTENDED DATA FIGURES

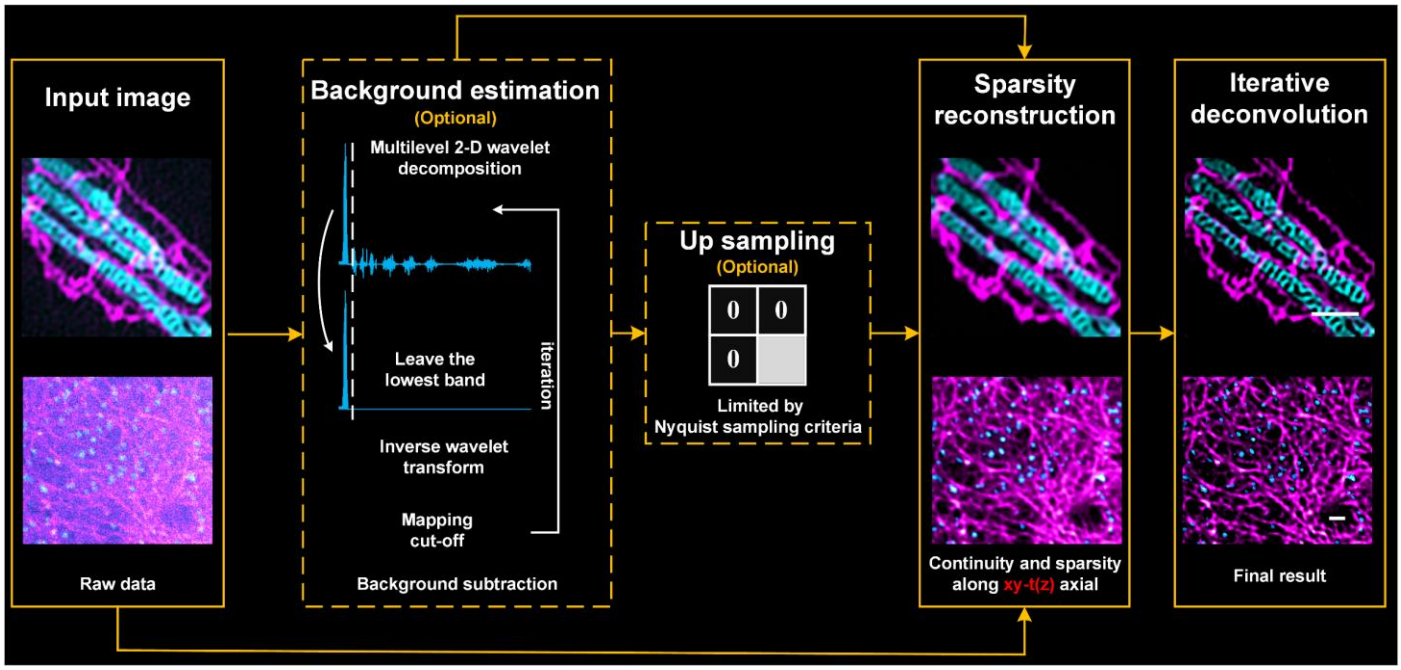

Extended Data Fig. 1 | Flowchart of the sparse deconvolution. Raw images from 2D-SIM or SD-SIM microscopes were background subtracted (optional operation), upsampled (optional operation), and reconstructed with the sparsity and the continuity a priori information along the *xy*-*t*(*z*) axes before the final iterative deconvolution. Scale bars: 1 μm.

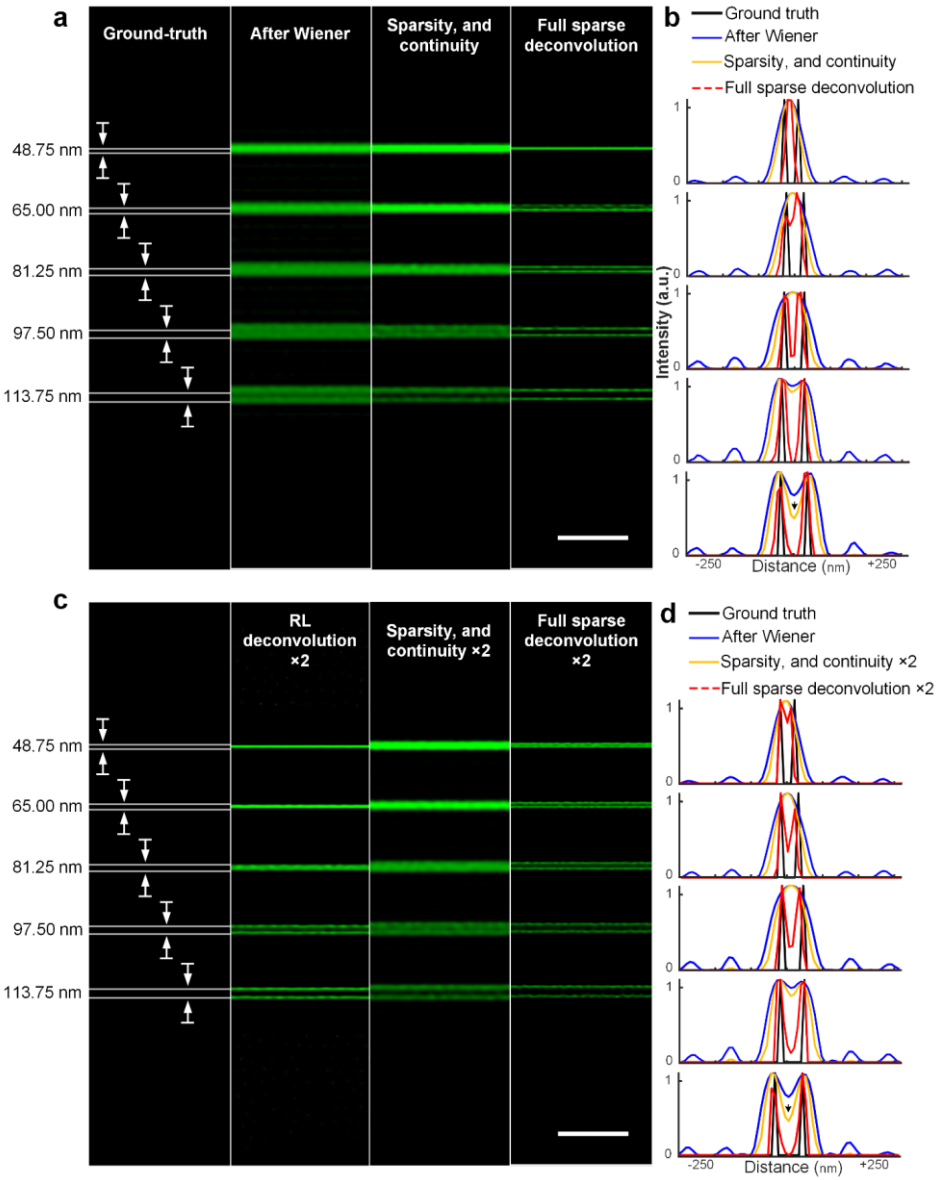

Extended Data Fig. 2 | Benchmark of spatial resolution at different steps of sparse deconvolution according to the synthetic images. (**a**) The resolution plate with a pixel size of 16.25 nm, which contained five pairs of lines at distances of 48.75 nm, 65.00 nm, 81.25 nm, 97.50 nm, and 113.75 nm. The synthetic image (512 × 512 pixels) is first illuminated by pattern excitation and then convolved with a microscope PSF of (1.4 NA, 488 nm excitation). The signal is recorded with an sCMOS camera with a pixel size of 65 nm, which meant 4× downsampling of the original image (128×128 pixels). We also included *Gaussian* noise with a variance of 5% of the peak intensity of the line to the raw image. Next, (from left to right) we used inverse Wiener filtering to obtain a conventional SIM image (256 × 256 pixels), followed by the reconstruction constrained by continuity and sparsity a priori information and final deconvolution. The theoretical limit resolution of Wiener SIM was calculated to be 97.6 nm by following the equation $\lambda/2(NA_i+NA_d)$, in which i and d respectively represent the illumination and detection NA. (**b**) The corresponding intensities across different pairs of lines in (**a**) are shown here. Two lines separated by 65 nm could be resolved only when the raw image underwent the full sparse deconvolution pipeline. (**c**) We also upsampled the SIM image obtained after Wiener inverse filtering to 512 × 512 pixels and processed it with RL deconvolution (20 iterations), and other steps in the sparse deconvolution pipeline thereafter. (**d**) The corresponding intensities across different pairs of lines in (**c**) are shown here. Note that two lines 48.75 nm apart could be separated by sparse deconvolution in the upsampled image. Scale bars: 1 μm.

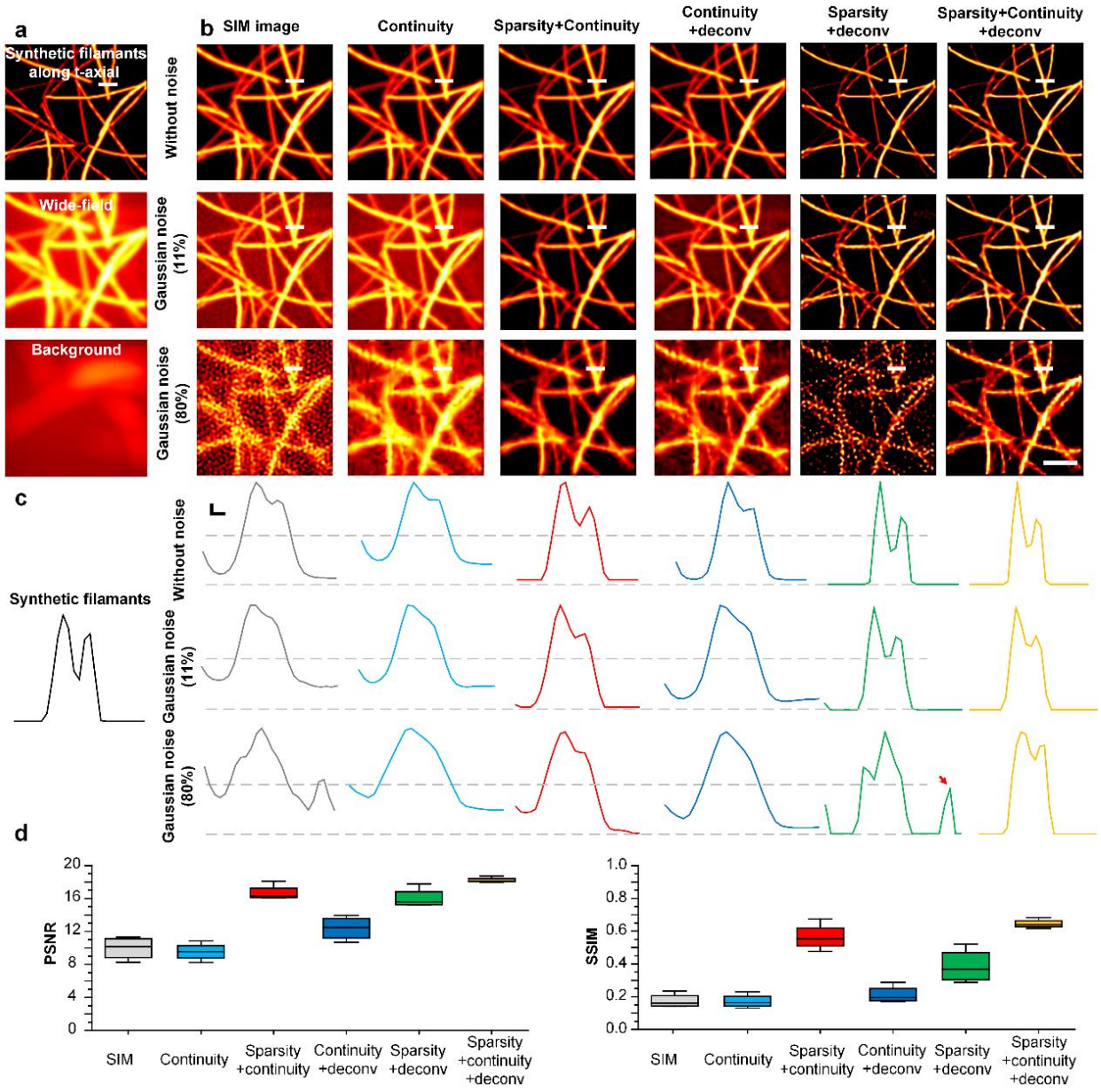

844

845 **Extended Data Fig. 3 | Contributions of different steps in sparse deconvolution of synthetic images**
846 **corrupted with different noise extents.** (**a**) From top to bottom: the ground-truth filament structures,
847 corresponding wide-field image, and out-of-focus background (**Method**). (**b**) Performance comparisons
848 among five different types of SR reconstructions at 0% 11% and 80% noise levels (from top to bottom).
849 Specifically, the raw images were reconstructed with inverse Wiener filtering (column 1), followed by
850 continuity-constraint reconstruction only (column 2), sparsity-plus-continuity-constraint reconstruction
851 (column 3), continuity-constraint reconstruction and deconvolution (column 4), sparsity-constraint
852 reconstruction only and deconvolution (column 5), or sparsity-plus-continuity-constraint reconstruction and
853 deconvolution (column 6). (**c**) The fluorescence intensity profiles along the two opposing synthetic filaments
854 in (**b**) under different conditions. While the continuity reconstruction followed by the deconvolution did not
855 separate these filaments, the sparsity reconstruction followed by the deconvolution caused artifacts (an
856 example indicated by the asterisk) in raw images with 80% noise. (**d**) Compared to the synthetic ground truth,
857 the average structural similarity (SSIM) values[60] and peak signal-to-noise ratio (PSNR) of SR images
858 reconstructed with different methods from raw images corrupted with different levels of noise (0%, 11%, 25%,
859 50%, and 80%). More details are given in **Supplementary Tables 1** and **2**. Scale bars: (**a**) 1 μm; (**c**) axial: 0.1
860 arbitrary units (a.u.); lateral: 100 nm.

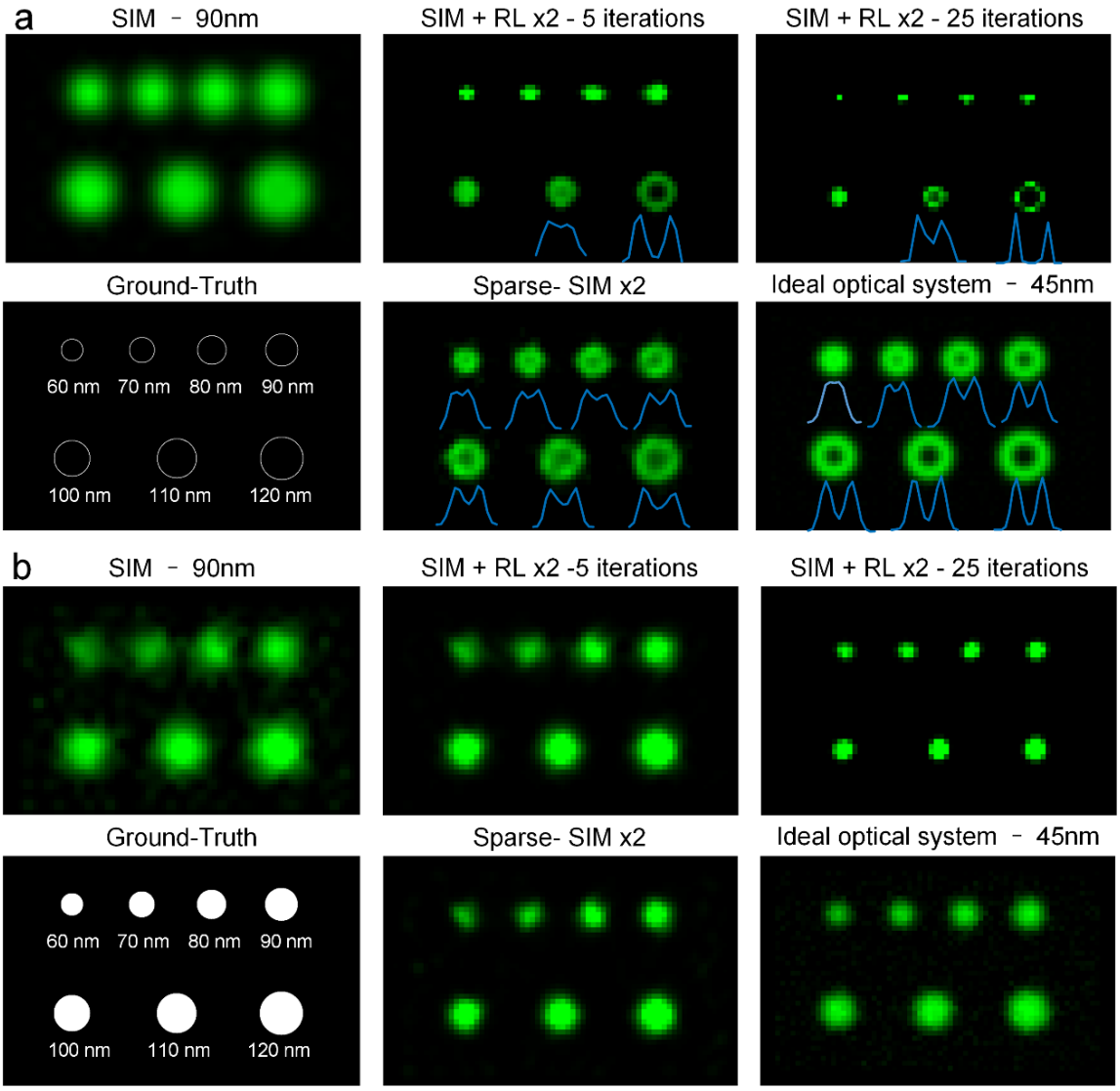

Extended Data Fig. 4 | Comparisons of reconstruction results of synthetic ring-shaped and punctated structures by the sparse and RL deconvolutions. Ring-shaped (**a**) and punctated structures (**b**) with different diameters were convolved with PSF with FWHM of either 90 nm (top left corner) or 45 nm (bottom right corner). These images were subsequently subsampled 32 times (pixel sizes of 32 nm) and corrupted with Poisson noise and 2% Gaussian noise to simulate ground truth images observed under microscopes with different spatial resolutions. For images reconstruction, we first Fourier interpolated images, and then deconvolved with conventional RL (5 and 25 iterations) or the sparse deconvolution algorithm, respectively (same parameters for punctated and ring-shaped structures).

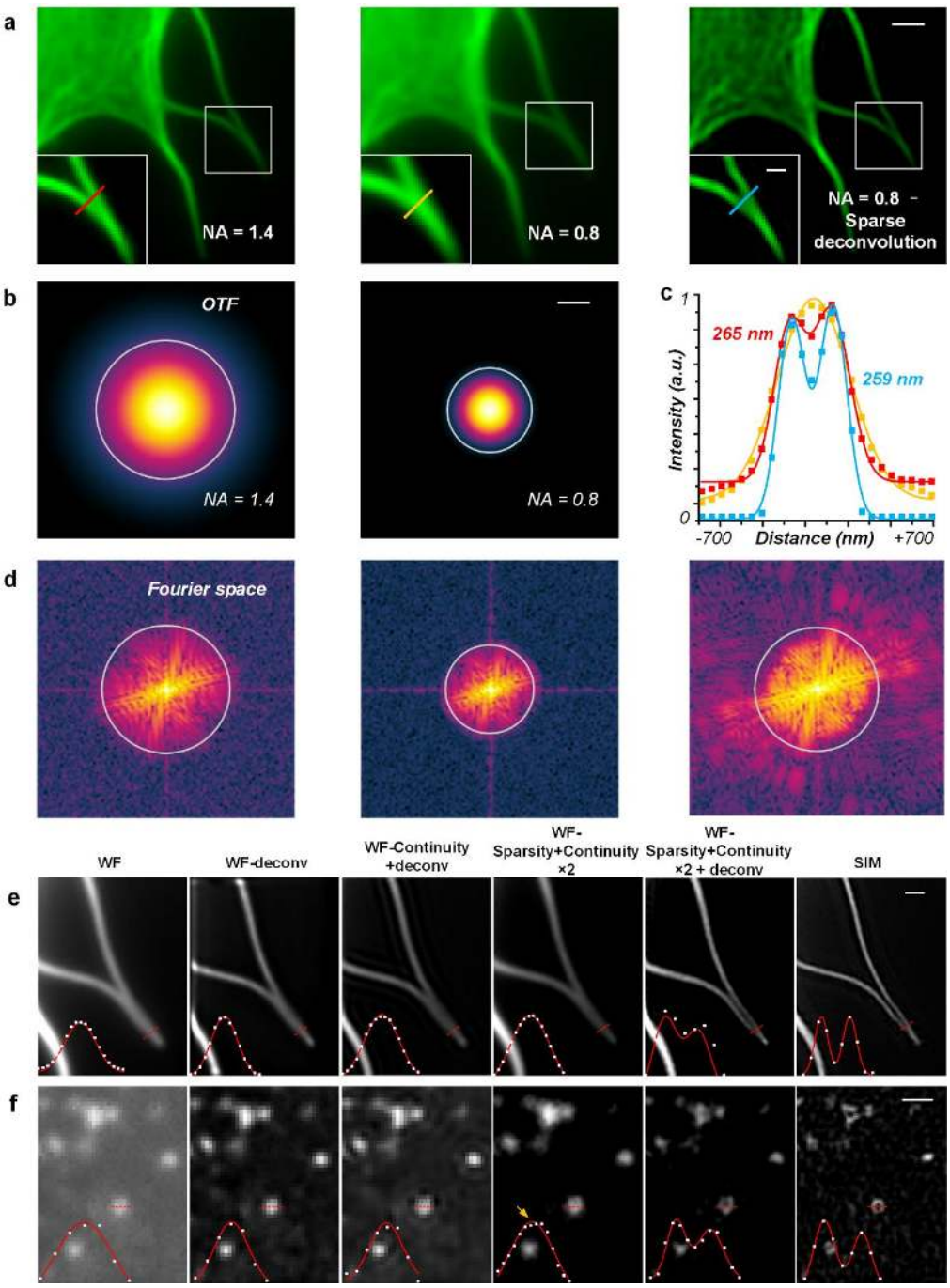

Extended Data Fig. 5 | Bona fide extension of spatial resolution by the sparse deconvolution when processing real biological structures. (**a**) From left to right are the high NA (1.4) image, the simulated low NA (0.8) image, and the low NA (0.8) image after sparse deconvolution (same data as in **Fig. 4a**). Here, the low NA image was generated using the formula iFFT[FFT($IMG_{1.4}$) × ($OTF0.8/OTF_{1.4}$)]. In the formula, the (i) FFT denotes the (inverse) fast Fourier transforms, and $IMG_{1.4}$ represents the high NA image. (**b**) The optical transform functions of NA = 1.4 ($OTF_{1.4}$) and NA = 0.8 ($OTF_{0.8}$). (**c**) The corresponding Gaussian-fitted cross-sections of the insets in (**a**). The two peaks with a distance of 259 nm are resolved under the low NA after sparse deconvolution, which is similar to 265 nm in the original high NA image. This indicates that sparse deconvolution achieves high NA resolution with better contrast. (**d**) The corresponding Fourier space images are presented from left to right. (**e**, **f**) We used live COS-7 cells overexpressing LifeAct-EGFP (**e**, *c.f.*, **Fig. 4a**, see also **Supplementary Video 15**) or Clathrin-EGFP (**f**) and imaged them with 2D-SIM, TIRF-SIM respectively. From the raw dataset, we used regular deconvolution, continuity reconstruction followed by deconvolution, upsampling plus sparsity, and continuity reconstruction, or upsampling plus sparsity and continuity reconstruction followed by deconvolution. Scale bars: (**a**, **b**, **d-f**) 500 nm; (**a**, inset) 200 nm.

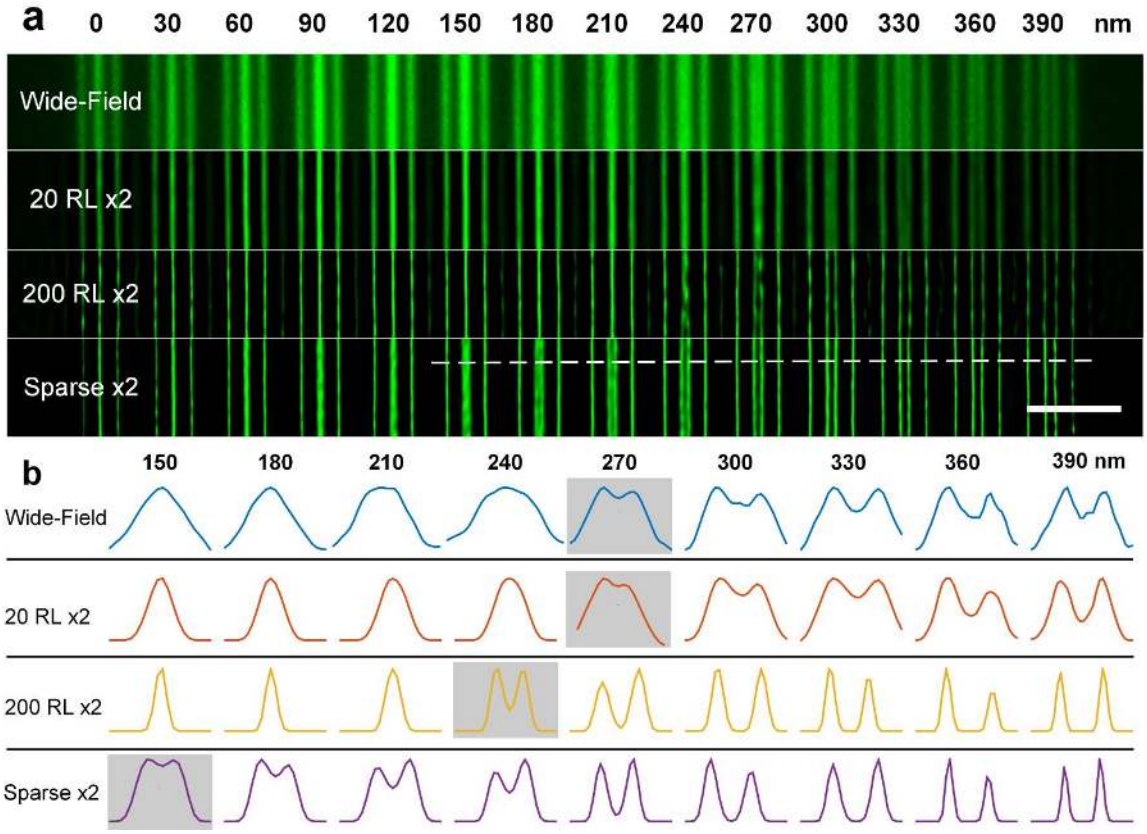

Extended Data Fig. 6 | Benchmarking of the resolution improvement of wide-field microscopy by the sparse deconvolution using pre-made pairs of horizontal lines of decreasing space. (**a**) The standard horizontal gradually spaced lines observed either by the wide-field microscope (NA 1.4), or Fourier interpolated, followed by the RL deconvolution with 20 (20 RL ×2) or 200 iterations (200 RL ×2), or Fourier interpolated followed by the sparse deconvolution (Sparse ×2). (**b**) The wide-field, 20 RL ×2, 200 RL ×2, Sparse ×2 configurations were able to distinguish pair lines up to 270 nm, 300 nm, 240 nm, and 150 nm, respectively. Scale Bar: 3 μm.

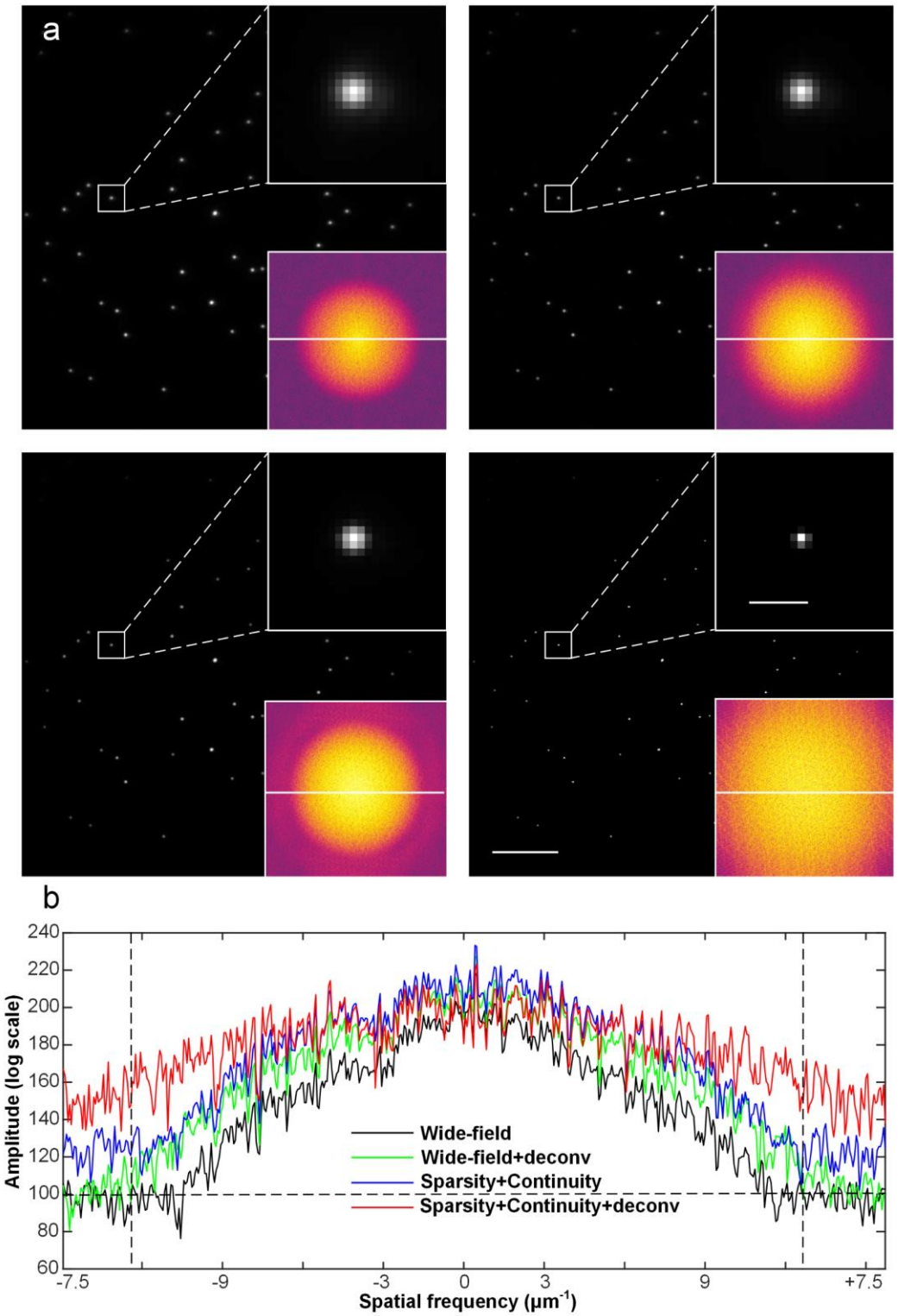

Extended Data Fig. 7 | OTFs obtained by the Fourier transform of fluorescent beads visualized under different conditions. (a) Images of fluorescent beads (48 nm in diameter) under wide-field imaging: (left upper), wide-field followed by deconvolution (right upper), wide-field plus sparsity and continuity reconstruction (left bottom), and wide-field plus sparsity and continuity reconstruction followed by deconvolution (right bottom). Upper insets: A single bead observed under different conditions; Lower insets: the corresponding Fourier transform of the image on the left. (**b**) The amplitudes along the white lines in the frequency domain from the low insets in **a**, while the two vertical dashed lines indicate the wide-field microscope's spatial frequency limits. Scale bar: 5 μm; inset: 500 nm.

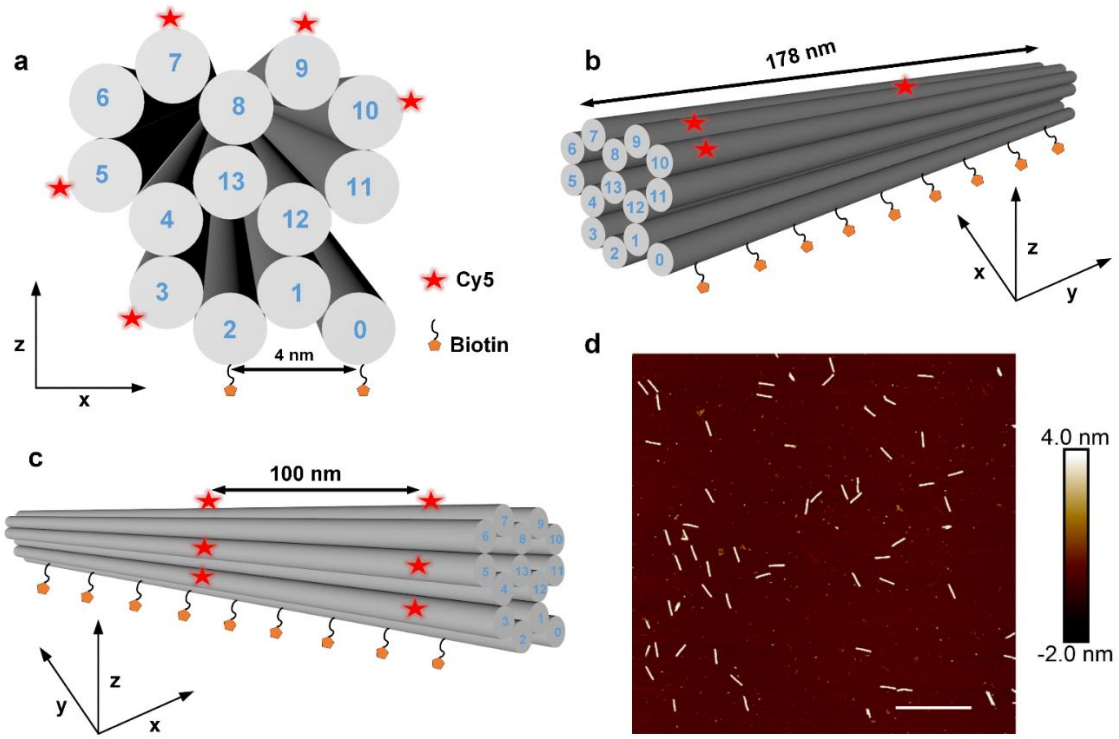

Extended Data Fig. 8 | Design and representative images of the 100 nm tubular DNA origami nanostructure. (**a**) Front-view schematic diagram of 14-HB DNA origami, including incorporating the Cy5 and biotin at 3' ends of the selected staple oligonucleotides. We attached biotin to two helix bundles (HB0 and HB2), and Cy5 to five (HB3, HB5, HB7, HB9, HB10), or four helix bundles (HB3, HB5, HB7, HB9). (**b**) Right-side view of the schematic diagram. (**c**) Left-side view of the schematic diagram. (**d**) DNA origami over a large field of view under the atomic force microscope. Scale bar: 1 μm.

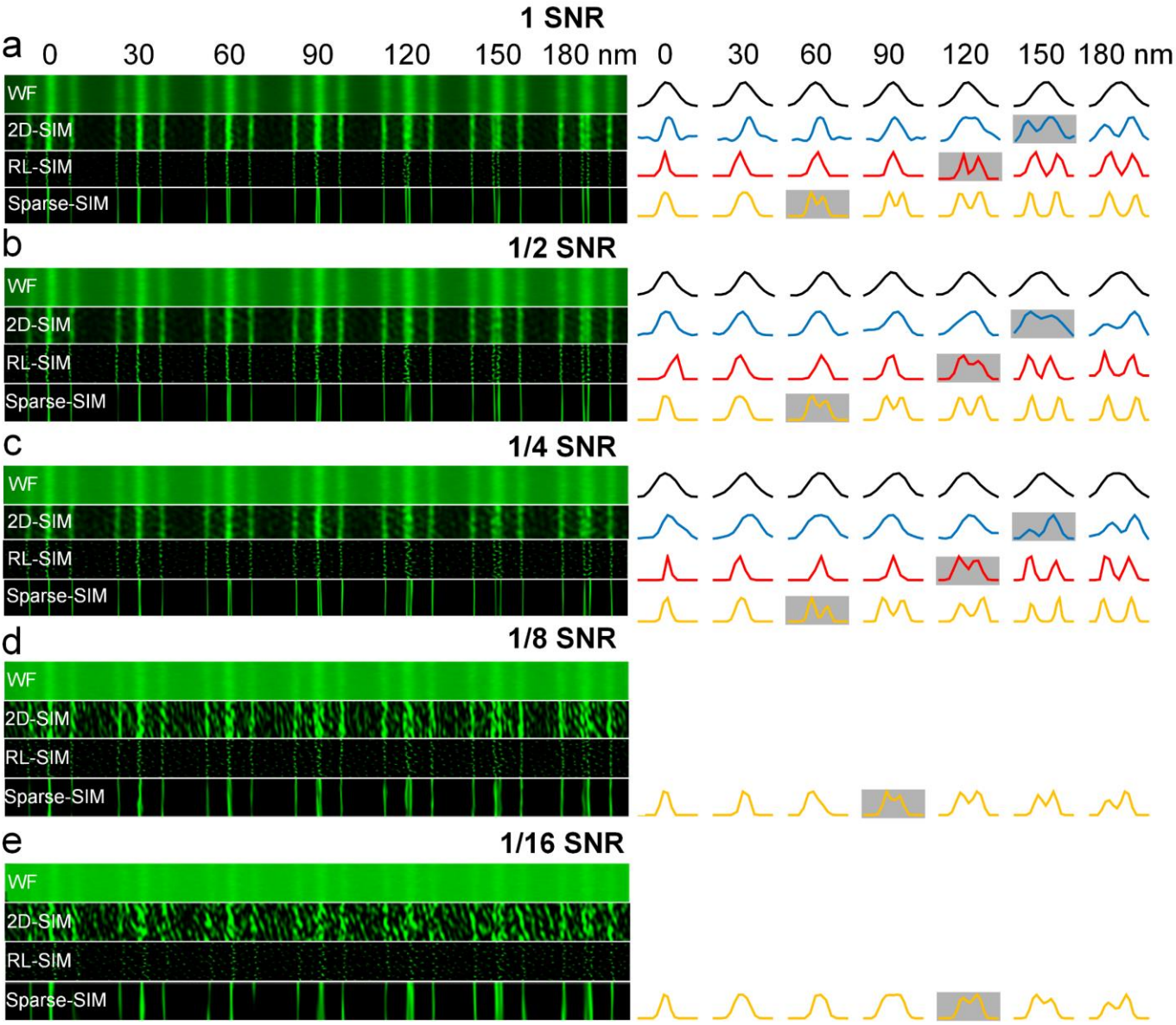

Extended Data Fig. 9 | Sparse deconvolution for Argo-SIM slide under different SNR conditions. (**a-e**) The results with different SNRs. We set the imaging condition of results in (**a**) as the full SNR ('1 SNR'), and the SNRs decreased from 1/2 to 1/16 for the results in (**b-e**). Left panel, from top to bottom: the averaged wide-field (WF) image (NA 1.4), the image reconstructed by Wiener-SIM (2D-SIM), the image reconstructed by Wiener-SIM and followed by RL deconvolution with 50 iterations ('RL-SIM'), and our Sparse-SIM model result. Right panel, from top to bottom: the corresponding fluorescence profiles along lines crossing the middle of the left panel. When the SNR was in the range of 1~1/4, the 2D-SIM, RL-SIM, and Sparse-SIM distinguished pair lines up to 150 nm, 120 nm, and 60 nm, respectively. When the SNR was in the range of 1/8~1/16, 2D-SIM and RL-SIM failed to reconstruct the paired parallel lines, and snowflake-like artifacts emerged. However, under similar conditions, Sparse-SIM still resolved the pair parallel lines up to 90 nm and 120 nm, respectively.

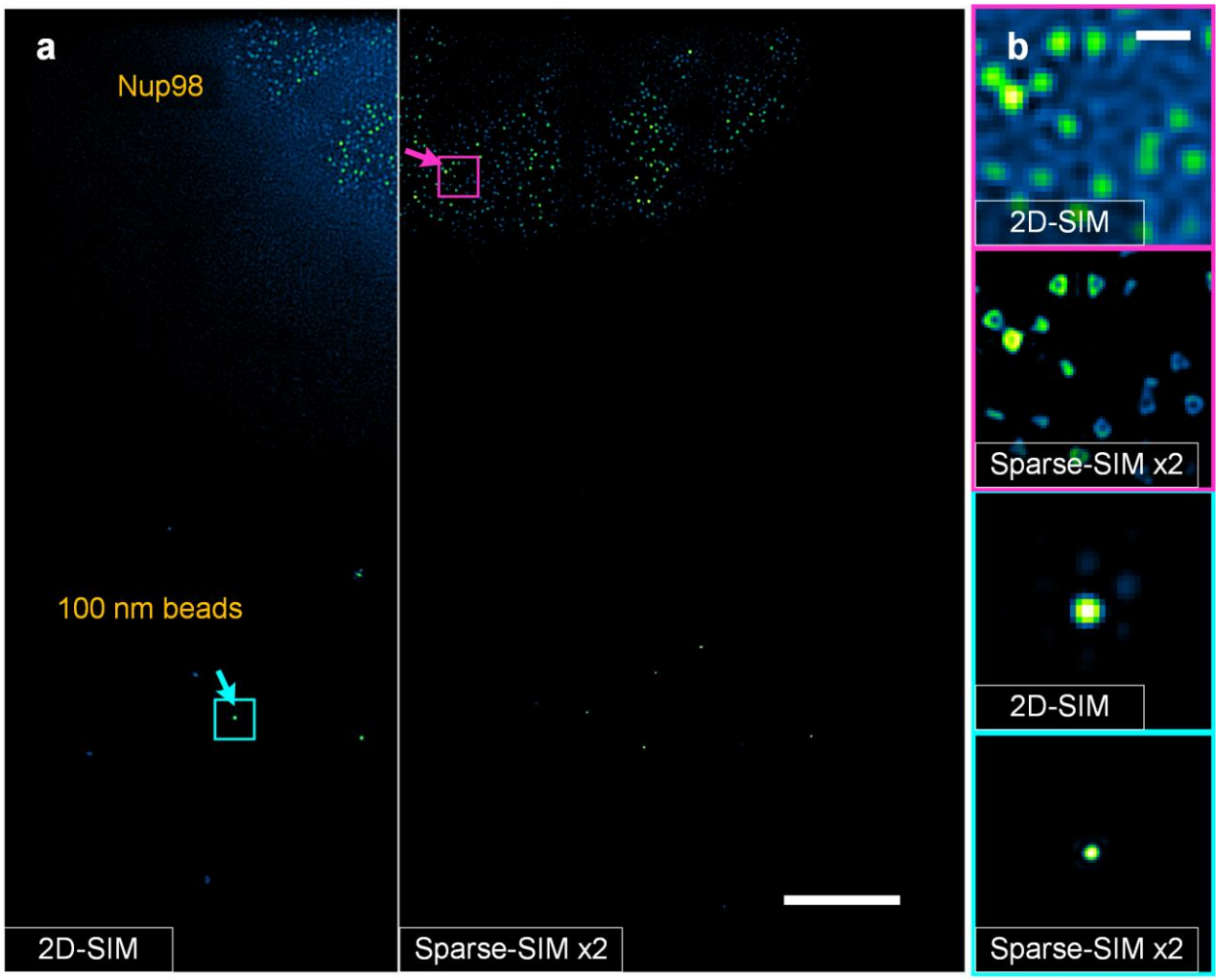

Extended Data Fig. 10 | Nup98 pores and 100 nm beads in the same FOV under the 2D-SIM and the Sparse-SIM × 2. (**a**) Snapshots under the 2D-SIM and the Sparse-SIM ×2 configurations were shown on the left and right side. (**b**) Magnified view of the regions in (**a**) under 2D-SIM and Sparse-SIM × 2. The magenta and cyan boxes represent the view of Nup98 and 100 nm bead, respectively. Scale bars: (**a**) 3 μm; (**b**) 300 nm.

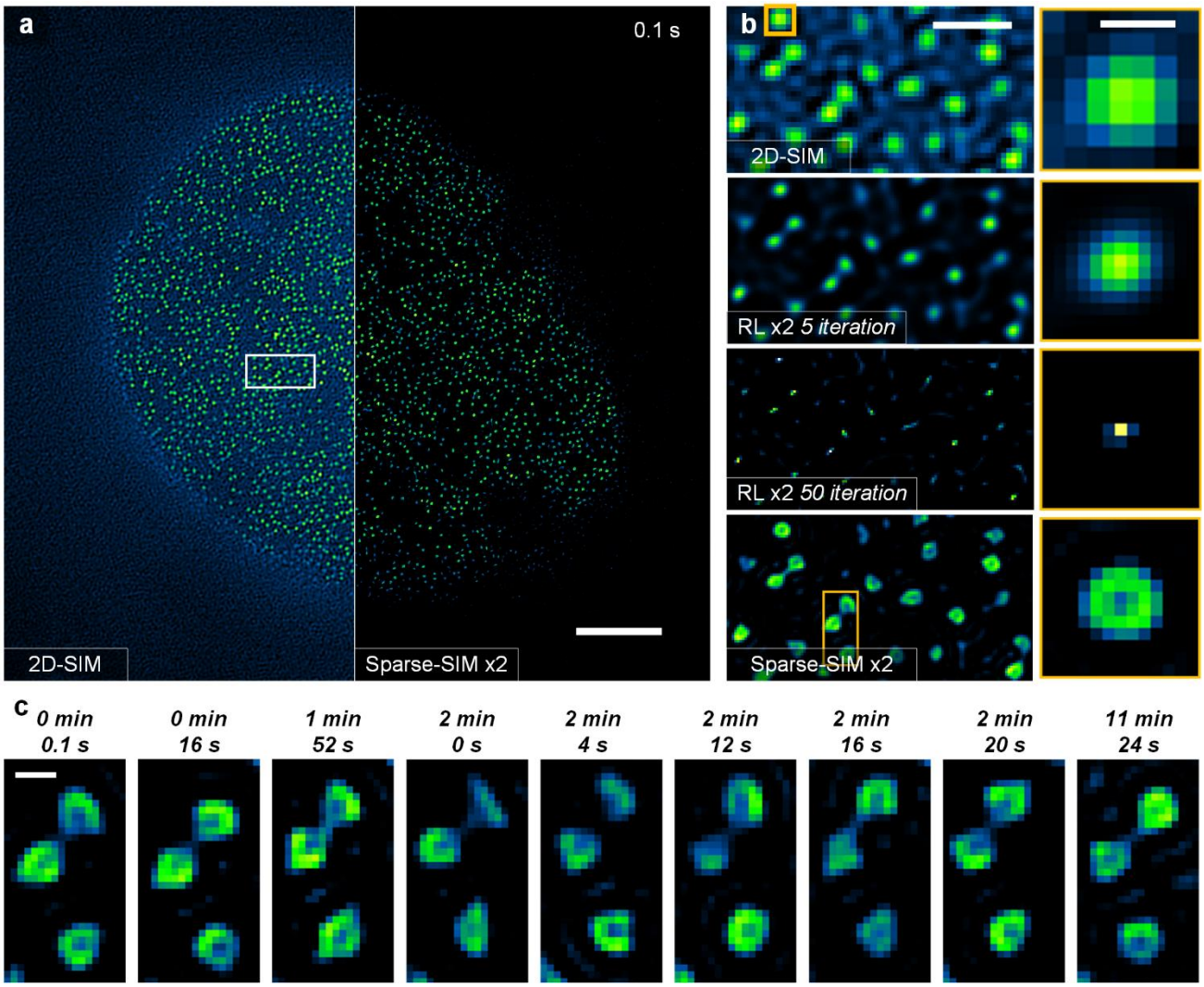

926

927 **Extended Data Fig. 11 | Sparse-SIM detected long-term dynamics of ring-shaped nuclear pores labeled**
928 **by Nup98-GFP in a live COS-7 cell (the holistic view of Fig. 2c).** (**a**) Snapshots were acquired in 0.1 sec
929 under the 2D-SIM, and the Sparse-SIM ×2 configurations were shown on the left and right sides. (**b**)
930 Magnified view of the region in (**a**) under different configurations were shown in the left, from which the
931 nuclear pore enclosed in the yellow box was further zoomed up and shown in the right panels. (**c**) The yellow
932 box in (**b**) is enlarged and shown at nine time points. Scale bars: (**a**) 3 μm; (**b**) 500 nm; 100 nm; (**c**) 100 nm.

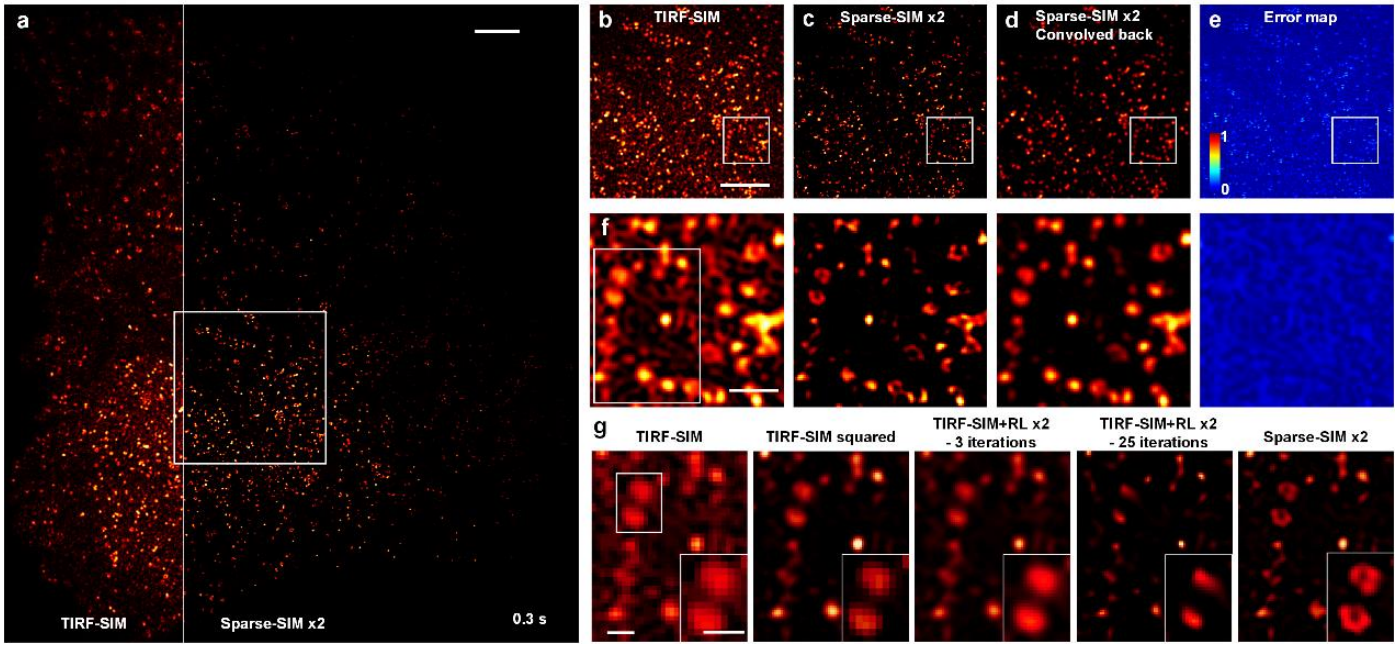

Extended Data Fig. 12 | Analysis of possible artifacts in the caveolae images reconstructed with the sparse deconvolution, which was further compared with other deconvolution methods. (**a**) A representative COS-7 cell labeled with caveolin-EGFP under TIRF-SIM and Sparse-SIM ×2 (whole FOV from **Fig. 4j**). (**b-e**) The region enclosed by the white box in (**a**) was magnified and shown under the non-iterative method (TIRF-SIM), sparse reconstruction (Sparse-SIM ×2), or sparse reconstruction followed by convolving back with the resolution scaled function (RSF). The RSF is estimated between TIRF-SIM and Sparse-SIM ×2, and the FWHM of this estimated RSF is 78 nm. (**e**) The resolution scaled error (RSE) map of Sparse-SIM ×2 against the raw TIRF-SIM image. Before the RSE map estimation, the intensity of TIRF-SIM and Sparse-SIM images are normalized to the range of 0~1, and the corresponding residual image (RSE map) is color-coded within the range of 0~1. (**f**) Magnified views in (**b-e**). (**g**) The region enclosed by the white rectangle in (**f**) was magnified and reconstructed with a non-iterative method (TIRF-SIM), followed by image squares (TIRF-SIM square), or Fourier interpolated followed by RL-deconvolution (TIRF-SIM + RL ×2) for 3 or 25 iterations, or Fourier interpolated followed by the sparse deconvolution (Sparse-SIM ×2). Scale bars: (**a-e**) 2 μm; (**f**) 1 μm; (**g**) 100 nm.

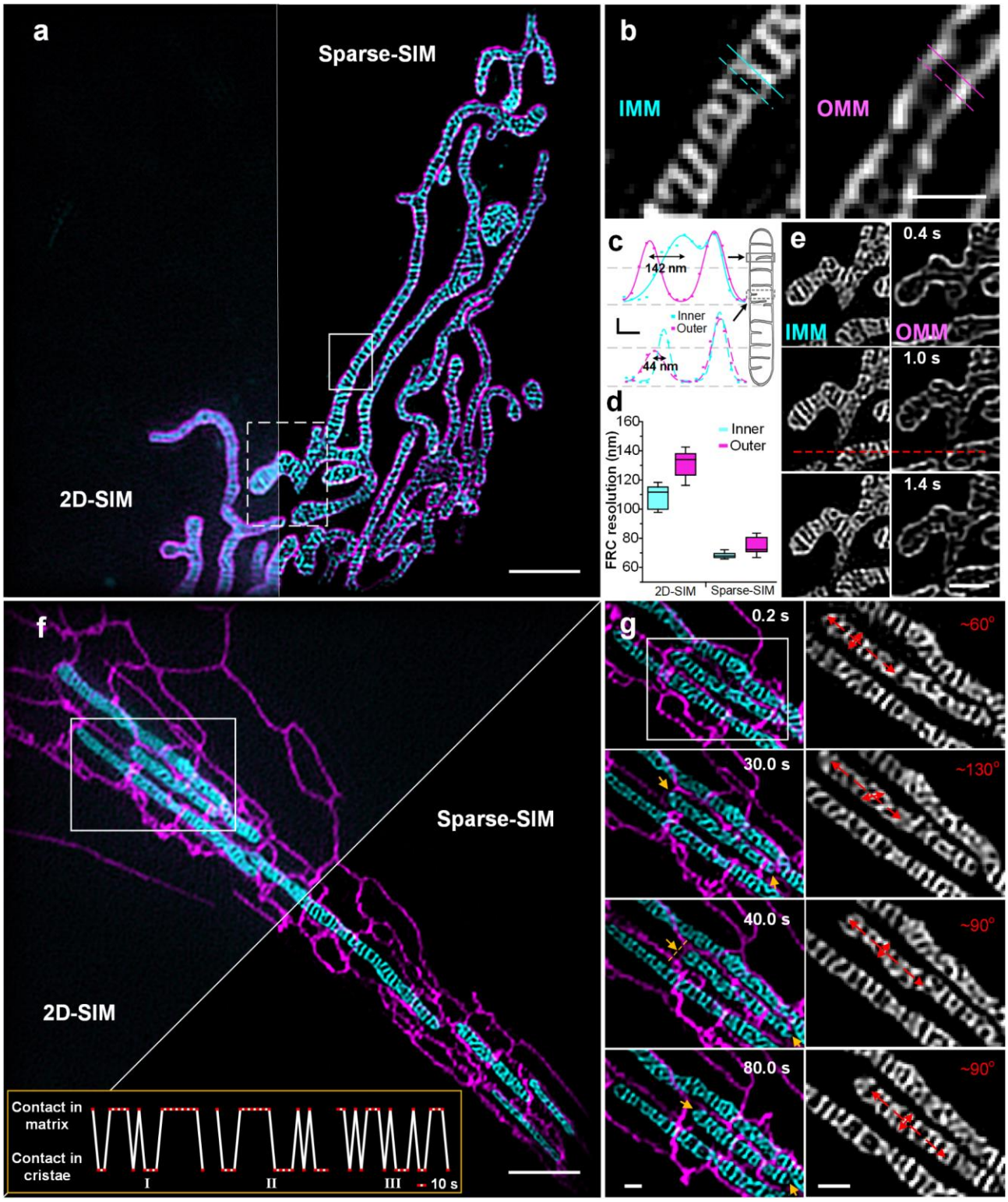

Extended Data Fig. 13 | Intricate dynamics within the mitochondria and between ER-mitochondria visualized by dual-color Sparse-SIM. (**a**) The OMM and IMM in a COS-7 cell. (**b**) Magnified views from the white box in (**a**). (**c**) Intensity profiles of Tom20-mScarlet (magenta) and MitoTracker Green (cyan) along the continuous and dashed lines in (**b**), with mitochondrial configurations shown in the right. (**d**) Average FRC resolutions in (**a**). (**e**) The white dashed box in (**a**) is enlarged and shown at three time points. (**f**) A representative example of both the IMM (cyan) and ER (magenta). (**g**) Magnified views from the white box in (**f**). Centerline, medians; limits, 75% and 25%; whiskers, maximum and minimum; error bars, s.e.m; scale bars: (**a**, **f**) 1 μm; **(c)** axial: 0.2 arbitrary units (a.u.); lateral: 100 nm; (**b**, **e** and **g**) 500 nm.

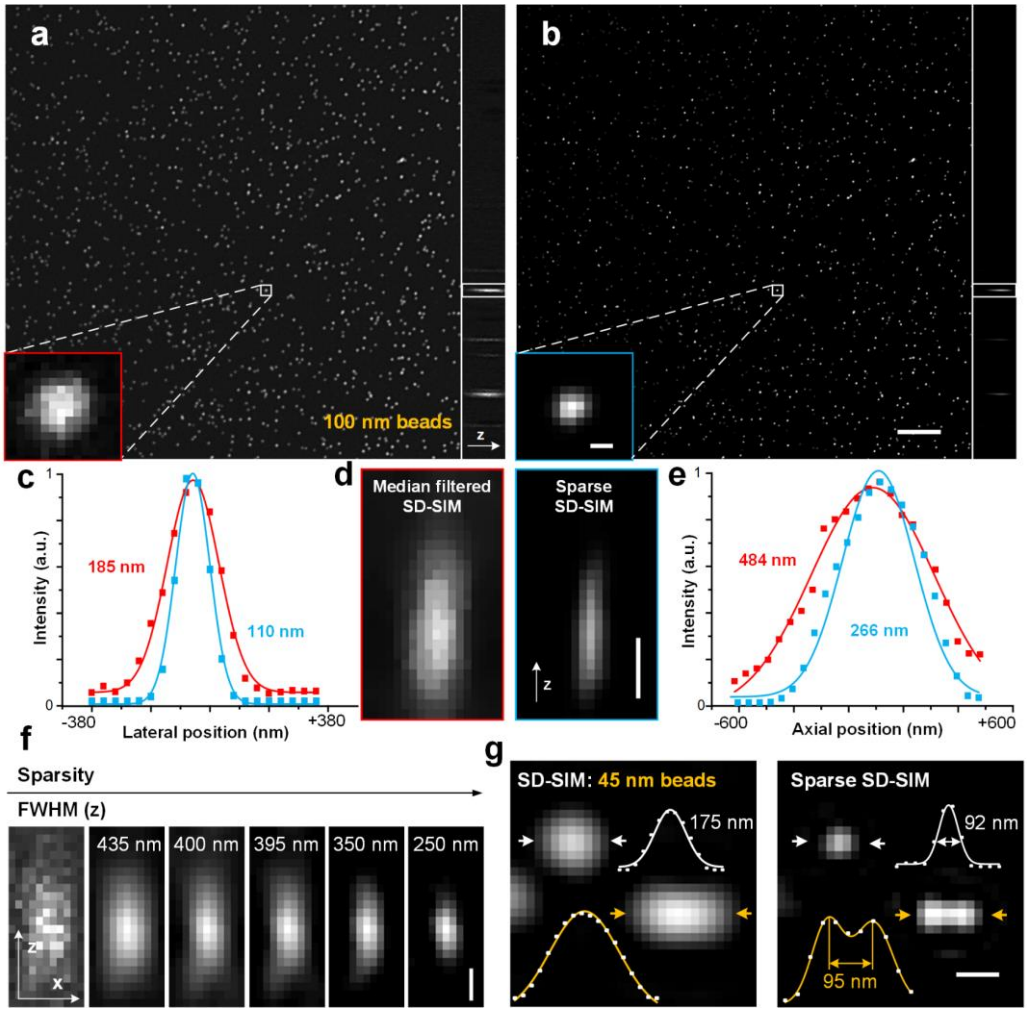

957

958 **Extended Data Fig. 14 | Three-dimensional image stack of fluorescent beads under SD-SIM and Sparse**
959 **SD-SIM.** (**a-b**) A maximum intensity projection (MIP) view (left) and a horizontal section (right) of
960 fluorescent beads (100 nm in diameter) recorded by SD-SIM (**a**) and after the sparse deconvolution (**b**),
961 respectively. Insets in the left-lower corner show a magnified view of the same fluorescent bead under different
962 reconstruction methods. (**c**) The corresponding Gaussian fitted profiles in (**a,** left-lower corner)**,** which indicate
963 that the lateral FWHM of SD-SIM (red) and Sparse SD-SIM (blue) are 185 nm (calibrated resolution ~165
964 nm) and 110 nm (calibrated resolution ~90 nm), respectively (**Supplementary Note 9.2**). (**d**) Magnified
965 horizontal sections from the white boxes in (**a–b**) are shown in the left and right panels, while the SD-SIM
966 image is processed with a median filter to avoid a non-converged fitted result. (**e**) We used Gaussian functions
967 to fit the intensity profiles along the axial direction of the fluorescent bead in (**d**), yielding axial resolutions of
968 484 nm and 266 nm for SD-SIM and Sparse SD-SIM, respectively. (**f**) The gradually improved axial resolution
969 (FWHM) of a 100 nm bead while increasing the weight of sparsity. (**g**) Measuring the FWHM with fluorescent
970 beads with a diameter of 45 nm. The fitted FWHMs (cross-sections between white arrows displayed with
971 white profiles in the right) of SD-SIM and Sparse SD-SIM are 175 nm and 92 nm, respectively. As shown
972 with yellow profiles (cross-sections between yellow arrows), the Sparse SD-SIM resolved adjacent two beads
973 with a distance of 95 nm. Scale bars: (**b**) 4 μm, (**b**, inset) 100 nm and (**d**, **f**, **g**) 200 nm.

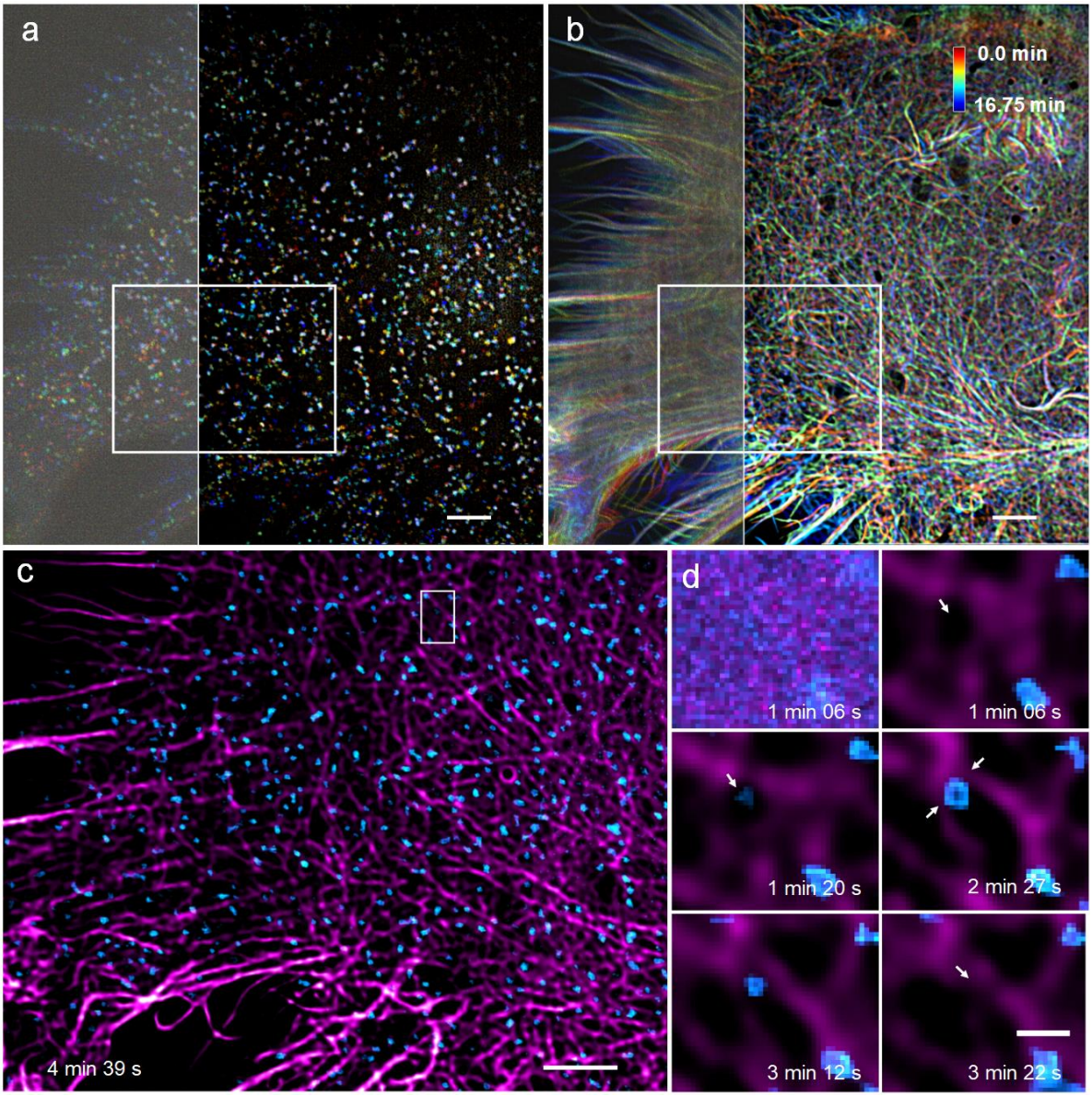

Extended Data Fig. 15 | Two-color live-cell imaging of clathrin and actin by Sparse SD-SIM (Supplementary Video 16). (**a–b**) Color temporal projections of CCPs (**a**) and the actin filament network (**b**) recorded by SD-SIM (left) and Sparse SD-SIM (right) for 16.75 minutes at 5 s intervals. (**c**) CCPs (cyan) and the cortical actin cytoskeleton (magenta) in a COS-7 cell captured by Sparse SD-SIM. (**d**) Montages of the boxed region in (**c**) at five-time points are shown at a magnified scale; the first image observed under SD-SIM appears at the top left corner for comparison. It can be observed that a CCP docks stably at the junction of two actin filaments and then disappears from the focal plane as these neighboring filaments merge. Scale bars: (**a-c**) 4 μm; (**d**) 500 nm.

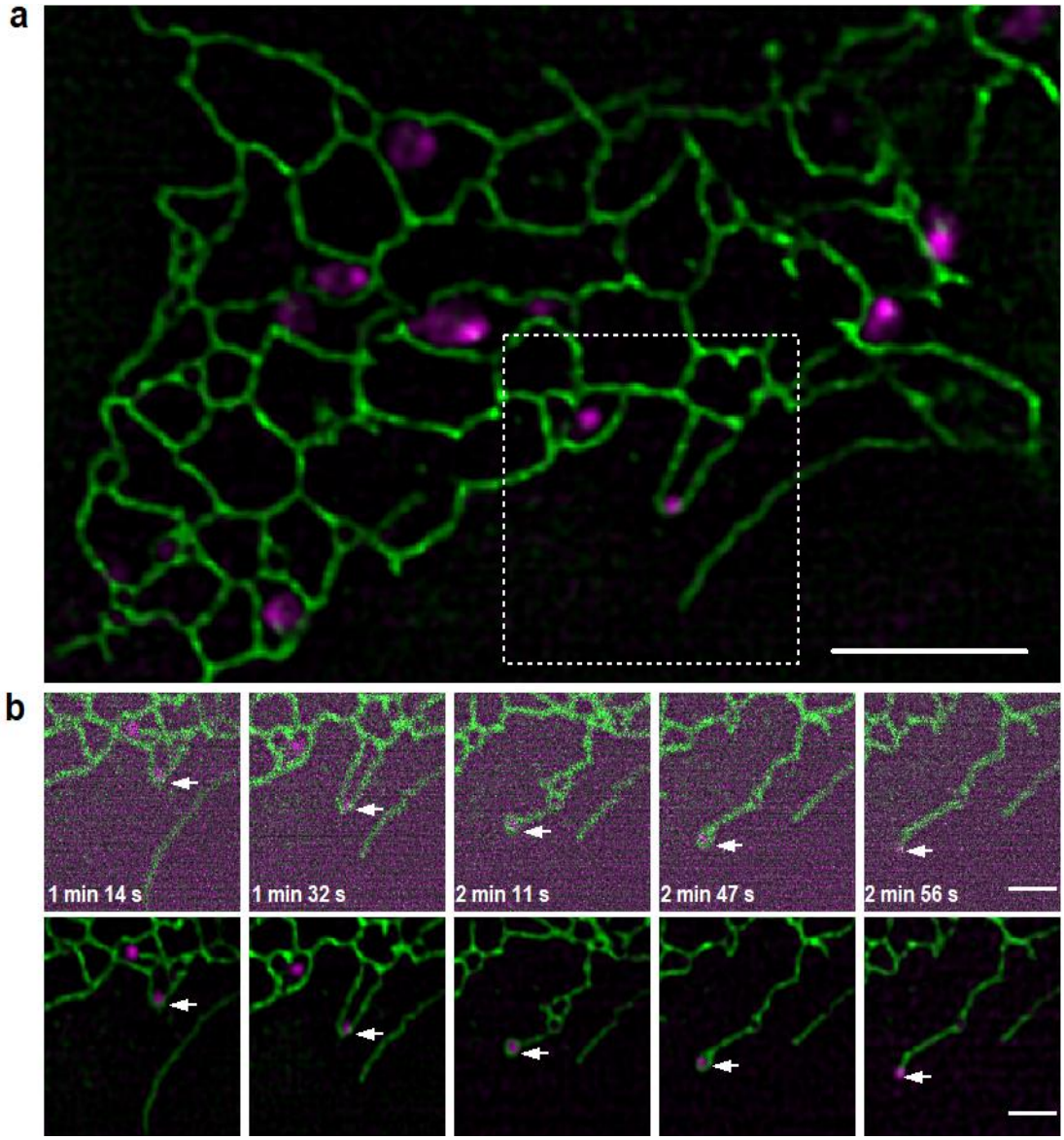

Extended Data Fig. 16 | ER-lysosome contacts revealed by the sparse SD-SIM (Supplementary Video 17). (**a**) Contacts between ER tubules (labeled by Sec61-EGFP, green) and lysosomes (labeled by Lysotracker DeepRed, magenta) visualized by Sparse SD-SIM in live COS-7 cells. (**b**) Time-lapse images of typical lysosome-ER contact dynamics magnified from the dashed-boxed region in (**a**) by SD-SIM (top) and Sparse SD-SIM (bottom). The ER tubules moved along with the lysosome, followed by the contraction of the tubular structure to a polygon surrounding the lysosome (indicated by white arrows) and the final disappearance of the polygon due to the retraction of the ER tubules. Scale bars: (**a**) 3 μm; (**b**) 2 μm.

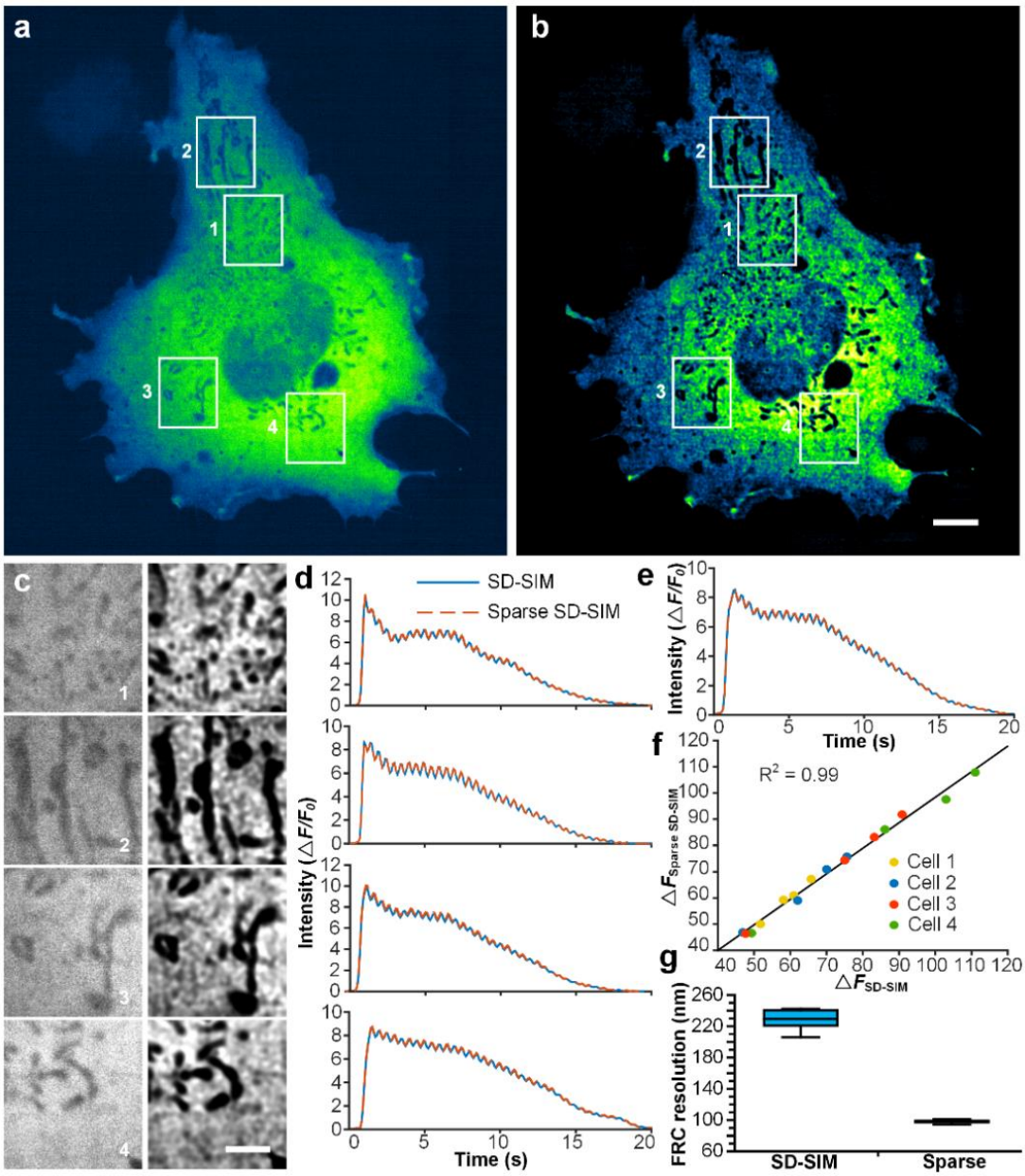

Extended Data Fig. 17 | Highly-correlated Ca^{2+} transients after the sparse deconvolution compared to the original data obtained by the SD-SIM. (**a**, **b**) The representative COS-7 cell was transfected with GCaMP6s, stimulated with ATP (10 μM). One snapshot under the SD-SIM (**a**) and after the sparse deconvolution (**b**) were shown. (**c**) Magnified views of regions enclosed by white boxes 1-4 in (**a**, and **b**). (**d**) ATP stimulated calcium traces from corresponding macrodomains in (**c**). (**e**) Representative ATP stimulated whole-cell calcium traces. (**f**) ATP stimulated increases in fluorescence intensities of GCaMP6s from different macrodomains (4 cell × 4 regions) under the SD-SIM (x-axis) exhibited a linear relationship with those obtained under the Sparse SD-SIM microscope (y-axis). (**g**) Average minimal resolutions by the FRC method. Scale bars: (**a**) 5 μm; (**c**) 2 μm.

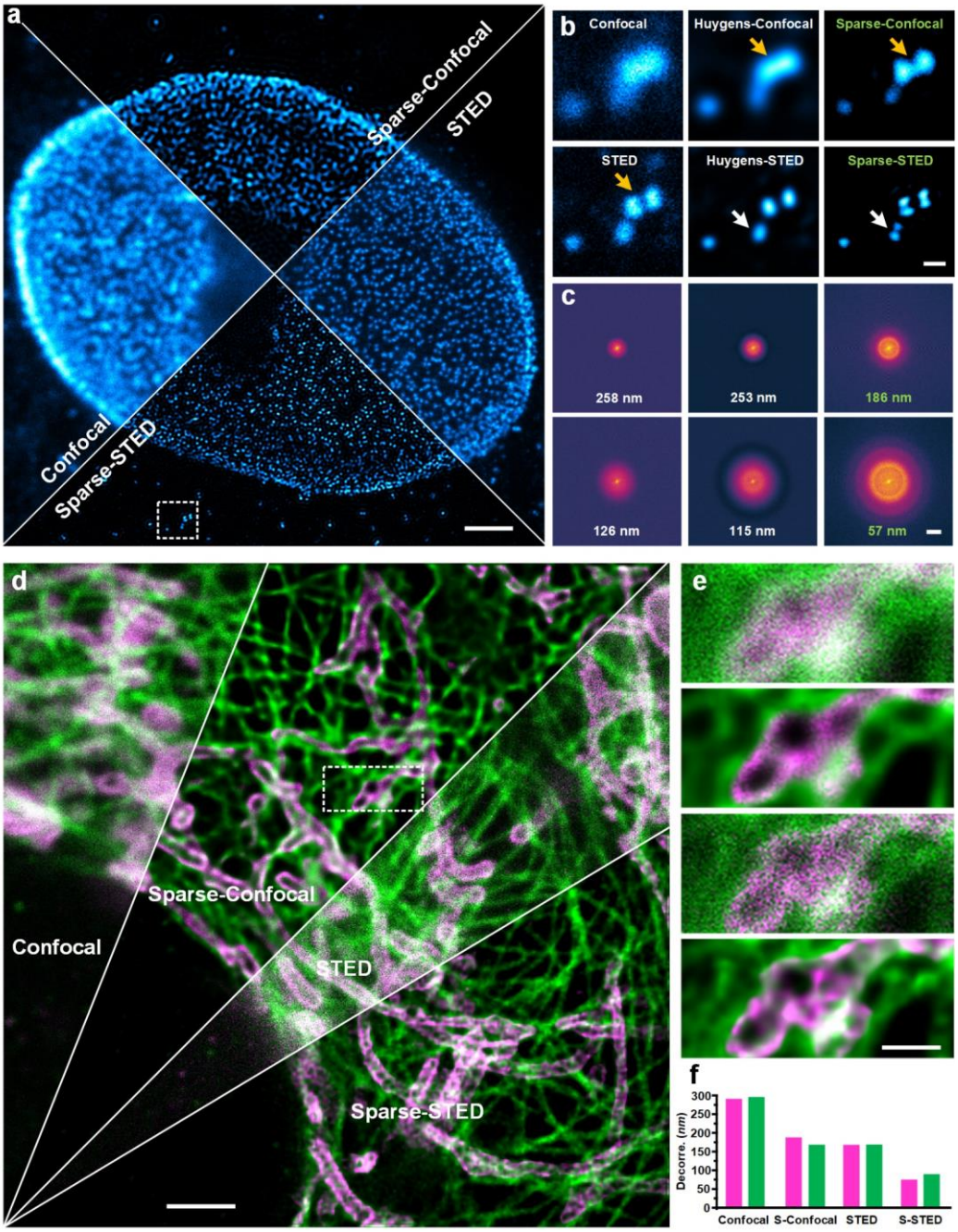

Extended Data Fig. 18 | *Bona fide* spatial resolution improvement of confocal and STED microscopes by the sparse deconvolution. (**a**) Nuclear pores in HeLa cells were labeled with an anti-Mab414 primary antibody and the Alexa594 secondary antibody, and observed under the confocal, Sparse-confocal, STED, and Sparse-STED configurations. (**b**) Magnified views from the region enclosed in the white dashed box in (**a**) under different microscopes. Huygens- represents that the images were deconvoluted by Huygens Professional (Scientific Volume Imaging, The Netherlands). (**c**) The Fourier transforms of images obtained by the corresponding microscopes. Labeled with the corresponding decorrelation resolution. (**d**) A representative HeLa cell in which microtubules (green) and mitochondria (magenta) were labeled with anti-tubulin and anti-Tom20 primary antibodies. It was imaged under the Confocal, Sparse-Confocal, STED, and Sparse-STED configurations. (**e**) Magnified views from the region enclosed by the white dashed box in (**d**). (**f**) Resolutions are measured by the decorrelation method. S-Confocal: Sparse-Confocal; S-STED: Sparse-STED; Scale bars: (**a**, **c**, **d**) 2 μm; (**b**) 200 nm; (**e**) 500 nm.

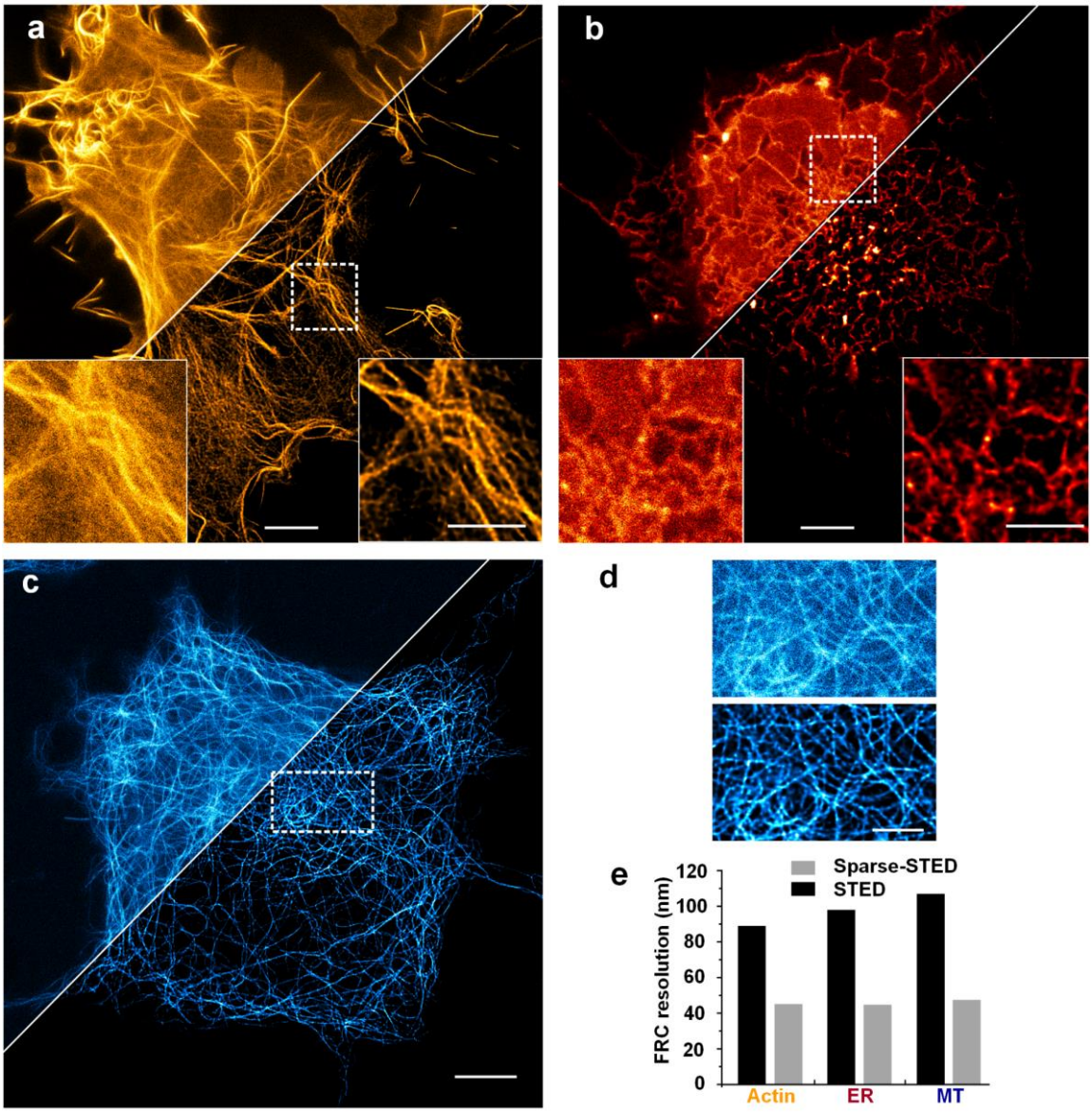

Extended Data Fig. 19 | Extending the spatial resolution of STED microscopy with sparse deconvolution. (**a, b**) A live COS-7 cell expressing either Lifeact-GFP (**a**) or Sec61β-GFP (**b**) visualized under the STED microscope (top), or after the Sparse deconvolution (bottom). Insets show magnified views of the same region seen under the STED (lower left inset) and after the Sparse deconvolution (lower right inset). (**c-d**) A snapshot of SiR-Tubulin-labeled microtubules seen under the STED (top) and Sparse-STED (bottom, **c**). The region enclosed by the white dashed box in (**c**) was magnified and shown in **d** (STED, top; Sparse-STED, bottom). (**e**) FRC minimum resolutions of actin, ER, and microtubules in (**a-c**) under STED and the Sparse-STED. ER: endoplasmic reticulum; MT: microtubule; Scale bars: (**a, b, c**) 5 μm; (**a** inset, **b** inset and **d**) 2 μm.

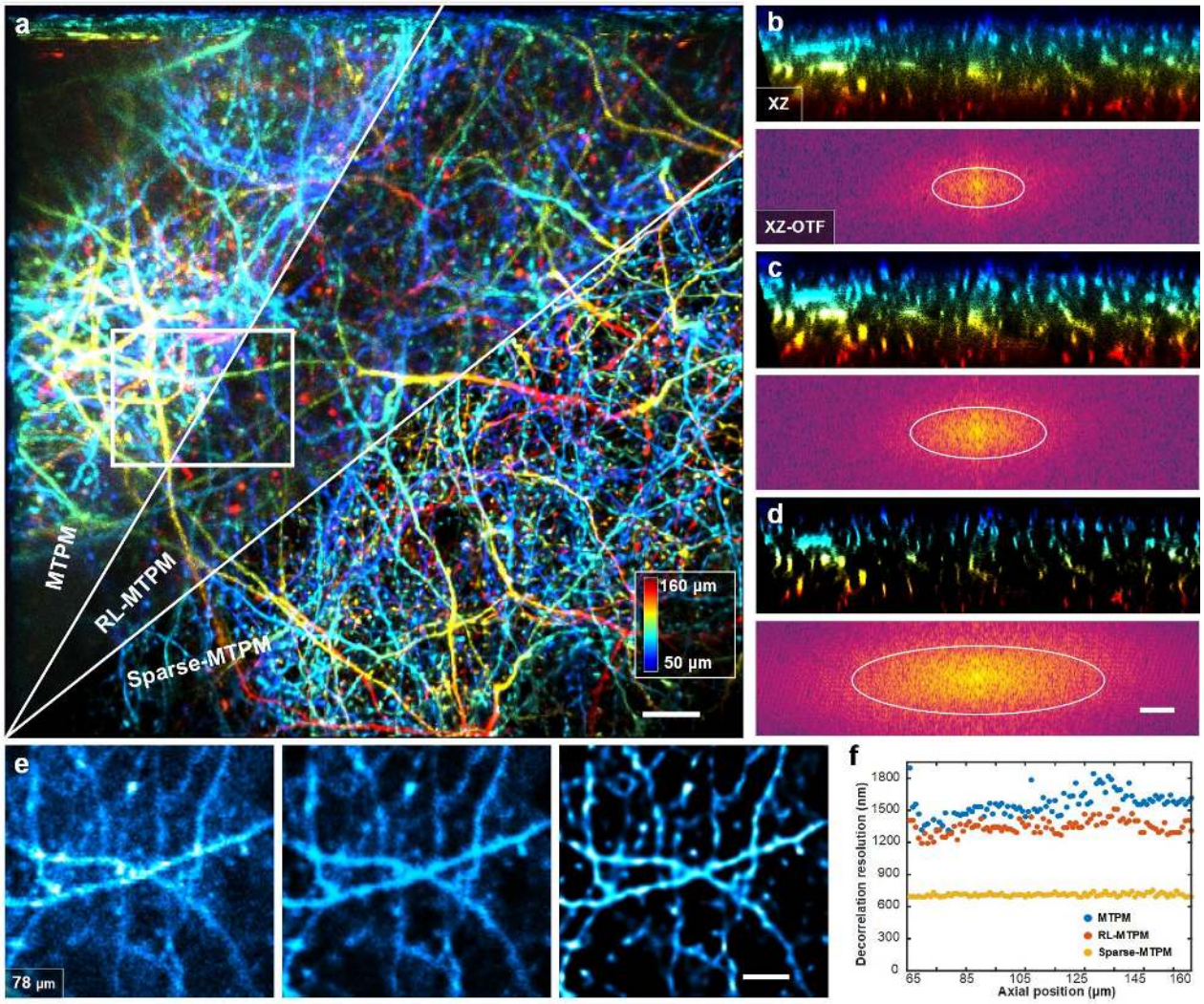

Extended Data Fig. 20 | Extending the spatial resolution of a miniaturized two-photon microscope (MTPM) with sparse deconvolution. (**a**) Three-dimensional distributions of neuronal dendrites and spines within a volume of 190 × 190 × 110 μm^3 from the brain of a Thy1-GFP transgenic mouse were observed under the MTPM, and after RL (RL-MTPM) or the sparse deconvolution (Sparse-MTPM). Different focal planes away from the surface were color-coded and projected to one image (see **Supplementary Video 18**). (**b-d**) The *xz* views and their Fourier transforms (**a**) under different configurations (**b**, MTPM; **c**, RL-MTPM; **d**, Sparse-MTPM). (**e**) Magnified views from the region enclosed by the white box in (**a**) under different configurations (from left to right: MTPM, RL-MTPM, Sparse-MTPM). (**f**) Resolutions of designated configurations as calculated by the decorrelation method at different axial positions. Scale bars: (**a**, **d**) 15 μm; (**e**) 3 μm.

Figures

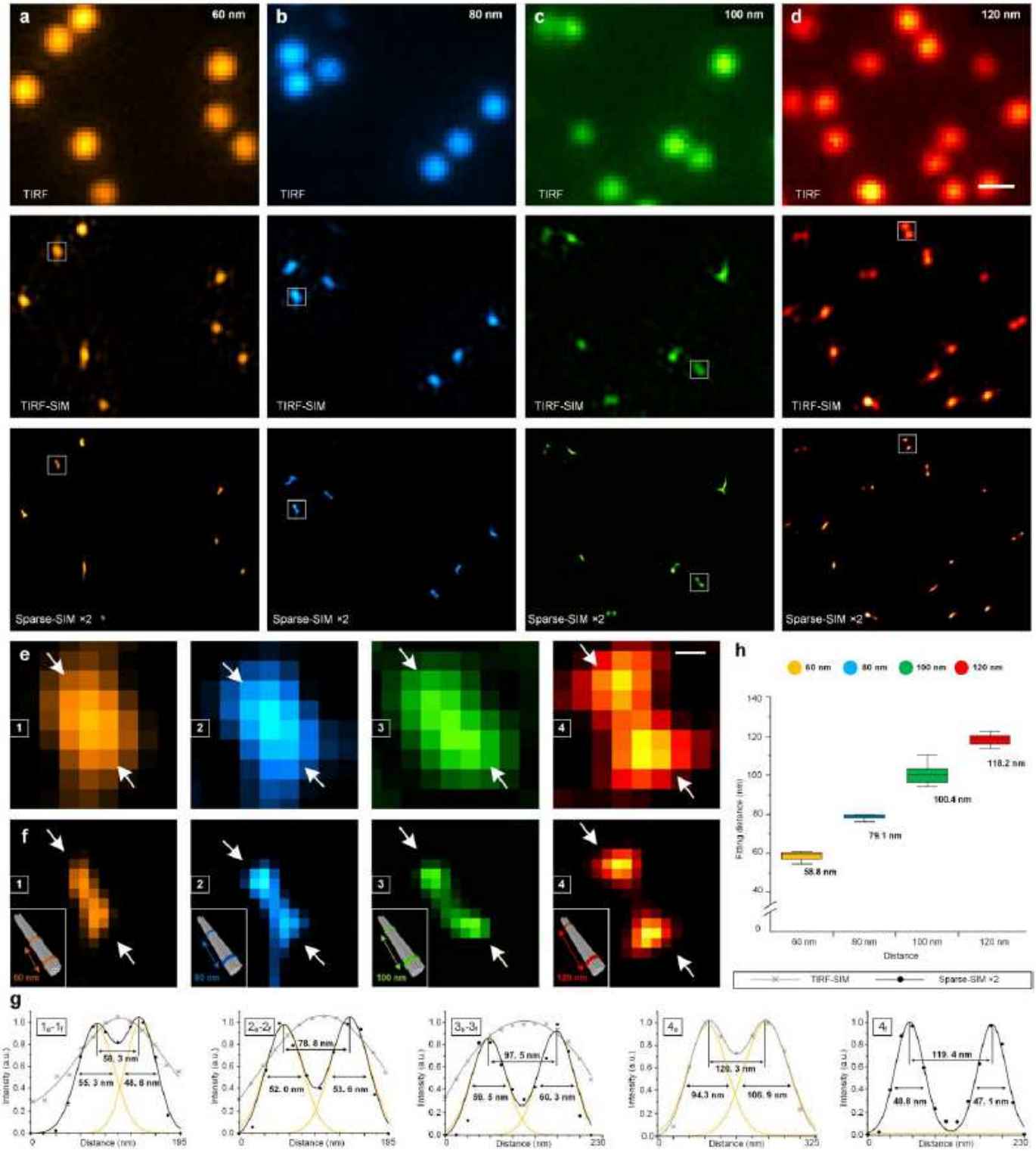

Figure 1

Evaluating Sparse-SIM with DNA origami samples. (a-d) DNA origami samples (Method) with 60 nm (a), 80 nm (b), 100 nm (c), and 120 nm (d) designed distances imaged by TIRF (top), TIRF-SIM (middle), and Sparse-SIM ×2 (bottom) configurations. (e, f) Enlarged regions enclosed by the white boxes in (a-d) under

TIRF-SIM (e) and Sparse-SIM ×2 (f) configurations. (g) Corresponding intensity profiles and multiple Gaussian fitting of the DNA origami structures indicated by the white arrows in (e), respectively. The numbers represent the FWHM and distance between peaks. (h) Average fitted distances of different DNA origami samples. Each measurement was repeated 12 times. Scale bars: (d) 500 nm; (e) 50 nm.

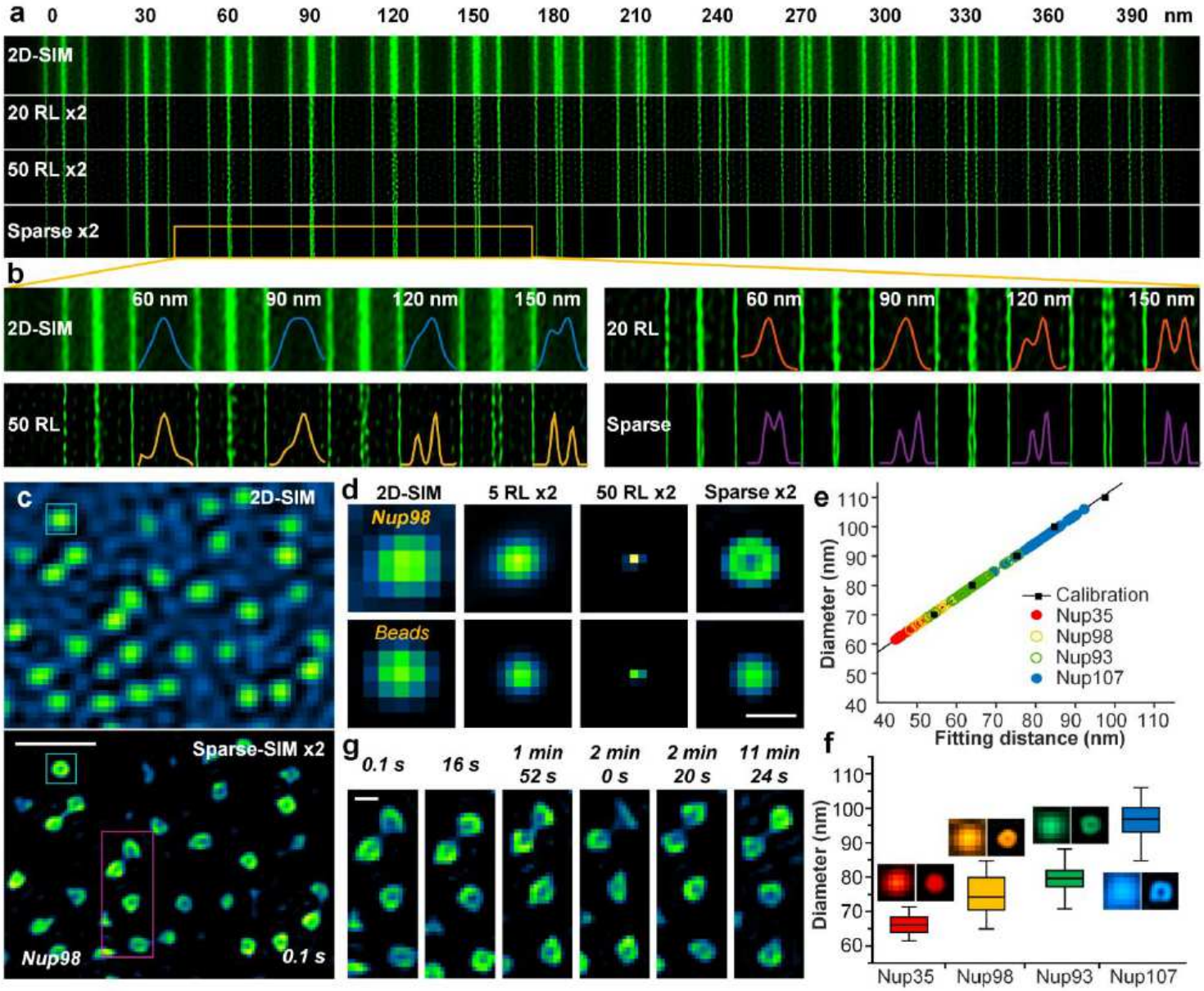

Figure 2

Sparse-SIM resolves known structures of ~60 nm in size. (a-b) Separation of two fluorescent lines with interline spacing down to 60 nm by the Sparse-SIM. Raw images were either reconstructed with Wiener algorithm (2D-SIM), or Fourier interpolated before reconstructed with Wiener algorithm followed by Fourier interpolated before reconstructed with the RL deconvolution for 20 (20 RL × 2), 50 (50 RL × 2) iterations, or the Sparse deconvolution pipeline (Sparse ×2) (a). The region enclosed by the yellow box was magnified and shown in (b). (c) A representative example of dynamic ring-shaped nuclear pores labeled with Nup98-GFP in a live COS-7 cell was observed with Sparse-SIM for more than ten mins. Images under the 2D-SIM and the Sparse-SIM ×2 configurations were shown in the upper and bottom

panels, respectively. (d) The snapshot of the nuclear pore structure enclosed by the cyan box in c was compared with a 100-nm fluorescent bead under different reconstruction methods (2D-SIM, 20 RL × 2, 50 RL × 2, Sparse ×2). (e) Because the sizes of nuclear pores were comparable to the resolution of Sparse-SIM and the size of the pixel, we followed the protocol in Supplementary Note 9.1 to derive the actual diameters of nuclear pore structures labeled by Nup35-GFP (red), Nup98-GFP (yellow), Nup93-GFP (green), and Nup107-GFP (cyan), respectively. (f) Average diameters of rings formed by Nup35 (66 ± 3 nm, n = 30 from 3 cells), Nup98 (75 ± 6 nm, n = 40 from 3 cells), Nup93 (79 ± 4 nm, n = 40 from 3 cells), or Nup107 (97 ± 5 nm, n = 40 from 3 cells). Left and right montages showed the results after Wiener reconstruction or Sparse deconvolution. (g) The magenta box in (c) is enlarged and shown at six time points. Scale bars: (c) 500 nm; (d, g) 100 nm.

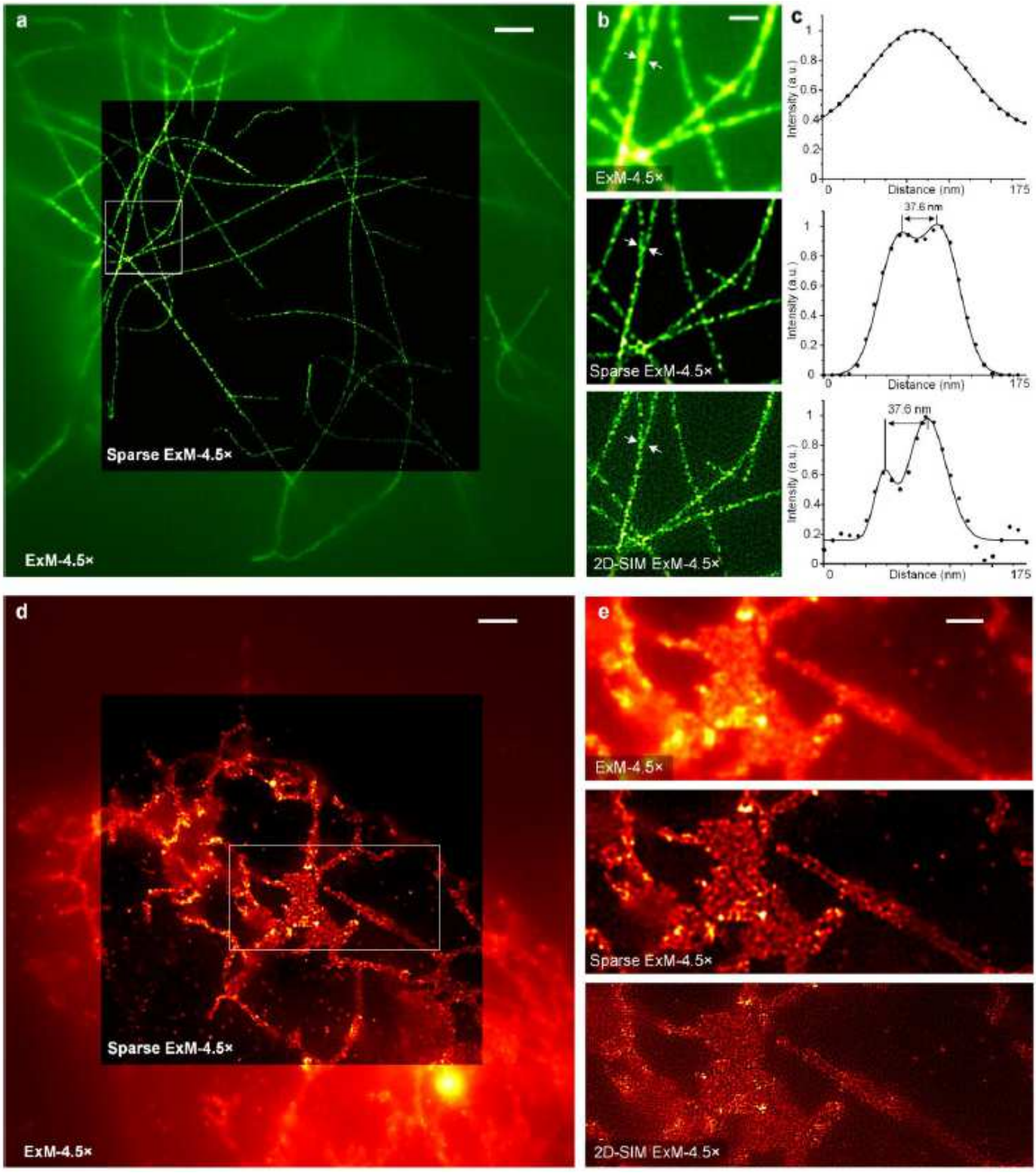

Figure 3

Sparse deconvolution assisted expansion microscopy (Sparse-ExM). (a) The COS-7 cell was immunostained with a primary antibody against α-tubulin, and a second antibody conjugated with AF488. We showed the 4.5 times expanded cell (ExM-4.5×) in the background and the Sparse ExM-4.5× image in the center. (b) Magnified views of the regions in (a) under ExM-4.5×, Sparse ExM-4.5×, and ExM-4.5× under the 2D-SIM (2D-SIM ExM-4.5×). (c) Intensity profiles and multiple Gaussian fitting of the

filaments are indicated by the white arrows in (c), respectively. The numbers represent the distances between peaks. (d) ExM images of Sec61β-GFP in a COS-7 cell. We showed the 4.5 times expanded cell (ExM-4.5×) in the background and the Sparse ExM-4.5× image in the center. (e) Enlarged regions enclosed by the white box in (a) seen under ExM-4.5×, Sparse ExM-4.5×, and 2D-SIM ExM-4.5×. (f) Highlighted regions from white boxes in (e). Scale bars: (a, d) 1 μm; (b) 300 nm; (e) 500 nm; (f) 200 nm.

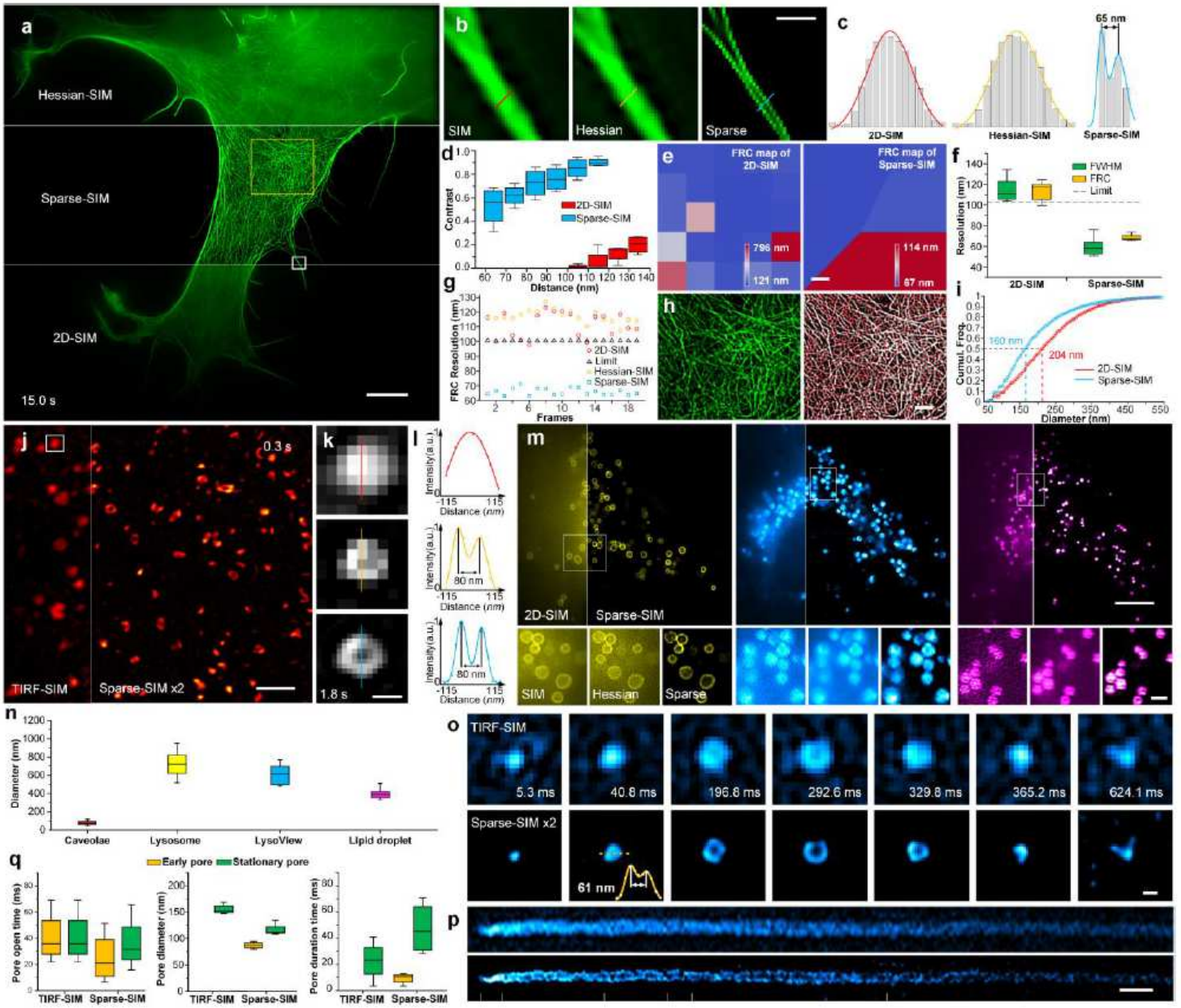

Figure 4

Sparse-SIM achieves ~60 nm and millisecond spatiotemporal resolution in live cells. (a) A representative COS-7 cell labeled with LifeAct-EGFP. (b-c) Enlarged regions enclosed by the white box in a (b), and the corresponding profiles along lines (c). Each box in (c) denotes the intensity of one pixel. (d) Average contrasts of two peaks with different distances. (e) FRC maps of actin filaments. (f) Resolutions measured as the FWHMs and by the FRC. (g) Time-dependent minimal FRC resolutions. Black triangles represent the theoretical resolution limit of 2D-SIM. (h) The magnified view of actin filaments in the

yellow box from (a) (left) and the segmented version (right, Method). (i) Cumulative distributions of pore sizes within the actin meshes in (h). (j) A representative COS-7 cell labeled with caveolin-EGFP. (k-l) From top to bottom are magnified views of the white box in (j) reconstructed by TIRF-SIM, Sparse-SIM, and Sparse-SIM ×2 with upsampling (k), and their fluorescence profiles are shown in (l). (m) Lysosomes were labeled with LAMP1-EGFP (left, yellow) or LysoView (middle, cyan), while lipid droplets were labeled with LipidSpot (right, magenta). (n) Average diameters of different vesicles. (o) Representative montages of a vesicle fusion event. (p) Kymographs from lines in TIRF-SIM (upper) and Sparse-SIM ×2 (lower) images are shown in (o). (q) Average opening time (left), diameters (middle), and duration time of early (yellow) and stationary (green) fusion pores (right). Centerline, medians; limits, 75% and 25%; whiskers, maximum and minimum; error bars, s.e.m.; Cumul. Freq., cumulative frequency; scale bars: (a, e, and m top) 5 μm; (b and j) 500 nm; (h and m bottom) 1 μm; (k, o) 100 nm; (p) 500 ms.

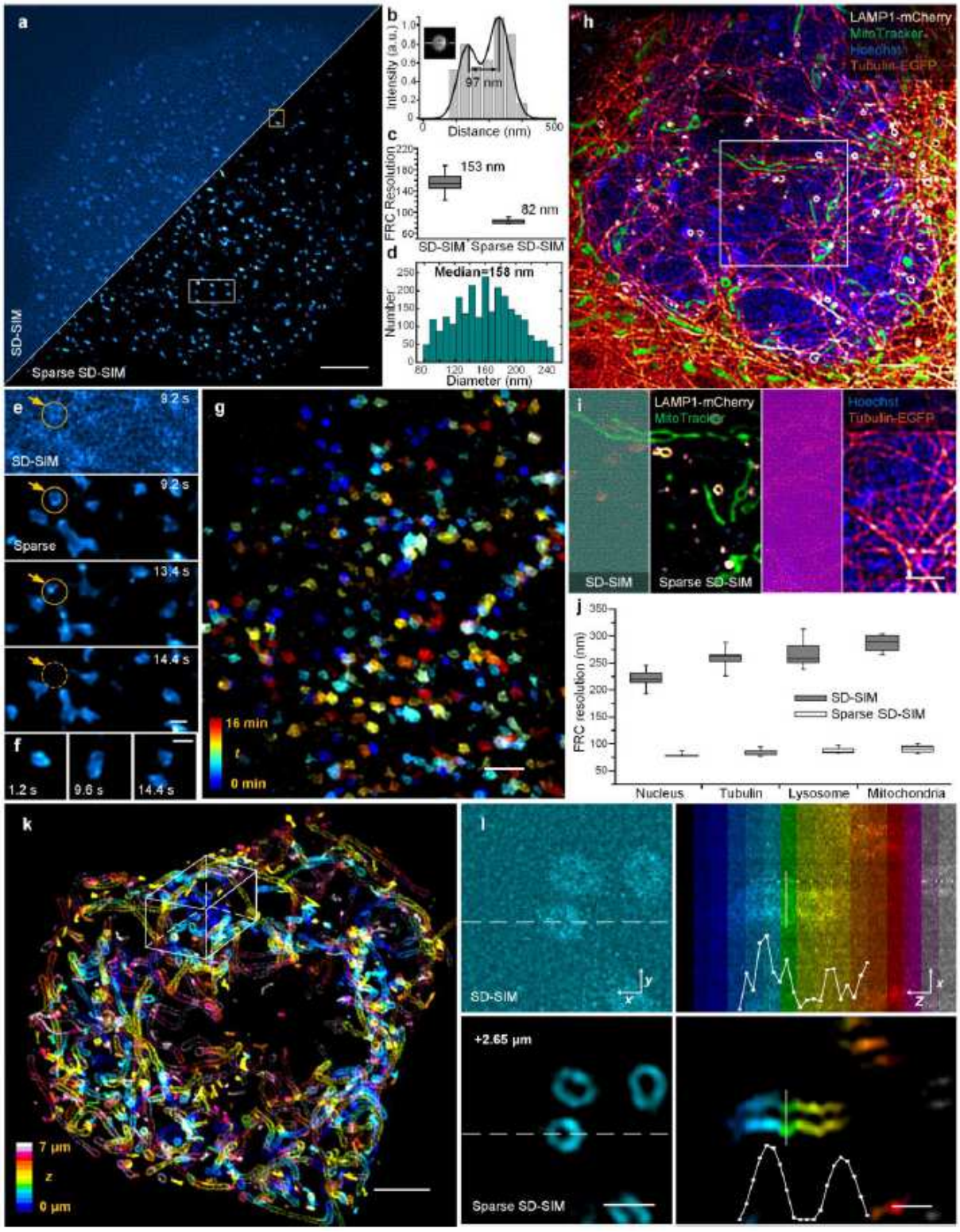

Figure 5

Sparse SD-SIM enables three-dimensional, multi-color, and sub-90-nm resolution for live-cell SR imaging. (a) A snapshot of CCPs in a COS-7 cell. (b) The profile corresponding to the resolved central ring of the CCP. (c) Average minimal resolutions by the FRC method. (d) Histogram of the diameters of CCPs. (e-f) Magnified view of the white boxed region (e) and yellow boxed region (f) in (a). (g) Temporal projections of CCPs within 16 mins. (h) A representative example of four-color (LAMP1-mCherry, yellow; MitoTracker,

green; Hoechst, blue; Tubulin-EGFP, brown), live-cell SR imaging. (i) Magnified view of the white boxed region in (h). (j) Average resolutions by the FRC method. (k) Three-dimensional distributions of all mitochondria (labeled with TOM20-mCherry) of a live COS-7 cell. (l) Color-coded horizontal (left) and vertical sections (right) from the white boxed region in (k). Centerline, medians; limits, 75% and 25%; whiskers, maximum and minimum; error bars, s.e.m; scale bars: (a, i) 3 μm; (e, f) 300 nm; (g, l) 1 μm; (h, k) 5 μm.

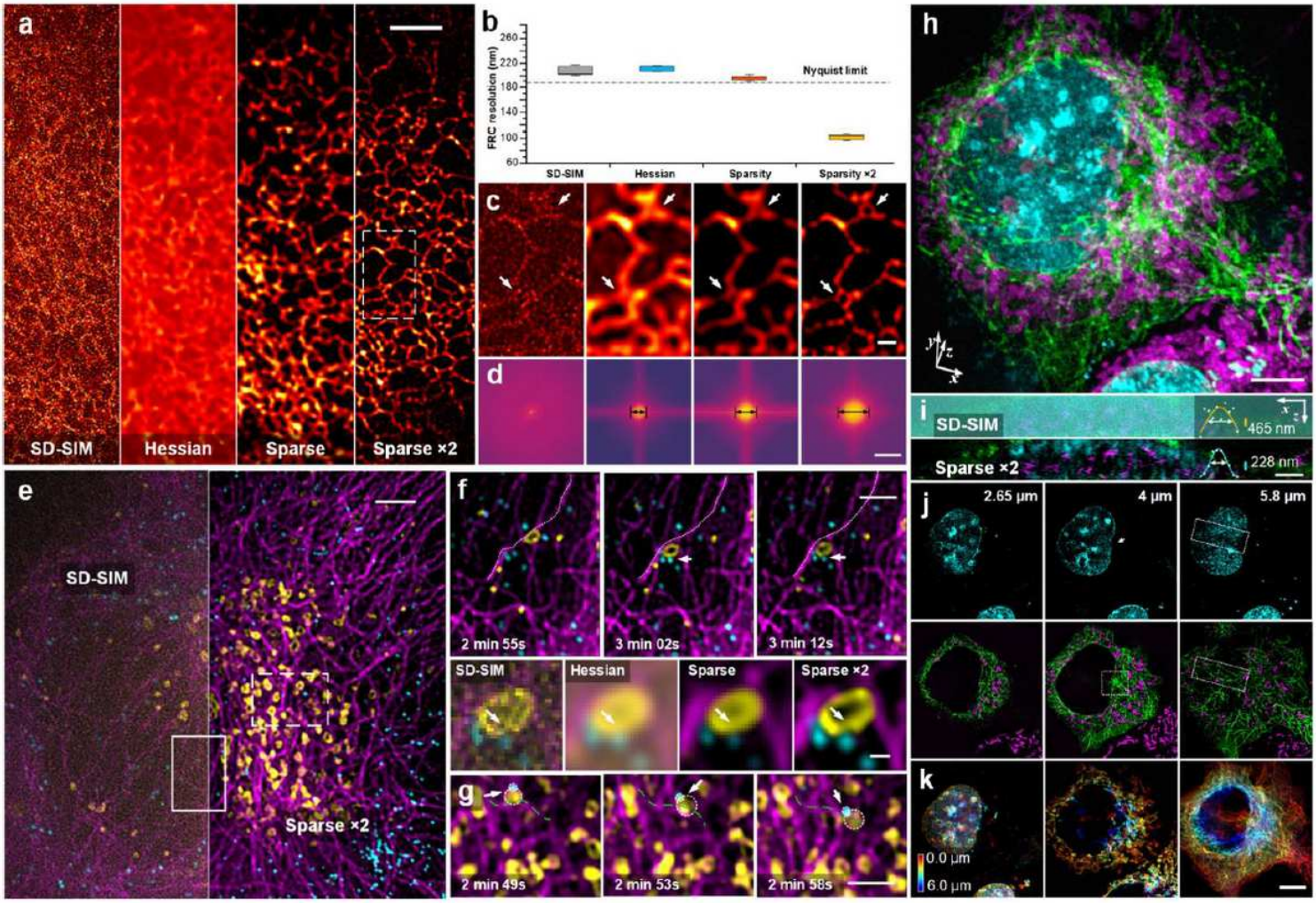

Figure 6

Upsampling enables Sparse SD-SIM to overcome the Nyquist sampling limit to achieve multi-color 3D SR imaging in live cells. (a) ER tubules in a COS-7 cell seen under different configurations. (b) Average resolutions by the FRC method. (c) Magnified views of ER tubules from (a). (d) Fourier transforms of images. Black arrows indicate the OTFs of corresponding images. (e) A snapshot of a HeLa cell labeled with tubulin-EGFP (magenta), Pex11a-BFP (cyan), and Lamp1-mCherry (yellow). (f) Magnified views in (e). As highlighted by white arrows in the bottom panel, only Sparse SD-SIM ×2 can dissect the lysosome's deformation by a neighboring peroxisome. (g) Time-lapse images of another example of the co-movement of both a lysosome and a peroxisome along a microtubule. (h) Live-cell three-color (Tubulin-EGFP, green; Hoechst, cyan; MitoTracker Deep Red, magenta) 3D imaging by Sparse SD-SIM ×2. (i) The z-axial view from (h). (j) Three horizontal sections of the cellular nucleus (top) and mitochondria

merged with microtubules (bottom). (k) Color-coded volumes of nuclei, mitochondria, and microtubules. Scale bars: (a, d, e, h, i, j, and k) 5 μm; (b and f top, and g) 3 μm; (c) 1 μm; (f middle and bottom) 500 nm.

Supplementary Files

This is a list of supplementary files associated with this preprint. Click to download.

- SupplementaryinformationSparseSIM.pdf
- 1MovieNup98Longterm.mp4
- 2MovieActin.mp4
- 3VideoCaveoleTIRF.mp4
- 4Movielamplysolipid.mp4
- 5MovieFusionPoreinrealtime.mp4
- 6MovieFusionPore.mp4
- 7MovieMito.mp4
- 8MovieMitoER.mp4
- 9MovieCCP.mp4
- 10Movie4colorlysomitonucltub.mp4
- 11MovieTOM203DMito.mp4
- 12MovieER.mp4
- 13Moviemicrotubulelysosomeperoxisome.mp4
- 14Movie3color3D.mp4
- 15MovieActinWFSIM.mp4
- 16MovieActinCCP.mp4
- 17MovielysoER.mp4
- 18MovieMTPM.mp4